

Contact mechanics of filled thermoplastic and thermoset polymer systems

Citation for published version (APA):

Krop, S. (2016). *Contact mechanics of filled thermoplastic and thermoset polymer systems*. [Phd Thesis 1 (Research TU/e / Graduation TU/e), Mechanical Engineering]. Technische Universiteit Eindhoven.

Document status and date:

Published: 26/04/2016

Document Version:

Publisher's PDF, also known as Version of Record (includes final page, issue and volume numbers)

Please check the document version of this publication:

- A submitted manuscript is the version of the article upon submission and before peer-review. There can be important differences between the submitted version and the official published version of record. People interested in the research are advised to contact the author for the final version of the publication, or visit the DOI to the publisher's website.
- The final author version and the galley proof are versions of the publication after peer review.
- The final published version features the final layout of the paper including the volume, issue and page numbers.

[Link to publication](#)

General rights

Copyright and moral rights for the publications made accessible in the public portal are retained by the authors and/or other copyright owners and it is a condition of accessing publications that users recognise and abide by the legal requirements associated with these rights.

- Users may download and print one copy of any publication from the public portal for the purpose of private study or research.
- You may not further distribute the material or use it for any profit-making activity or commercial gain
- You may freely distribute the URL identifying the publication in the public portal.

If the publication is distributed under the terms of Article 25fa of the Dutch Copyright Act, indicated by the "Taverne" license above, please follow below link for the End User Agreement:

www.tue.nl/taverne

Take down policy

If you believe that this document breaches copyright please contact us at:

openaccess@tue.nl

providing details and we will investigate your claim.

Contact mechanics of filled thermoplastic and thermoset polymer systems

Sam Krop

Contact mechanics of filled thermoplastic and thermoset polymer systems by Sam Krop
Technische Universiteit Eindhoven, 2016.

A catalogue record is available from the Eindhoven University of Technology Library
ISBN: 978-90-386-4058-7

This thesis was prepared with the L^AT_EX₂ ϵ documentation system.
Reproduction: Ipskamp Printing BV, Enschede
Cover design: Frans Goris (Grafische Werken)

The work presented in this thesis is financially supported by AkzoNobel N.V.

Contact mechanics of filled thermoplastic and thermoset polymer systems

PROEFSCHRIFT

ter verkrijging van de graad van doctor aan de Technische Universiteit Eindhoven, op
gezag van de rector magnificus prof.dr.ir. F.P.T. Baaijens, voor een commissie
aangewezen door het College voor Promoties, in het openbaar te verdedigen op
dinsdag 26 april 2016 om 16:00 uur

door

Sammie Krop

geboren te Paramaribo, Suriname

Dit proefschrift is goedgekeurd door de promotoren en de samenstelling van de promotiecommissie is als volgt:

voorzitter: prof.dr. L.P.H. de Goey
promotor: prof-em.dr.ir. H.E.H. Meijer
copromotor: dr.ir. L.C.A. van Breemen
leden: prof.dr.ir. T.A. Tervoort (ETH Zürich)
prof.dr. C. Gauthier (Université de Strasbourg)
prof.dr. C. Creton (ESPCI ParisTech)
prof.dr. R.A.T.M. van Benthem
dr.ir. J.J.C. Remmers

Het onderzoek of ontwerp dat in dit proefschrift wordt beschreven is uitgevoerd in overeenstemming met de TU/e Gedragscode Wetenschapsbeoefening.

Contents

Summary	ix
1 Introduction	1
2 Global and local large-deformation response of sub-micron, soft- and hard-particle filled polycarbonate	5
2.1 Introduction	7
2.2 Experimental	9
2.2.1 Materials and sample preparation	9
2.2.2 Testing	10
2.3 Modeling	10
2.3.1 Microstructure	10
2.3.2 Constitutive model	12
2.4 Results and Discussion	14
2.4.1 Experimental results	14
2.4.2 Numerical results	16
2.5 Conclusions	24
3 Multi-mode modeling of global and local deformation, and failure, in particle filled epoxy systems	27
3.1 Introduction	29
3.2 Experimental	30
3.2.1 Materials and sample preparation	30
3.2.2 Testing	31
3.3 Modeling	32
3.3.1 Constitutive modeling	32
3.3.2 Microstructure	33
3.4 Results and Discussion	34

3.4.1	Glass transition temperature	34
3.4.2	Characterization of the epoxy matrix	34
3.4.3	Particle filled epoxy	38
3.5	Conclusions	45
3.A	Material parameters	46
4	Finite element modeling and experimental validation of single-asperity sliding friction on particle filled polycarbonate	47
4.1	Introduction	49
4.2	Experimental	50
4.2.1	Materials and sample preparation	50
4.2.2	Testing	51
4.2.3	Experimental results	51
4.3	Modeling	53
4.3.1	Constitutive model	53
4.3.2	Homogenization procedure	54
4.3.3	FE mesh and friction modeling	56
4.3.4	Influence of tip geometry	58
4.3.5	Effect of local friction coefficient	60
4.3.6	Comparing experiments with simulations	61
4.3.7	Stress field	62
4.4	Conclusions	64
4.A	Material parameters	65
5	Sliding friction on particle filled epoxy: Developing a quantitative model for complex coatings	67
5.1	Introduction	69
5.2	Experimental	70
5.2.1	Materials and sample preparation	70
5.2.2	Testing	71
5.2.3	Experimental results	71
5.3	Modeling	74
5.3.1	Intrinsic mechanical response	74
5.3.2	Scratch simulations	77
5.3.3	Comparing experiments with simulations	79
5.3.4	Effect of SR filler-particles	81
5.4	Conclusions	89
5.A	Material parameters	91

6	Micro-structural design for optimum scratch-resistant, wear-resistant, and low-friction coatings	93
6.1	Introduction	93
6.2	Scratch-resistant and low-friction coatings	94
6.2.1	Yield or post-yield	95
6.2.2	Scratch resistance and yield stress	96
6.2.3	Low friction coatings	99
6.3	Wear-resistance	100
6.3.1	Introduction	100
6.3.2	Wear in unfilled epoxy systems	100
6.3.3	Wear in filled epoxy systems	104
6.4	Optimizing for scratch- and wear resistant coatings	110
6.5	Conclusions and recommendations	115
7	Conclusions and Recommendations	119
7.1	Conclusions	119
7.2	Recommendations	123
	References	125
	Samenvatting	133
	Dankwoord	135
	Curriculum Vitae	137
	List of Publications	139

Summary

This study aims to relate the intrinsic mechanical response of particle-filled polymer glasses to their response in sliding friction. A previous study showed that the frictional properties of unfilled polycarbonate are quantitatively captured by finite element simulations when using a proper constitutive model, i.e. a model that captures the polymers intrinsic mechanical response quantitatively, and a rate-independent friction (stick-slip) model. Single-asperity scratch tests were successfully modeled over a range of scratch velocities and for different indenter-tip geometries.

In this thesis we extend these pioneering results to the class of practically more relevant and interesting particle-filled (thermoplastic and thermoset) polymer systems. To that end, hard- and soft-particle filled polycarbonate and epoxy systems are investigated. Starting with polycarbonate (that is over the years fully characterized) as matrix material, hard inorganic (TiO_2) and soft rubber (MBS) filled model systems are designed and produced. Their intrinsic response is measured in lubricated uniaxial compression tests. To reveal local events at the interparticle level, three-dimensional representative volume elements (3D-RVEs) are constructed to model the complex microstructure of these systems. Finite element simulations of these 3D-RVEs show that the intrinsic response is captured well but, moreover, they provide insight in the critical local events that lead to global failure. The simulations provide the (homogenized) material parameters that macroscopically describe these particle-filled systems, and that are used in the simulations of their scratch response in sliding friction tests. It is confirmed that by combining a proper constitutive framework with the most simple, rate-independent, friction model, all experiments are appropriately described quantitatively by the numerical simulations. Furthermore, the onset of failure during scratching becomes accessible. The local (homogenized) strains resulting from the scratch simulations can be translated to simulations on the RVE-level that reveal the extent of critical events at the interparticle level.

After the successful modeling of filled thermoplastic systems, the focus is next on thermosets. Epoxy-based composites are investigated, designed and produced, since this matrix is more relevant for coating applications. The intrinsic mechanical response of the matrix material, a standard epoxy, is characterized and the material parameters used in the constitutive model are determined. The model systems filled with either soft polysiloxane rubber particles or hard TiO_2 particles are created and tested. It is shown that the complete methodology as derived and described for polycarbonate is also valid for these thermoset systems.

The thesis ends with an onset of designing smart materials, inspired by our findings from the simulations on the microstructures and the scratch tests.

CHAPTER 1

Introduction

Tribology, the science of adhesion, friction, lubrication, and wear of surfaces in relative motion, remains as important today as it was in ancient times. It plays a role in the fields of physics, chemistry, geology, biology, and engineering [1]. The complexity of even the simplest tribological process originates from mechanisms acting at different length- and time-scales. Friction is closely related to both adhesion and wear. To determine what happens at the macroscopic level, understanding of highly non-equilibrium processes occurring at the molecular level is required. Both surfaces can be hard or soft, elastic, plastic or viscoelastic, smooth or rough, and of very different chemistries. Many asperities on both surfaces are constantly coming into (and out) of contact within milliseconds, causing fluctuations in local pressures in the Pa–GPa range. The introduction of the atomic force microscope (AFM) has enabled quantitative (nanometer scale) single-asperity friction experiments, opening opportunities to investigate these tribological processes at the molecular level [2]. Parallel to the development of sophisticated measurement tools, theoretical approaches such as molecular dynamics (MD) simulations emerged. Atomistic MD simulations have provided valuable understanding of processes at the smallest time- and length-scale, but there also lies its main weakness: simulations are currently limited to timescales of tens of nanoseconds and lengthscales of nanometers. For polymers this poses even more problems due to their molecular architecture and long relaxation times. Applying these techniques as an engineering tool for real-life applications, such as for designing and testing scratch and wear resistant coatings, is therefore impractical.

Historically, simple empirical laws have been used to describe tribological processes at the macroscopic level. This dates back to Leonardo Da Vinci (1452–1519) who stated

two laws of friction: (1) the areas in contact have no effect on friction and (2) the force to overcome friction is doubled if the load of an object is doubled. These two laws were rediscovered three centuries later by Guillaume Amontons, and subsequently refined by Charles-Augustin de Coulomb, leading to what we now know as the Amontons-Coulomb law of (dry) friction:

$$\mu_a = \frac{F_f}{F_n}, \quad (1.1)$$

with the apparent friction coefficient μ_a that gives the proportionality between the friction force F_f and F_n , the normal load applied. Statement (1) is counterintuitive at first sight since most of us would assume that friction does depend on the cross-sectional area. In fact, this statement was first contradicted by the work of Bowden et al. [3] on metal-metal interfaces, but later explained by the concept of the true area of contact as proposed by Archard [4]. This view introduced the notion of multi-asperity contact, where the real area results from a summation of all small, up to atomic-scale, contact sites. Greenwood and Wu [5] showed that the result of this summation is close to that of a smooth asperity with the same general shape.

This definition helps when a (micrometer scale) single-asperity scratch set-up is considered: the topological properties of the rigid diamond indenter surface and the deformable polymer surface follow from their surface profiles. Therefore, the indenter is considered a rigid smooth cone with a specified top radius (of micrometer scale) and the polymer as a flat surface. The single-asperity sliding friction test, often referred to as ‘scratch test’, allows studying a wide range of surface mechanical properties in a controlled manner, including the characterization of coatings and modeling of deformation and wear when subjected to hard asperity contact [6–10]. In these cases deformations are typically surpassing the elastic regime, resulting in ductile ploughing and ultimately in wear [11]. Generally, the frictional response is decomposed into two components: adhesion, which in fact originates from the nanometer-scale processes discussed before, and (large scale) deformation. This implies that the real contact area, in this case between indenter and polymer surface, is important for a proper description of the (macroscopic) scratch response. For ideal elastic or ideal plastic deformation this area is easily determined, but for polymers, characterized by their visco-elastic nature, this is not as straightforward. However, with the rise of Finite Element Methods (FEM) new possibilities opened to study nonlinear contact problems. In a previous study, Van Breemen et al. [12], this route was explored using a hybrid experimental–numerical approach to analyze the scratch response of polycarbonate, a well characterized (thermoplastic) model polymer. The simple (rate-independent) Amontons-Coulomb law of friction in combination with a constitutive model that quantitatively captures the poly-

mers' intrinsic mechanical response, proved to be capable of capturing the scratch response for different sliding velocities applied, and for different indenter-tips, with a single set of material parameters and one unique friction coefficient. The approach revealed the subtle interplay between the adhesive contribution, that dictates the formation and size of the bow wave in front of the indenter, and the rate dependent mechanical behavior of the polymer substrate.

In practice, and especially in tribological applications, most polymers are filled, since mixing combinations of existing polymers and reinforcements is usually a more cost-efficient route than developing new polymers [13, 14]. Other reasons are to change the appearance through colorants, e.g. in (decorative) coatings, or as a cost reduction in the form of cheap fillers that replace a more expensive matrix material. Therefore, the work on unfilled PC is extended to particle-filled systems. The effect of filler particles, either soft or hard, on the intrinsic stress-strain response is first explored by preparing well-defined model systems. In parallel, three-dimensional Representative Volume Elements (3D-RVEs) are created as simplified representations of the filled-polymers' microstructure. These 3D-RVEs have a twofold purpose, they provide insight into the local (inter-particle) deformations leading to microscopic, and ultimately, macroscopic wear, and they provide material parameters necessary for the scratch simulations. An important class of materials in contact mechanics are coatings. Therefore, thermosetting polymers such as epoxies, polyesters and polyurethanes have much more relevance here. Epoxy-based composites are prepared and investigated, following the same strategy as used for the PC-based model systems. First the pure epoxy is investigated, next filled systems are prepared and the parameters used in the homogenized constitutive equations are determined via compression tests and simulations on 3D-RVEs; finally scratch tests are performed at different speeds, and compared to numerical predictions. The thesis ends with an onset of designing smart materials, inspired by our findings from the simulations on the microstructures and the scratch tests.

CHAPTER 2

Global and local large-deformation response of sub-micron, soft- and hard-particle filled polycarbonate

Abstract

Since polymers play an increasingly important role in both structural and tribological applications, understanding their intrinsic mechanical response is key. Therefore in the last decades much effort has been devoted into the development of constitutive models that capture the polymers' intrinsic mechanical response quantitatively. An example is the Eindhoven Glassy Polymer model. In practice most polymers are filled, e.g. with hard particles or fibers, with colorants, or with soft particles that serve as impact modifiers. To characterize the influence of type and amount of filler particles on the intrinsic mechanical response, we designed model systems of polycarbonate with different volume fractions of small, order 100 nm sized, either hard or soft particles, and tested them in lubricated uniaxial compression experiments. To reveal the local effects on interparticle level, three-dimensional representative volume elements (RVEs) were constructed. The matrix material is modeled with the EGP model and the fillers with their individual mechanical properties. It is first shown that (only) 32 particles are sufficient to capture the statistical variations in these systems. Comparing the simulated response of the RVEs with the experiments demonstrates that in the small strain regime

Reproduced from: S. Krop, H.E.H. Meijer, and L.C.A. van Breemen. "Global and local large-deformation response of sub-micron, soft- and hard-particle filled polycarbonate," *Journal of the Mechanics and Physics of Solids* **87**, 51–64 (2016).

the stress is under-predicted since the polymer matrix is modeled by using only one single relaxation time. The yield- and the large strain response is captured well for the soft-particle filled systems while, for the hard-particles at increased filler loadings, the predictions are less accurate. This is likely caused by polymer-filler interactions that result in accelerated physical aging of the polymer matrix close to the surfaces. Modifying the S_a -parameter, that captures the thermodynamic state of the polymer matrix, allows to correctly predict the macroscopic response after yield. The simulations reveal that all rate-dependencies of the different filled systems originate from that of the polymer matrix. Finally, an onset is presented to predict local and global failure based on critical events on the microlevel, that are likely to cause the over-prediction in the large-strain response of the hard-particle filled systems.

2.1 Introduction

Predicting the intrinsic mechanical response of polymers is one of the major challenges of material scientists. Constitutive models that quantitatively capture this intrinsic response are an essential part of the engineering tools and used in finite element methods (FEM) to help designing their structural applications. In practice most engineering polymer materials are composites since mixing combinations of existing polymers and reinforcements is usually a more cost-efficient route than developing new polymers based on new chemistry [13, 14]. In composites the macroscopic response originates from the individual intrinsic responses of the constituents, their volume fractions, the spatial distribution, and the interfacial interactions [15]. Historically, in the absence of numerical techniques, this issue was addressed using approximations based on mean-field homogenization schemes [16–22]. With the introduction of computers more complex methods could be implemented, but originally still for simplified situations, such as restrictions to two-phase systems, simple elasto-plastic materials, moderate macroscopic strains, low filler fractions, and periodic distributions. Usually analyses were restricted to two-dimensional problems only, due to large computational costs [23–27].

One of the first attempts to overcome these restrictions was by the group of Llorca [28–31], who used unit cells containing several dozens of particles. They showed with FEM simulations that the mechanical response over different particle realizations presented little scatter provided that indeed a sufficient number of particles was present. Still, these systems consisted of simple elastic and elasto-plastic systems. With Pierard et al. [32] a first attempt was made to model an elasto-viscoplastic (Perzyna model) system. The moduli of the two constituents differed less than an order of magnitude, and only the small strain regime was considered. Numerical results were only compared to other homogenization techniques only, not to actual experimental results. Of particular interest in recent years is the class of so-called nanocomposites where high surface-to-volume ratio's make interfacial effects become more important. Often a third phase surrounding the nano-particles is introduced, the interphase, using one- or two-step modeling strategies. With the former strategy interphases are directly incorporated in the representative volume element (RVE), with the latter an 'effective particle' is introduced, homogenizing particle and interphase [33–36]. Also in these examples only the small-strain elastic regime was considered.

In this chapter we will try to improve on these points by capturing the actual mechanical response starting with the intrinsic mechanical behavior of the polymer matrix. Upon

homogeneous deformation, glassy polymers initially show a viscoelastic region which becomes progressively nonlinear with increased loading. At the yield point (the first maximum in the curve) the stress is sufficiently high to overcome intermolecular forces at the rate of deformation prescribed, allowing large-scale segmental motion of the polymer chains. The post-yield response displays two characteristic phenomena: (i) strain softening, the initial decrease of true stress with increasing true strain, which is related to a structural evolution that reduces the material's resistance to plastic deformation, and (ii) strain hardening, the increase in stress at high strains, which originates from the network of entangled polymer chains that orients with deformation. The macroscopic response of polymers is strongly determined by the interplay between these two effects: strain softening tends to destabilize the deformation leading to the formation of localized plastic deformation zones, while the evolution of these plastic zones strongly depends on the stabilizing effect of strain hardening. These concepts are employed in several 3-D constitutive models, such as the Boyce-Parks-Argon (BPA) model [37, 38], the Oxford Glass-Rubber (OGR) model [39–41] and the Eindhoven Glassy Polymer (EGP) model [42–46].

The highly non-linear time-dependent behavior of polymers causes in filled polymer systems the macroscopic response to be dominated by a sequential yielding process throughout the total microstructure. Mean-field homogenization schemes are therefore useless beyond the small-strain regime. For the response at increased deformation, analyses are needed that incorporate the microstructure of the system in an RVE. The advantage of such an approach is that events at the interparticle scale are probed as well, as nicely demonstrated by Van Melick et al. [25] and Meijer and Govaert [13] for two-dimensional RVEs of polystyrene and polycarbonate matrices filled with circular voids, where the matrix was modeled using the EGP-model. They showed qualitatively the effect of voids on the macroscopic response, and demonstrated that a hydrostatic-stress based craze-nucleation criterion could be used to predict brittle-to-ductile transitions.

Here again polycarbonate (PC) is used as model material for the matrix and hard- and soft-particle filled systems are prepared and tested in uniaxial compression. These model systems are captured by 3D RVEs in a finite element mesh. First the critical size of the unit cell or RVE is determined, i.e. the minimum number of particles in the system that is required to ensure its representative character. Subsequently, the optimal element size inside the RVE is investigated. Next compression tests are performed, and experimental results are compared with the macroscopic response as it follows from the numerical simulations. Finally the local response on interparticle level is investigated and discussed, using a critical hydrostatic-stress based criterion to predict local and fi-

nally global failure. This criterion proved successful in predicting craze nucleation in a vast range of glassy polymers such as polycarbonate, polystyrene, poly(2,6-dimethyl-1,4-phenylene oxide), polysulphone, and (unplasticized) polyvinyl chloride [25, 47–52]. The part of the work presented in this chapter prepares for the modeling of soft- and hard-particle filled thermoset epoxies that finally will be modeled and tested as coatings in sliding friction experiments, analogous to Van Breemen et al. [12].

2.2 Experimental

2.2.1 Materials and sample preparation

The matrix material used is polycarbonate (PC). For the soft-particle filled systems we used Lexan 141R (Sabic Innovative Plastics, Bergen op Zoom, the Netherlands), an injection molding grade of PC. The filler particles are a low temperature impact modifier, Paraloid EXL-2600 (Rohm & Haas), a methacrylate-butadiene-styrene (MBS) core-shell copolymer with a diameter of 100 nm. Samples with two filler fractions were prepared by Sabic IP: 4.5 and 9 vol% MBS. Cylindrical compression samples (\varnothing 3 mm \times 3 mm) are machined from injection molded bars (80 \times 10 \times 4 mm³). The matrix material used for the hard-particle filled systems is Lexan 101R, an extrusion grade of PC. The hard particles are Ti-Pure R-706 (DuPont Titanium Technologies), a dry grade titanium dioxide (TiO₂) with a particle size of 350 nm. To improve the quality of mixing, PC pellets are grinded and subsequently premixed with TiO₂ in a ratio of 60/40 vol% PC/TiO₂. The premixed batch is vacuum dried at 80 °C for 12 hours before further compounding on a small Prism TSE 16 mm co-rotating twin screw extruder with temperature set to 220 °C and using a rotational speed of 100 rpm. To minimize absorption of water by the hydrophilic TiO₂ the premixed PC/TiO₂ is continuously flushed with nitrogen during feeding into the extruder. Following the same procedure, this master-batch is subsequently diluted to batches containing 5, 10, and 20 vol% TiO₂. Cylindrical samples (\varnothing 4 mm \times 4 mm) for the uniaxial compression tests are machined from compression molded plates (40 \times 35 \times 6 mm³). The dried PC/TiO₂ pellets are heated in a mold for 30 minutes at 60 °C above its glass transition temperature (T_g) and then compressed in seven subsequent intervals of 1 minute, progressively increasing the force with each step to a final force of 100 kN. Between each compression step, the force is released to allow for degassing. Finally the mold is placed in a cold press and cooled to room temperature under a force of 30 kN. For comparison, also compression samples of unfilled PC are prepared following the same procedure.

2.2.2 Testing

To determine the T_g , differential scanning calorimetry (DSC) experiments are performed with a Mettler Toledo DSC823e. First, samples of approximately 15 mg are heated to 250 °C, the subsequent scan is performed at a cooling rate of 10 K/min to 25 °C. The distribution of TiO₂ particles in the PC matrix is checked with a FEI Quanta 600F ESEM in low vacuum mode using backscattered electron (BSE) imaging. Uniaxial compression tests are performed on a Zwick 1475 tester. Cylindrical samples are compressed between two parallel flat steel plates at constant true strain rates of 10^{-5} – 10^{-2} s⁻¹. To prevent bulging due to friction between plates and samples, a thin PTFE film (3M 5480 skived plastic film tape) is applied on both ends of the sample and a lubricant (Grifon PTFE spray TF 089) is used on both contact areas between plates and samples. All compression experiments are performed at an ambient temperature of 23 °C.

2.3 Modeling

2.3.1 Microstructure

The heterogeneous microstructure is modeled with a representative volume element (RVE), a periodic cubic unit cell containing a finite number of particles in a finite element mesh. The particles, representing the fillers in the matrix, are assumed to be spherically shaped, mono-sized, and to adhere perfectly to the matrix material. The particle size distribution and the exact shape of the filler particles certainly affects the stress field and overall response, as shown by Chawla and Chawla [53] for a particle reinforced metal-matrix composites. But this method requires extensive characterization of the morphology of the particle-filled samples, followed by cumbersome meshing of these microstructures. These difficulties are circumvented by simplifying the particle shape, i.e modeling the particles as ellipsoids or spheres. Since in RVE computations, that are characterized by sequential yielding events throughout the volume, the difference in response between systems using spherical and elliptical inclusions proved to be only marginal [53], we here assume mono-sized spherically shaped particles, since ellipsoids introduce, apart from the spatial distribution, an extra directional distribution that unnecessary complicates the analysis. We do not know the exact contact condition between filler particles and the polymer matrix, which leaves us with two options: either perfect contact, or no adhesion at all. Due to the excellent adhesive properties of PC, we assume that it adheres perfectly to the filler particles.

The spatial distribution of the spheres is generated in a MATLAB (The Mathworks Inc.) program. Using a build-in routine, uniformly distributed pseudo-random numbers are generated to produce the coordinates for the spheres in the simulation box. To avoid the same sequence of numbers for each run, the random number generator is seeded based on the current system time [54]. With the number of spheres fixed, the radius of the spheres (R) is computed from the desired volume fraction. Spheres within a defined minimum allowed distance (h_{min}) from any other sphere are rejected (if $x \leq 2R + h_{min}$). Spheres very close to or only slightly crossing the cubic cell faces are also rejected, since they would complicate meshing of the small gap or small part of the sphere. After each rejection another coordinate is generated and checked until the desired number of spheres is placed in the simulation box. Note that since the RVE is periodic, the allowable distance check between spheres also needs to be performed at the periodic boundaries.

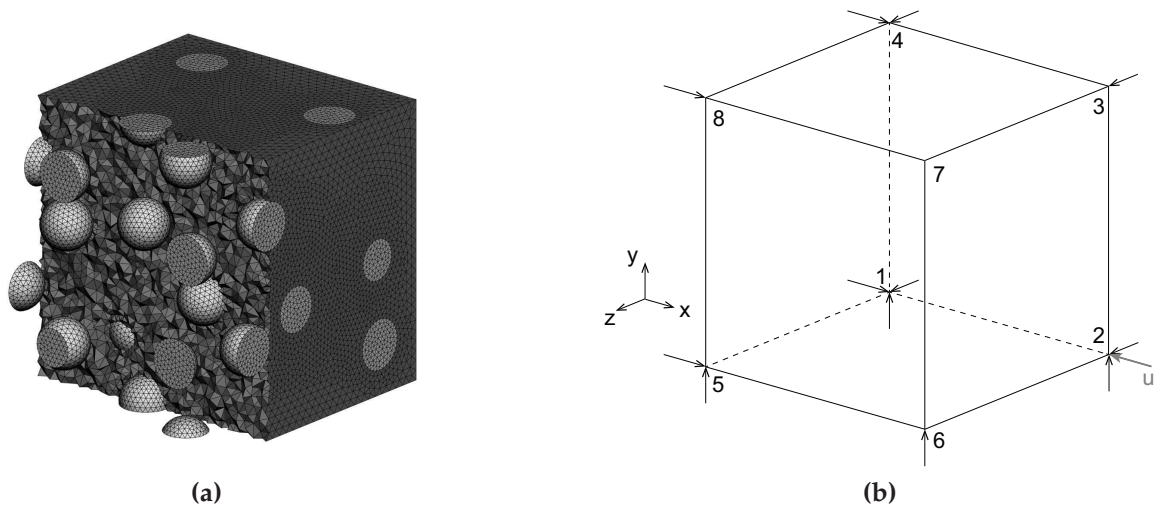


Figure 2.1: Example of a meshed RVE with part of the matrix made invisible (a), and the boundary conditions applied for uniaxial compression in the x -direction (b).

With the spatial distribution generated, the geometry is constructed and subsequently meshed with Gambit 2.4.6 [55]. Particles intersecting a cube face are split and copied to the opposite cube face. The faces are subsequently meshed with linear triangular elements, see Figure 2.1a. The finite element mesh also needs to be periodic so only three face meshes are unique, each face mesh is copied to the opposite cube face. The volume is meshed using 4-node tetrahedral elements. Rigid body movement is prevented by applying the boundary conditions on the corner nodes, see Figure 2.1b. Periodic boundary conditions are used on the faces of the RVE, to ensure that the shape of two opposing faces remains the same. This is achieved by tying nodes on the right face

(A_{2673}) with their associated nodes on the left face (A_{1584}) and to nodes 1 and 2. With the other faces tied in a similar way, these nodal ties are expressed as

$$\begin{aligned}\vec{x}_{A_{2673}} &= \vec{x}_{A_{1584}} - \vec{x}_1 + \vec{x}_2, \\ \vec{x}_{A_{8734}} &= \vec{x}_{A_{5621}} - \vec{x}_1 + \vec{x}_4, \\ \vec{x}_{A_{5678}} &= \vec{x}_{A_{1234}} - \vec{x}_1 + \vec{x}_5,\end{aligned}\tag{2.1}$$

where \vec{x}_i represents the actual position vector of node i and $\vec{x}_{A_{ijkl}}$ indicates the position vector of nodes on the surface A_{ijkl} . For the situation in Figure 2.1b, the true strain along the x-axis resulting from the prescribed displacement u is given by $\ln(1 + u/1)$, and the corresponding stress is obtained by dividing the reaction force in node 2 in the x-direction by the surface area of A_{2673} . Note that since all the nodes on this face are linked to node 2, see Equation (2.1), the reaction force in this node is the total load on this face.

2.3.2 Constitutive model

We use the EGP-model [43, 44] for the matrix material. It is based on an additive decomposition of the Cauchy stress into a hardening stress and a driving stress. The hardening stress accounts for the stress contribution of the entangled network and is modeled with a neo-Hookean spring (G_r); the driving stress is attributed to intermolecular interactions and is additively decomposed into a hydrostatic (volumetric) part, expressed by Poisson ratio ν , and a deviatoric part. In this framework, the deviatoric part of the driving stress (σ_s^d) is modeled as a combination of multiple parallel linked Maxwell elements but, for computational reasons, only the first mode will be used here. The plastic deformation rate tensor (D_p) relates to the driving stress σ_s^d by a non-Newtonian flow rule, that for the isothermal case reads

$$D_p = \frac{\sigma_s^d}{2\eta(\bar{\tau}, p, S_a)}.\tag{2.2}$$

Here, the viscosity η depends on the equivalent stress $\bar{\tau}$, the pressure p and the thermodynamic state of the material S_a . The viscosity is described by an Eyring flow rule, which has been extended to take pressure dependence and intrinsic strain softening into account:

$$\eta = \eta_{0,ref} \underbrace{\frac{\bar{\tau}/\tau_0}{\sinh(\bar{\tau}/\tau_0)}}_{(I)} \underbrace{\exp\left(\frac{\mu p}{\tau_0}\right)}_{(II)} \underbrace{\exp(S_a R(\bar{\gamma}_p))}_{(III)},\tag{2.3}$$

where the initial viscosity $\eta_{0,ref}$ defines the so-called reference (un-aged) state, part I represents the stress dependence with the characteristic stress τ_0 , the pressure dependence (part II) is governed by the parameter μ , and part III captures the dependency of the viscosity on the thermodynamic history via S_a . The equivalent plastic strain $\bar{\gamma}_p$ follows from its evolution equation:

$$\dot{\bar{\gamma}}_p = \sqrt{2\mathbf{D}_p : \mathbf{D}_p}. \quad (2.4)$$

Strain softening is described by the softening function $R(\bar{\gamma}_p)$, a modified Carreau-Yasuda relation with fitting parameters r_0, r_1 and r_2 . For a full review of the model, see Klompen et al. [43] and Van Breemen et al. [44]. It should be emphasized that in this framework it is assumed that only one molecular process (the α -process, captured by τ_0) is contributing to the deformation response, although it is well known that PC shows a secondary process (or β -transition), see a.o. Bauwens-Crowet et al. [56], Klompen and Govaert [57], Mulliken and Boyce [58]. Above the β -transition strain-rate, for PC about 10^2 s^{-1} at room temperature, a different yielding behavior is shown. Since the highest strain rate in our experiments is 10^{-2} s^{-1} , so four orders in magnitude below this β -transition, we assume no contribution from this β -process.

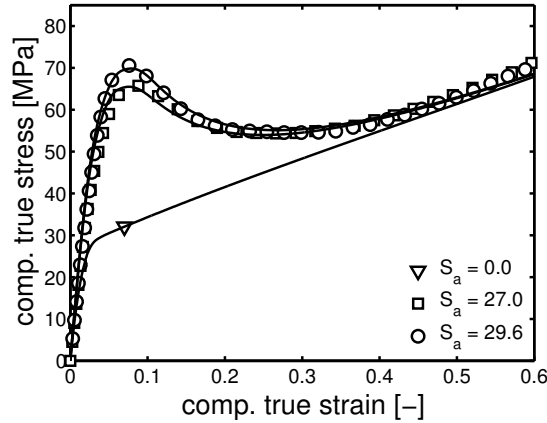


Figure 2.2: Intrinsic stress-strain response of PC with different thermal histories at a strain rate of 10^{-3} s^{-1} . Symbols are experiments, solid lines are model predictions. Data taken from Van Breemen et al. [44]

The material parameters are listed in Table 2.1. The only unknown parameter is the one that captures the present thermodynamic state of the material (S_a). This is illustrated in Figure 2.2, where the stress-strain response is shown of two PC samples with different thermal history and compared to a fully rejuvenated, un-aged, sample [44]. Since S_a depends on the processing history, its value is determined from the data of the unfilled

PC. The constitutive model is implemented in the FEM package MSC.Marc as a user subroutine. The hard TiO_2 particles are modeled as a linear elastic material with an elastic modulus of 230 GPa and a Poisson ratio of 0.27; the MBS rubber particles are modeled with the simplest rubber elastic model, neo-Hookean, with a shear modulus of 5 MPa. Note that in both cases the exact choice of the parameters is arbitrary since both moduli differ about two orders in magnitude from the modulus of the PC matrix. For each RVE three simulations are performed, to be precise: compression in each of the three perpendicular directions.

Table 2.1: Material parameters for PC, adopted from Van Breemen et al. [44].

G_r [MPa]	ν [-]	τ_0 [MPa]	S_a [-]	μ [-]	r_0 [-]	r_1 [-]	r_2 [-]	G [MPa]	$\eta_{0,ref}$ [MPa·s]
26	0.4	0.7	28	0.08	0.965	50	-3	352	$2.10 \cdot 10^{11}$

2.4 Results and Discussion

2.4.1 Experimental results

Sample preparation

DSC scans are performed after compounding the TiO_2 -filled PC batches, the resulting glass transition temperatures are shown in Figure 2.3. For the 40 vol% master batch a decrease in T_g of almost 25 °C is observed, compared to unprocessed PC. Batches diluted to 5, 10, and 20 vol% filler-content show a gradual decrease in T_g with increasing filler content. Since for PC, even far above M_e , T_g strongly depends on molecular weight [59] an interaction between PC and TiO_2 is suggested, causing degradation of the PC chains during processing. The molecular weight reduction is attributed to a hydrolytic degradation reaction of PC [60] which' rate depends on both temperature and water concentration. The strongly hydrophilic TiO_2 attracts water and, in combination with elevated temperatures during compounding, severe molecular degradation results, despite our efforts to prevent this by drying the materials prior to, and flushing with nitrogen during, compounding.

Nanoscale confinement of polymers at interfaces also result in changes in T_g and for PC this is reported for both supported and freestanding films [61–63]. Where we experience

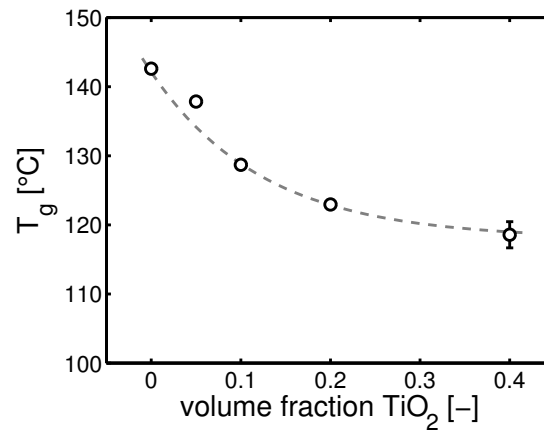


Figure 2.3: Glass transition temperature of batches containing 5, 10, 20, and 40 vol% TiO₂. The T_g of the unfilled PC is from Lexan 101R prior to extrusion. The dashed line is a guide to the eye.

a 25 °C decrease in T_g for the hard fillers, soft fillers were found to have no effect [64]. The 25 °C decrease corresponds with a length scale of approximately 40 nm [63], which translates to 25% of the polymer matrix volume for a 20 vol% TiO₂-filled system. Given all these considerations it seems plausible that degradation is the major cause for the change in T_g observed for the TiO₂-filled systems. Finally, Figure 2.4 shows that the quality of the dispersion of TiO₂ in the polymer matrix is excellent.

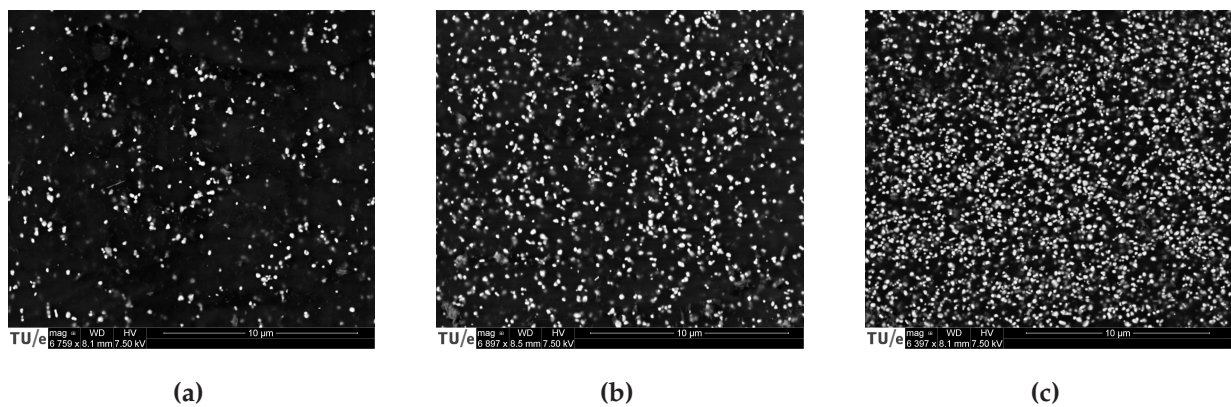


Figure 2.4: Characterization of the dispersion of TiO₂ fillers in the PC matrix, BSE-SEM pictures of a sample containing 5 vol% (a), 10 vol% (b), and 20 vol% (c) TiO₂.

Compression tests

Figure 2.5a shows the stress-strain responses of all samples at room temperature and at a constant compressive strain rate of 10^{-3} s^{-1} . Adding soft MBS fillers to the PC matrix decreases the yield stress. Remarkably, the large-strain response is unaltered (4.5 vol% MBS), or only slightly lower (9 vol% MBS), than that of pure PC. Adding hard TiO_2

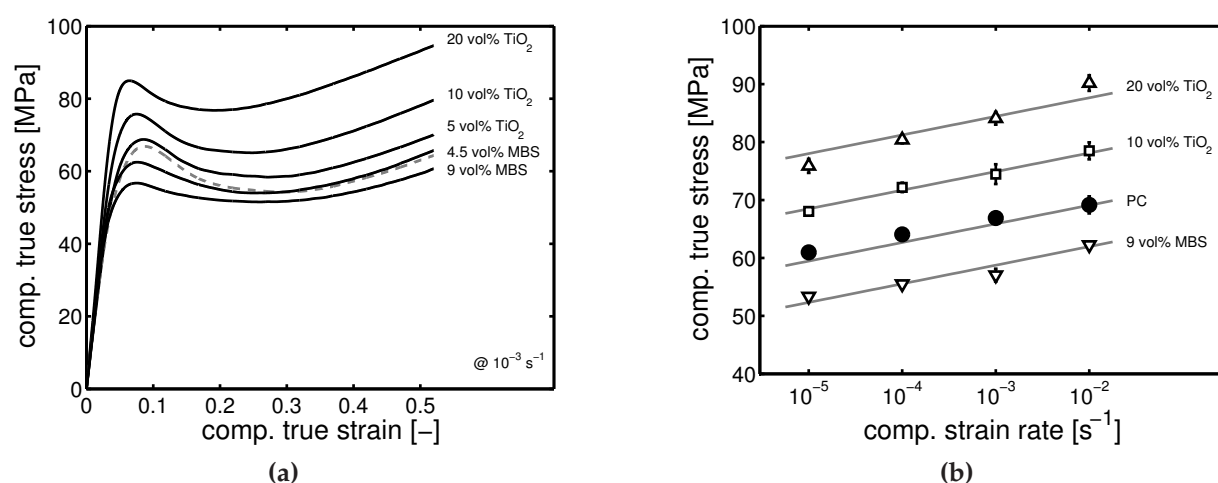


Figure 2.5: Stress-strain responses of all samples at a compressive strain rate of 10^{-3} s^{-1} and a temperature of $23 \text{ }^\circ\text{C}$, (a) and yield stress as a function of the strain rate applied (b). The grey dashed line (a) and the closed symbols (b) correspond to unfilled PC. Grey lines in (b) are a guide to the eye and, for sake of clarity only, results of the lowest TiO_2 and MBS filler-content are omitted.

fillers increases the elastic modulus and yield stress, while the large strain response shows a pronounced increase in stress values as well. Figure 2.5b gives the strain-rate dependence of the yield stress. Interestingly, fillers only change the magnitude of the yield stress; not the rate dependency.

2.4.2 Numerical results

Minimum number of particles in the RVE

Before comparing the simulations quantitatively to the experiments it is necessary to determine what the minimum size of the RVE should be. Although it is tempting to add a large number of inclusions in an RVE to account for all the possible spatial arrangements, this results in simulations that simply demand too much memory and take too

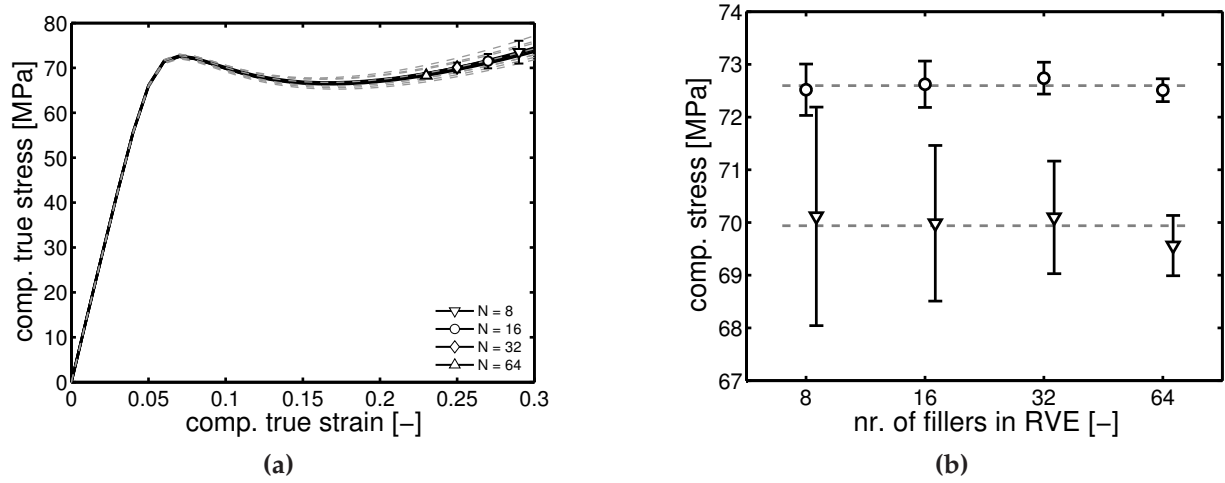


Figure 2.6: Influence of the number of spheres in an RVE. The RVEs are filled with 10 vol% hard spheres, the matrix material is PC ($S_a = 28$). (a) The mean compressive stress-strain response per set (solid lines); the dashed lines represent the bounds of the standard deviation of each set of simulations. (b) The mean stress and standard deviation at yield (circles) and at a strain of 0.25 (triangles) for each set of simulations. The dashed lines are the average over all simulations.

long to finish. An alternative is to generate multiple, but smaller, RVEs and to perform a series of simulations. To that purpose, RVEs of 10 vol% filler fraction are generated with a different number of spheres ($N = 8, 16, 32, 64$) keeping the total number of spheres per RVE-set constant, $N_{set} = \sum N = 320$. Thus, using 8 spheres, 40 RVEs are generated, for 16 spheres we use 20 RVEs, etc. The minimum distance allowed between spheres is $h_{min} = 0.25R$ and the element size is set to $0.25R$. The matrix material is modeled as PC and the inclusions as TiO_2 .

The mean and standard deviation of the stress response of each set is computed, see Figure 2.6a. The average stress response is almost the same for each set of simulations, the standard deviation decreases with increasing number of particles per RVE. This is shown in more detail in Figure 2.6b, where the mean stress and the standard deviation at yield (circles) and at a strain of 0.25 (triangles, slightly shifted to the right for clarity reasons) is shown for each set of simulations. The standard deviation clearly decreases with increasing number of particles, see the data at a strain of 0.25 (triangles), but at a strain around yield (circles) we see a clear improvement above 16 particles, while from 32 to 64 the improvement is less evident. Considering the issue of computational cost (in this case 32 particles: 500,000 elements or 64 particles: 1,000,000 elements) we conclude based on these results that the choice of 32 particles is a good compromise between

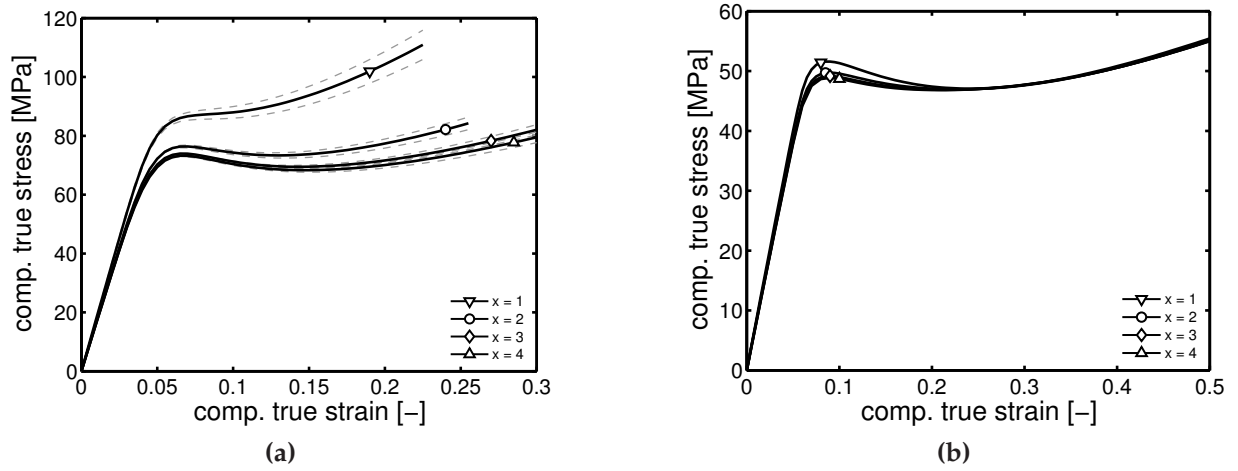


Figure 2.7: Influence of element size in an RVE. The RVE is filled with $N=32$, 20 vol% hard (a) and soft (b) particles. Solid lines are the mean of the response from the three perpendicular directions, dashed lines give the upper and lower bounds.

accuracy and computational effort.

Element size

A second issue in FEM calculations is the mesh size and, also here, a compromise is needed between reliability of the results and computational costs. In 3D, mesh refinement by a factor two increases the number of elements by a factor of eight and, since calculation times scale, at least, linearly and, at most, quadratic with the number of elements, a 8–64 increase in time results. The problem can be partly circumvented by meshing only those regions where large gradients are expected with small elements, and allow the element size to increase in the remainder of the RVE. The largest gradients are expected close to the interface and between closely packed particles. An RVE is constructed with 20 vol% of spheres and a minimum distance between the spheres allowed of $h_{min} = 0.40R$. The faces between matrix and particles are first meshed with triangular elements in four different sizes ($0.40R/x$, where $x = 1, 2, 3, 4$). The maximum size of the tetrahedral elements in the matrix-volume is set to $2x$.

The simulation results of the four different meshes are shown in Figure 2.7. With an element size of $x = 1$, the gap between two inclusions closest to one another is meshed with only one element and from Figure 2.7 it is clear that for both the hard- and soft-particle filled cases this is insufficient. A minimum of $x = 3$ proves to yield sufficiently reliable

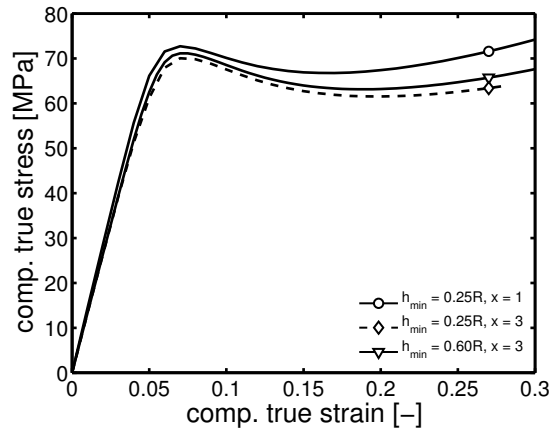


Figure 2.8: Effect of dispersion quality on the stress-strain response.

results; decreasing the element size further has only little effect. Indeed, with $x = 3$ the smallest possible gap between two inclusions consists of at least three elements, just enough to account for a deformation gradient between two inclusions. Another striking feature is that the effect of element size for the hard-particle filled system is mainly found in the large strain region, while for the soft-particle filled systems only the yield stress itself is affected, the large strain response does not change, compare Figures 2.7a and 2.7b. Locally decreasing the element size with a factor three ($x = 3$) increases the total number of elements in the RVE from 580,000 to 3.3 million, and makes the computations six times more expensive: computing up to 0.25 compressive strain takes almost two days on eight parallel CPU's (2.6 GHz Intel Xeon X5550 with 48 GB RAM). In all computations up to now, the minimum distance between two inclusions was set to $h_{min} = 0.25R$. Increasing this distance implies a better dispersion of particles in the matrix. Since we established that a minimum of three elements are needed over this distance, increasing h_{min} simultaneously reduces the number of elements required. For example for an RVE with $x = 3$ and $h_{min} = 0.60R$ only about 400,000 elements are required and the computational costs are reduced by a factor eight compared to the $x = 3$ and $h_{min} = 0.25R$ case. Despite this, the results are in reasonable agreement with the less well dispersed system of $x = 3$ and $h_{min} = 0.25R$, see Figure 2.8. From this we can conclude that by slightly constraining the freedom of the dispersion in the RVE, a large benefit in computational costs results. This seems to be an acceptable compromise.

Combining experimental and numerical results

For each filler fraction three different RVEs are generated. Each RVE consists of 32 spheres. The element size is such that at least three elements are included through

the thickness between two closely packed particles. The minimum allowed distance between spheres is set to $h_{min} = 0.60R$ for the RVEs with filler fractions up to 10 vol%, which is a compromise between computational costs without too much restricting the number of possible conformations. For the RVEs with 20 vol% fillers, h_{min} is set to $0.40R$, since higher values impose too much restriction on the spatial distribution of the particles.

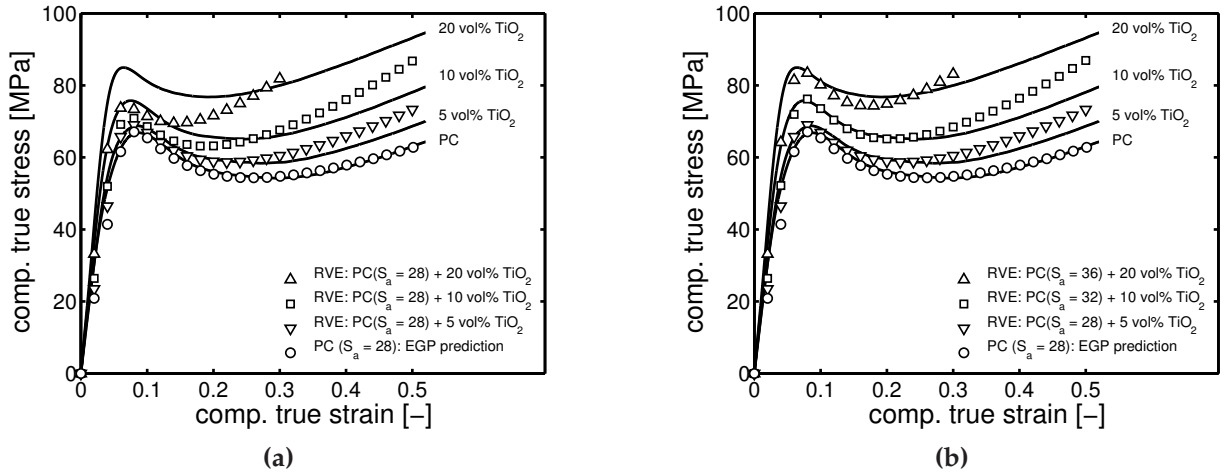


Figure 2.9: (a) Stress-strain response of compression molded PC filled with 0, 5, 10, and 20 vol% TiO_2 at a strain rate of 10^{-3} s^{-1} and a temperature of $23 \text{ }^\circ\text{C}$. Solid lines are the experimental results, symbols are the simulation results with state parameter $S_a = 28$. (b) As Figure 2.9a, now with variable S_a .

As already mentioned, the only unknown material parameter is the state parameter S_a of the PC matrix. Together with the TiO_2 -filled samples, also a batch of pure PC was prepared and a value of $S_a = 28$ was found to accurately capture its yield stress and large strain response, see Figure 2.9a. S_a depends on the processing history, but in first instance we assume the same value for all samples. The small-strain regime is somewhat under-predicted by the simulations, due to the use of a single relaxation time only. For the system filled with 5 vol% TiO_2 yield stress and the initial part of the strain softening are captured well, and only at large strains the stress response is slightly over predicted. With increasing filler content, the yield prediction is less accurate and the large-strain predictions show similar trends as found for the 5 vol%-filled sample: compared to the experiments a slightly steeper increase in stress.

Therefore we abandon the assumption of $S_a = 28$ for all samples, and allow it to adjust, see Figure 2.9b. To predict the system with 10 vol% TiO_2 quantitatively, a value of

$S_a = 32$ is needed, and for the system with 20 vol% TiO_2 , $S_a = 36$ is found. By only increasing the thermodynamic state, reflected in S_a , clearly much better predictions of the yield regime result. Adapting S_a may at first sight seem a random choice, but this is not the case. Blackwood et al. [65] provided evidence that the addition of TiO_2 leads to a densification of PC around the filler particles. Although they did not specify particle size and its extend, densification directs to enhanced and accelerated physical aging, as was found by Cangialosi et al. [66, 67] to occur for PC in confinement, in contrast to other polymers [68]. The effect is already present at length-scales even larger than the average particle size of 350 nm in our study. Since introduction of a third interphase would require indications of its thickness and age, represented by its S_a -value, our (simple) choice of defining an ‘effective aging’ for the total matrix seems justified.

A striking observation in the hard-particle filled systems is found in its strain softening after yield, which value is known to determine the materials macroscopic, tough or brittle, response. Increasing S_a mainly results in an increase in yield stress while the minimum after yield is largely unaffected, see Figure 2.10a. This is quantified by the value of yield drop $\Delta\sigma_y$, defined as the difference between yield stress and the subsequent stress minimum. Increasing the S_a from 28 to 36 results in a change in $\Delta\sigma_y$ from 12.8 to 21.1 MPa, which is 8.3 MPa. For the 20 vol%-filled sample, only and increase of $\Delta\sigma_y$ from 4.7 to 9.5 MPa is found, which is 4.8 MPa. Thus the increase in strain softening in the matrix is largely canceled out by the effect of strain amplification in the hard-particle filled systems. This is illustrated in Figure 2.10b, that shows the range of equivalent plastic strains $\bar{\gamma}_p$, as defined by Equation (2.4), in hard- and soft-particle filled systems, with macroscopic deformation. PC starts to plastically deform at 0.06 macroscopic strain in uniaxial compression; in particle-filled systems plastic deformation commences at a much earlier stage and is locally strongly amplified, but even up to applied compressive strains of 0.5 sites exist in the PC matrix that have not yet plastically deformed at all.

The MBS-filled PC samples were prepared differently and the experimental results of Engels et al. [64] are used to determine the age of the PC in the matrix. Accidentally also in this case a value of $S_a = 28$ was found to capture the yield stress properly. Figure 2.11a shows the simulation results of the RVEs using this value and, in contrast to the TiO_2 -filled systems, no extra contribution from the state parameter is required to capture the yield stress and large strain response quantitatively. Also in these samples a sequential yielding process is present, shown as a band around the plastic-deformation line of unfilled PC in Figure 2.10b, although it is less pronounced than in the TiO_2 -filled systems.

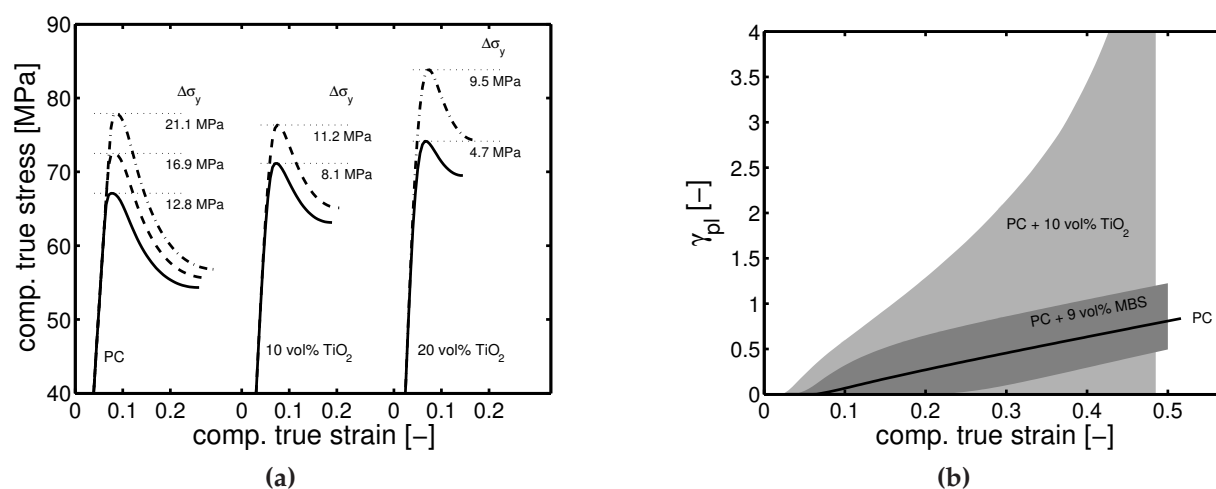


Figure 2.10: (a) Simulated stress-strain response of 0, 10, and 20 vol% TiO_2 filled PC systems at a strain rate of 10^{-3} s^{-1} and a temperature of $23 \text{ }^\circ\text{C}$. Solid lines are for $S_a = 28$, dashed lines for $S_a = 32$, and the dashed-dotted lines for $S_a = 36$. The values of the yield drop $\Delta\sigma_y$ are indicated. (b) The local equivalent plastic strain $\bar{\gamma}_p$ as a function of the macroscopically applied strain. The solid line is the response of uniaxial deformation of unfilled PC, the light grey area gives the range of $\bar{\gamma}_p$ in the matrix for 10 vol% hard-particle filled RVEs; the dark grey area gives this range for 9 vol% soft-particle filled RVEs.

Figure 2.11b shows the results of the simulations with different strain rates applied. Compared to Figure 2.5b where the lines were to guide-the-eye, here the lines are direct simulation results. It is concluded that indeed only the matrix material PC is responsible for the strain rate dependence of its composites, and that its prediction is quantitative.

Onset of failure

Up to this point only the total response in the simulations of the RVEs is considered. For the hard-particle filled systems the response in the large strain regime is over-predicted, see Figure 2.9b, caused by the fact that in the simulations perfect adhesion between particles and polymer matrix is assumed, and no failure criterion is implemented. Therefore simulations continue where in experiments samples fail, e.g. by cracks appearing close to or at the particle-matrix interface. Meijer and Govaert [13] showed that the introduction of a failure criterion in the form of a critical hydrostatic stress allows the prediction of the onset of local cavitation, resulting in brittle failure. Therefore, the max-

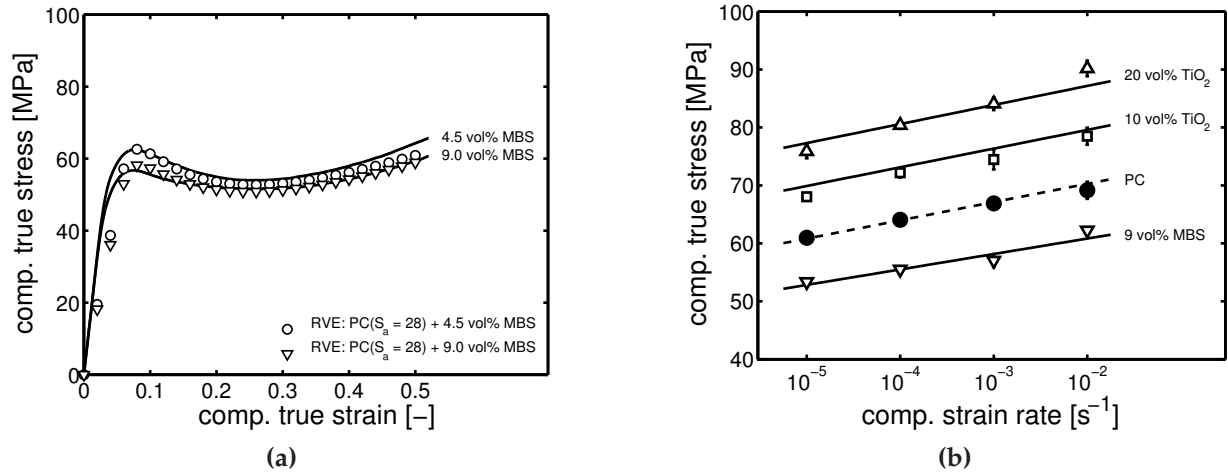


Figure 2.11: (a) Stress-strain response of PC filled with 4.5 and 9 vol% MBS at a strain rate of 10^{-3} s^{-1} and a temperature of $23 \text{ }^\circ\text{C}$. Solid lines are the experimental results, symbols are the simulation results with state parameter $S_a = 28$. (b) Yield stress as a function of strain rate applied. Symbols are experimental results, solid lines are, compared to Figure 2.5b where the lines were to guide-the-eye, the results of the simulations using proper RVEs. The dashed line is the EGP-model prediction of the rate dependence of pure PC, with experiments indicated with closed symbols.

imum value of the positive hydrostatic stress σ_{max}^h present in the RVEs' polymer matrix is determined at each increment. The stress maxima are localized since the difference in stiffness between polymer matrix and filler causes large local strains to occur.

Figure 2.12 shows the resulting maximum values as a function of the macroscopically applied compressive strain. The critical hydrostatic stress σ_c^h at which voiding for PC sets in, as mentioned in literature [47, 49–51], ranges between 80 and 95 MPa. Clearly, for the hard-particle filled systems, this value is already exceeded at 2–5% macroscopic strain, indicating that failure commenced even before the sample shows macroscopic yielding. Sequential failure in the matrix occurs and, when σ_c^h is reached, a cavity appears that locally releases the stress maximum. Upon further deformation this process continues to happen until cavities combine to form cracks; a result that becomes macroscopically visible.

Remarkably, also in the soft-particle filled systems, σ_c^h is exceeded, although it is reached only at 8–12% macroscopic strain. Where the hard-particle filled systems reach σ_c^h in earlier stages of the macroscopic deformation with increasing filler content, for soft-particle

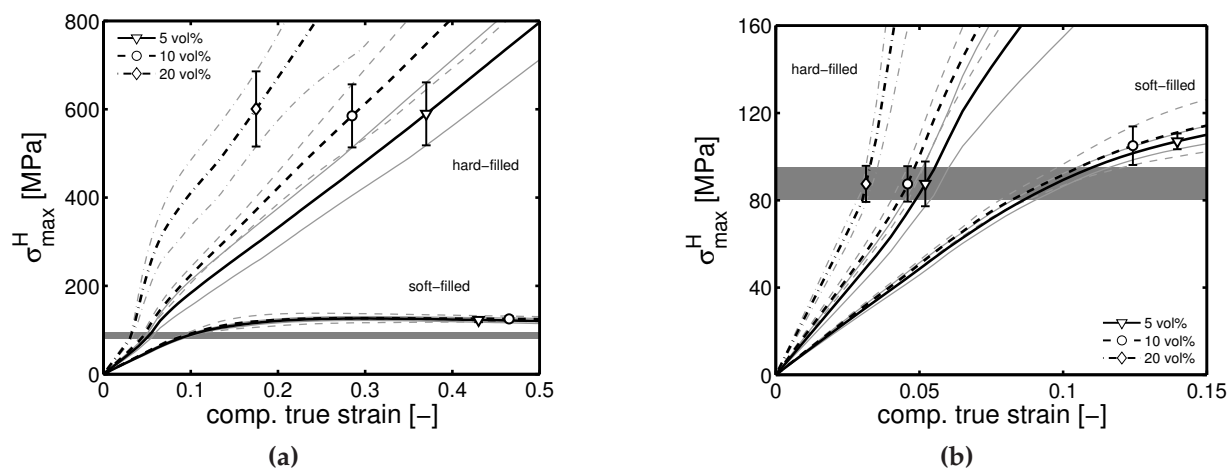


Figure 2.12: Maximum positive hydrostatic stress inside the RVEs as a function of the macroscopically imposed compressive strain. Bold lines are the mean of the different simulations, the corresponding grey lines show the upper and lower bounds. The grey area depicts the critical hydrostatic stress of PC. In (a) the complete strain region is shown, in (b) only the first 15% of macroscopic strain.

filled systems no clear trend is observed. To explain this, we consider the locations in the RVE where σ_c^h is reached. In the hard-particle filled systems this happens first between closely packed fillers positioned in an equatorial plane perpendicular to the loading direction. Increasing the filler content results in more (and stronger) interactions between failure events at different fillers. In the soft-particle filled systems the critical value is reached at the poles of the fillers along the axis of deformation. Hence, no clear effect of the filler content is observed.

2.5 Conclusions

A restricted number of 32 particle proves to be sufficient to give reliable RVE responses with little scatter, provided that the element size is sufficiently small to capture the gradients between closely packed particles. The result of an insufficient element size depends on the system: in hard-particle filled systems the large-strain response is over-predicted; in soft-particle filled systems the yield stress is over-predicted, but the large strain-response is unaffected.

Using proper RVEs it proves possible to describe key features of the intrinsic mechanical response of complex sub-micron, soft- and hard-particle filled polymer systems,

such as the increase in initial elastic modulus, in yield stress, and in strain hardening with increasing TiO_2 -content, and the decrease in initial modulus and yield stress with increasing MBS-content. All the rate-dependency in the system's response originates from the polymer matrix; fillers only change the magnitude of the stress response.

A minor shortcoming of the modeling choices is revealed in the small strain regime where the simulations under-predict the response prior to yielding since the matrix response is modeled with a single relaxation mode only. While yield and post-yield responses of the MBS-filled systems are accurately captured, some interesting discrepancies are observed for the TiO_2 -filled systems. Using S_a values of the unfilled polymer, the yield response is largely under-predicted for filler loadings of 10 and 20 vol%. Increasing S_a proves sufficient to shift the response of the simulations to the experimentally obtained values. This increased aging of the PC matrix is rationalized by observations from literature that show an increased densification, thus aging, for this specific polymer-filler combination [65] and accelerated aging of confined PC [66, 67].

In the simulations it is assumed that particles perfectly adhere to the matrix. In reality the (polymer at the) interface will fail at some local critical stress. The presence of fillers causes even in macroscopic negative loading situations, like in compression experiments, positive hydrostatic stresses to locally occur; in hard-particle filled systems at the equator, a plane perpendicular to direction of the applied macroscopic stress, in soft-particle filled systems at the poles. The simulations reveal that already at small macroscopic deformations the critical hydrostatic stress of PC is reached, implying a sequential occurrence of local failure, finally combining to grow into a macroscopic crack. Occurrence of early local damage helps explaining some of the discrepancies found between experiments and simulations in the TiO_2 -filled systems.

CHAPTER 3

Multi-mode modeling of global and local deformation, and failure, in particle filled epoxy systems

Abstract

A three dimensional Representative Volume Element is used to analyze the local heterogeneous stress and strain distributions, and the onset to failure, in a standard epoxy system filled with sub-micron sized hard and soft particles. Computations are compared with experiments performed in lubricated compression tests that reveal the intrinsic material's response. The response on the macroscopic level, and that of the matrix on RVE level, is captured by a multi-mode constitutive version of the Eindhoven Glassy Polymer model that describes the non-linear viscoelastic pre-yield, yield and post-yield behavior accurately for all deformation rates used. Compared to the single-mode description, the multi-mode variant covers the pre-yield regime correctly and for the hard-particles also the post-yield response. At a local level, multi-modes give increased stress values and more intensified critical events, which is particularly important for quantitatively predicting the onset of failure. This is successfully done by detailed RVE analyses.

Reproduced from: S. Krop, H.E.H. Meijer, and L.C.A. van Breemen. "Multi-mode modeling of global and local deformation, and failure, in particle filled epoxy systems," *Composites Part A: Applied Science and Manufacturing*, submitted for publication (2016).

3.1 Introduction

Epoxy resins are widely used in applications such as structural adhesives, coatings, electrical devices, and as matrix material in fiber reinforced or particulate composites. They have excellent engineering properties like modulus and strength, low creep, good dimensional stability and corrosion resistance. Moreover they are relatively easy to manufacture into composites [69, 70]. Epoxies are usually modified to include a dispersed second phase. Hard fillers, like in particle- or more often fiber- reinforcement, are used to create lightweight, high-stiffness composites to replace metals parts in aircrafts and wind turbines [27, 71]. Soft fillers, in the form of a dispersed rubber phase, are applied as a solution to the inherently low toughness and impact resistance of epoxies [72–74]. Toughening can sometimes even be obtained by using inorganic particles [75, 76]. Furthermore, combining these hard and soft fillers into hybrid-particulate composites shows to enhance the toughness even further [77–79].

Mechanical characterization of composites is usually done via experiments that couple the global macroscopic mechanical response to microscopic properties, and events, like particle dispersion, cavitation, crack propagation, and particle debonding. However, no direct connection is obtained between global and local properties of the structure. This represents a major challenge for material scientists, and especially understanding the onset of failure, and more importantly preventing early failure, requires a quantitative coupling of the macroscopic intrinsic mechanical response, via detailed local analyses, to critical events happening at the micro-scale. Over the years effort has been devoted to the development of models that try to use the structure to estimate the stress fields at smaller length scales. Initially, solutions for effective properties were sought using approximations based on mean-field homogenization schemes [16–19, 21, 22]. A more direct coupling between macroscopic response and local properties became only possible with the introduction of computers, that allowed simulations with increasing complexity given the continuously increasing computational power. Finite element methods (FEM) provided an excellent tool to arrive at the micro-macro coupling, first for (simplified) microstructures [25, 71, 80, 81].

Later more complexity could be built in and the extension to three dimensional analyses became possible [27, 31, 32, 82]. For further details we refer to Chapter 2, where the experimental mechanical response of model systems of particle-filled polycarbonate (PC) was compared with that resulting from FEM simulations. The microstructure was modeled with a three-dimensional periodic representative volume element (RVE)

in a finite element mesh assuming randomly dispersed, mono-sized spheres that perfectly adhere to the matrix. To account for the influence of statistical variations in the systems on the homogenized behavior, it was shown that 32 particles, with three elements between neighboring particles, are a good compromise between accuracy and computational cost. The constitutive response of the PC matrix was modeled with a one mode version of the Eindhoven Glassy Polymer (EGP) model [42–44]. The macroscopic stress-strain response was captured relatively well by the simulations, including all the rate dependencies. The simulations showed that the presence of fillers causes positive hydrostatic stresses to occur in the polymer matrix, even in the case of negative loading situations as in compression experiments. These positive hydrostatic stresses reach the critical value of PC already at small macroscopic deformations, implying a sequential occurrence of local failure; the local failure events finally combine to grow into a macroscopic crack.

Originally, the EGP model was developed for thermoplastics, but it was already shown by Govaert et al. [80] that it is well capable of describing the intrinsic response of an anhydride cured epoxy. Therefore here the approach is applied to thermoset epoxies, also filled with soft- or hard particles and a complete spectrum of relaxation modes is used. The chapter is organized as follows. First the matrix material is fully characterized. Next, compression tests are performed and experimental results are compared with the macroscopic response from the numerical simulations. Finally the local 3-D response on the inter-particle level is investigated and discussed. The part of the work presented here extends on Chapter 2, on soft- and hard-particle filled polycarbonate, and prepares for the modeling and testing of soft- and hard-particle filled thermoset epoxies as coatings in sliding friction experiments, analogous to Van Breemen et al. [12].

3.2 Experimental

3.2.1 Materials and sample preparation

The epoxy resin used is Epon 828 (Hexion Inc.), a standard diglycidyl ether of bisphenol-A (DGEBA) with an epoxide equivalent weight (EEW) of 185–192 g/eq. The curing agent is Jeffamine D230, a polypropyleneoxide diamine with an average molecular weight of 230 g/mol and an amine hydrogen equivalent weight (AHEW) of 60 g/eq, supplied by Huntsman Performance Products.

The soft-particles are polysiloxane core-shell rubbers (SR) particles, supplied by Evonik Hanse GmbH as a masterbatch of particles pre-dispersed at 40 wt% in a standard DGEBA resin (trade name Albidur EP2240-A). The particle size is specified as 0.1–3 μm . The thin shell consists of epoxy-functional molecules grafted on the elastomer core. The density of resin and elastomer fillers is assumed to be equal, which entails that weight- and volume fraction have the same value. Samples are prepared with a filler fraction of 20 vol% elastomer content by diluting the masterbatch with standard DGEBA resin. The EEW of the mixture is calculated and the hardener is added in a stoichiometric amount.

The hard-particle fillers are Ti-Pure R-706, a dry grade titanium dioxide (TiO_2) with an average particle size of 350 nm and a density ρ of 4.0 g/cm^3 , supplied by DuPont Titanium Technologies. First, the resin and hardener are mixed in a stoichiometric ratio. Subsequently, the TiO_2 particles are added in a ratio of 80/20 vol% epoxy/ TiO_2 . To calculate this ratio, a density of 1.16 g/cm^3 is assumed for the cured epoxy.

The pre-mixed samples are thoroughly stirred, degassed under vacuum, and poured into aluminium cups with a diameter of 45 mm and 30 mm in height. The samples are cured for two hours at 80 $^\circ\text{C}$ followed by three hours at 125 $^\circ\text{C}$. While preparing each batch of particle-filled samples, a control batch of unfilled epoxy was prepared following the same preparation protocol. After the curing protocol, the oven is switched off and allowed to cool to room temperature. For the compression tests cylindrical samples (\varnothing 6 mm \times 6 mm) are machined from the cured samples.

3.2.2 Testing

To determine the glass transition temperature T_g , differential scanning calorimetry (DSC) experiments are performed using a Mettler Toledo DSC823e. First, samples of approximately 15 mg are heated to 150 $^\circ\text{C}$, the subsequent scan is performed at a cooling rate of 10 K/min to 25 $^\circ\text{C}$. Uniaxial compression tests are performed on a Zwick 1475 tester, equipped with a thermostatically controlled environmental chamber. The cylindrical shaped samples are compressed between two parallel flat steel plates at constant true strain rates of 10^{-4} – 10^{-2} s^{-1} , at a constant temperature of 21 $^\circ\text{C}$. To prevent bulging due to friction between plates and samples, a thin PTFE film (3M 5480 skived plastic film tape) is added on both ends of the sample and a lubricant (Griffon PTFE spray TF 089) is applied on both contact areas between plates and samples.

3.3 Modeling

3.3.1 Constitutive modeling

For the matrix material the EGP-model is used [43] in its multi-mode form [44]. It is based on an additive decomposition of the Cauchy stress into a hardening stress σ_r and a driving stress σ_s :

$$\boldsymbol{\sigma} = \boldsymbol{\sigma}_r + \boldsymbol{\sigma}_s. \quad (3.1)$$

Here $\boldsymbol{\sigma}_r$ accounts for the stress contribution of the network, either entangled or cross-linked, and is modeled with a neo-Hookean spring with modulus G_r . $\boldsymbol{\sigma}_s$ is attributed to intermolecular interactions. It is additively decomposed into a hydrostatic (volumetric) part ($\boldsymbol{\sigma}_s^h$) and a deviatoric part ($\boldsymbol{\sigma}_s^d$) that is modeled as a combination of n parallel linked Maxwell elements:

$$\boldsymbol{\sigma}_s = \boldsymbol{\sigma}_s^h + \sum_{i=1}^n \boldsymbol{\sigma}_{s,i}^d = \kappa(J-1)\mathbf{I} + \sum_{i=1}^n G_i \tilde{\mathbf{B}}_{e,i}^d, \quad (3.2)$$

with bulk modulus κ , volume change ratio J , unity tensor \mathbf{I} , shear modulus G , and the elastic part of the isochoric left Cauchy-Green strain tensor $\tilde{\mathbf{B}}_e^d$. The specific modes are denoted by subscript $i = [1, 2, \dots, n]$.

The plastic deformation rate tensors $\mathbf{D}_{p,i}$ relate to the deviatoric driving stresses $\boldsymbol{\sigma}_{s,i}^d$ by a non-Newtonian flow rule, that for the isothermal case reads

$$\mathbf{D}_{p,i} = \frac{\boldsymbol{\sigma}_{s,i}^d}{2\eta_i(\bar{\tau}, p, S_a)}. \quad (3.3)$$

Here, the viscosities η_i depend on the total equivalent stress $\bar{\tau}$, the hydrostatic pressure p and the thermodynamic state of the material S_a . The viscosities are described by an Eyring flow rule, which has been extended to take pressure dependence and intrinsic strain softening into account:

$$\eta_i = \eta_{0,i,ref} \underbrace{\frac{\bar{\tau}/\tau_0}{\sinh(\bar{\tau}/\tau_0)}}_{(I)} \underbrace{\exp\left(\frac{\mu p}{\tau_0}\right)}_{(II)} \underbrace{\exp(S_a R(\bar{\gamma}_p))}_{(III)}, \quad (3.4)$$

where the initial viscosities $\eta_{0,i,ref}$ define the so-called reference (un-aged) state. Part I represents the stress dependence on the deformation kinetics with the characteristic stress τ_0 ; the pressure dependence, part II, is governed by the parameter μ , and part III

captures the dependency of the viscosities on the thermodynamic history via S_a . Strain softening is described by the softening function $R(\bar{\gamma}_p)$, a modified Carreau-Yasuda relation with fitting parameters r_0 , r_1 and r_2 . For a full review of the model, the reader is referred to Van Breemen et al. [44], where also the procedure to determine the spectrum of relaxation times is explained in full detail.

The constitutive model is implemented in the FEM package MSC.Marc as a user subroutine. The hard TiO_2 particles are modeled as a linear elastic material with an elastic modulus of 230 GPa and a Poisson ratio of 0.27; the rubber particles are modeled with the simplest rubber elastic model, neo-Hookean, with a shear modulus of 5 MPa. Note that in both cases the exact choice of the parameters is arbitrary since both moduli differ about two orders in magnitude from the modulus of the epoxy matrix ($E \approx 3$ GPa).

3.3.2 Microstructure

The heterogeneous microstructure is modeled with a representative volume element (RVE), a periodic cubic unit cell containing a finite number of particles in a finite element mesh. In Chapter 2, 32 particles proved to be an optimal compromise between accuracy and computational cost to account for the influence of statistical variations in the microstructure on the macroscopic response. Here, the same assumptions regarding the morphology of the microstructure are used, i.e. the particles are assumed to be spherically shaped, mono-sized, and to adhere perfectly to the matrix material. The shell-thickness of the core-shell rubber-particles is assumed much smaller compared to the particle-radius and, therefore, it is not taken into account. The size of the simulation box is fixed at $1 \times 1 \times 1$ and, with the 32 particles specified, the radius of the spheres (R) is computed from the desired volume fraction, i.e. 20 vol%.

Spheres within a defined minimum allowed distance (h_{min}) from any other sphere are rejected (if $x \leq 2R + h_{min}$). Spheres very close to or only slightly crossing the cubic cell faces are also rejected, since this would complicate meshing due to the small part crossing- or the small gap to the cubic face. The procedure to construct the RVEs was described in detail in Chapter 2 and will not be repeated here.

The RVEs are meshed with standard first-order, four-node, isoparametric three-dimensional tetrahedron elements. Since this element uses linear interpolation functions, the strains are constant throughout the element, requiring sufficiently fine meshes to obtain an accurate solution in regions with high gradients. In Chapter 2 it was shown that a min-

imum of three such elements between neighboring particles pose a good compromise between computational cost and accuracy of the macroscopic response.

3.4 Results and Discussion

3.4.1 Glass transition temperature

After curing the samples DSC scans are done and the glass transition temperature of the unfilled samples is determined to be 85 °C, for the sample filled with 20 vol% TiO₂ we find 85.5 °C, and for the sample filled with 20 vol% SR a T_g of 79 °C results. The value measured for the unfilled samples is in close agreement with those found in previous studies with the same matrix material [83–86], which indicates full conversion. As the TiO₂-filled sample shows only a minor increase in T_g compared to the unmodified epoxy, it is concluded that the hard fillers do not influence the curing of the epoxy matrix. In the case of the SR-filled samples a decrease of 6 °C is observed, when compared to the unfilled sample. A similar decrease in T_g was also reported by Chen et al. [74] for an anhydride-cured epoxy polymer system filled with the same SR-particles, but its importance was dismissed as being within the experimental error.

3.4.2 Characterization of the epoxy matrix

Experimental results

Figure 3.1a shows the stress-strain response of unfilled epoxy at three different constant compressive strain rates. Clearly, the typical intrinsic material response seen in polymer glasses is recognized. During the compression test, first an (increasingly) non-linear viscoelastic response is observed, up to a maximum in the stress (yield). This is followed by a drop in the stress response (strain softening), until another plateau is reached (lower yield). Finally, the stress increases again, strain hardening. Increasing the strain-rate results in an increase in the polymer's resistance against deformation, which is noticeable as a (constant) increase in stress starting at the yield point.

Apart from the rate-dependence, a second typical time dependent phenomenon is observed in polymer glasses: the dependence on time via the thermal history the material experienced during manufacturing and use. The influence of the thermal history for this epoxy system is illustrated in Figure 3.1b. The fast cooled sample is taken from the

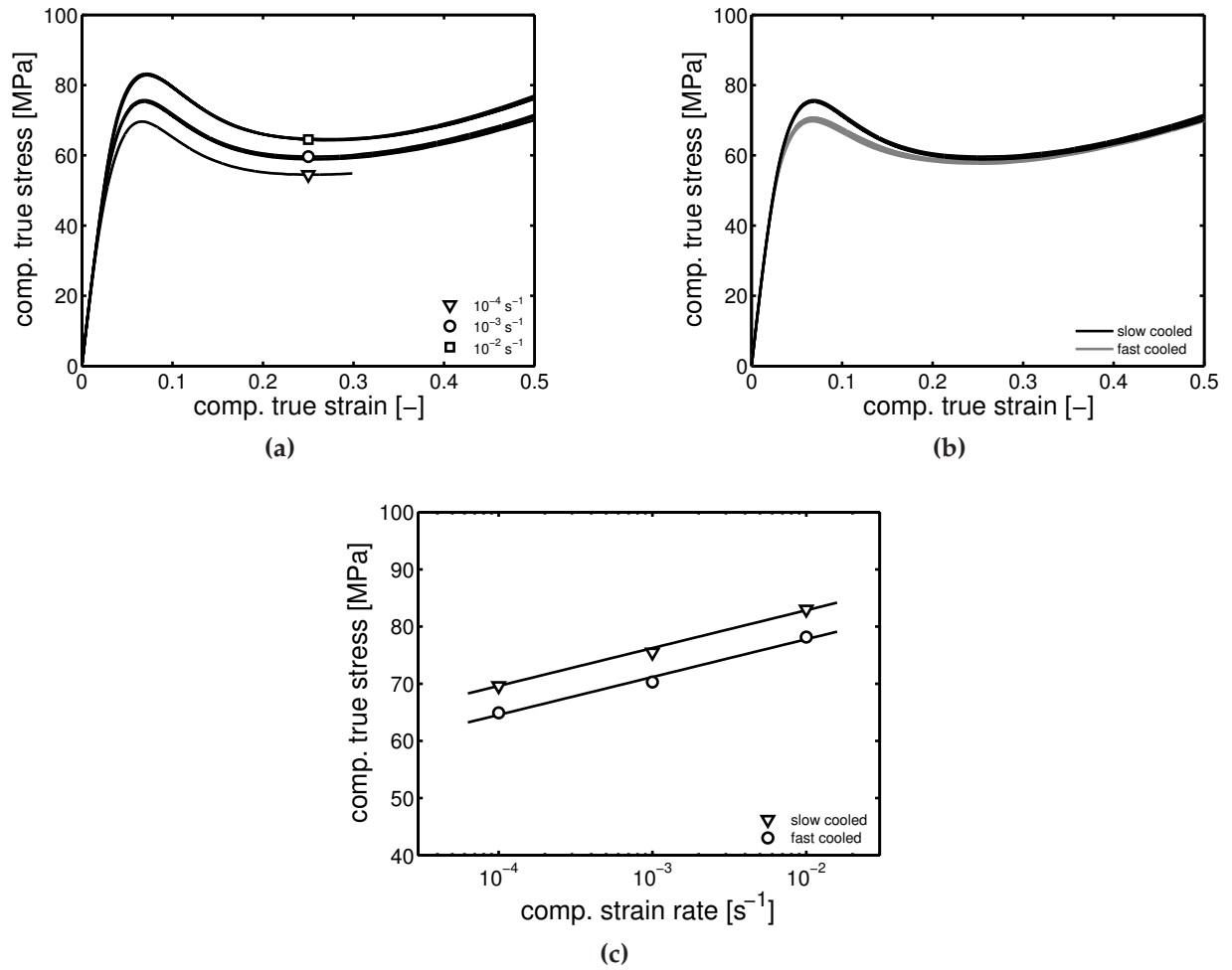


Figure 3.1: True stress as a function of true strain in uniaxial compression of the unfilled epoxy, (a) for different strain-rates applied (slow cooled after curing), and (b) for different thermal histories at a strain rate of 10^{-3} s^{-1} . (c) Effect of thermal history on the yield stress versus strain-rate applied, with symbols denoting the experimental results and lines as guide-to-the-eye.

oven immediately after curing, a cooling time of minutes results as compared to that of hours in the standard slowly cooled samples. Slow cooling results in a increase in yield stress only; the large strain response remains unaffected. This conclusively shows that a change in thermal history does not alter the degree of curing, the crosslink density, but only results in a different thermodynamic state of the polymer. This physical aging effect was also reported by G'Sell and McKenna [83] for the same epoxy system. Although the differences in intrinsic deformation for samples with different thermal history, thus a different thermodynamic state expressed in S_a , seem minor, they can have a huge ef-

fect on the macroscopic reponse, changing the material from ductile (young) to brittle (aged). Reason is that the amount of strain localization is strongly determined by the subtle interplay between strain softening after yield, causing the onset of strain localization, and the strain hardening afterwards, stabilizing by helping the material out of its localization. Although the change in cooling history dramatically affects the yield stress, it does not change the strain rate dependence, see Figure 3.1c.

Parameter determination

As explained in Van Breemen et al. [44], the determination of the relaxation spectrum requires a set of input-parameters: the strain hardening modulus G_r , the elastic bulk modulus κ , the pressure dependence parameter μ and the non-linearity parameter σ_0 , which for uniaxial compression yields

$$\sigma_0 = \frac{3}{\sqrt{3} - \mu} \tau_0. \quad (3.5)$$

The parameter μ is also required when determining G_r from the compression experiments, since

$$\sigma_s(t) = \sigma(t) - \frac{\sqrt{3}}{\sqrt{3} - \mu} G_r (\lambda^2 - \lambda^{-1}). \quad (3.6)$$

The procedure commonly employed to obtain the pressure dependence μ is by measuring the strain rate dependence of the yield stress in different loading geometries, such as in uniaxial or planar tension/compression. Prerequisite of this method is that the thermal history, reflected in the state parameter S_a , is identical for all test specimens. Since each loading geometry requires its own optimized sample shape, it is difficult to ensure the exact same thermal history for differently shaped samples [43]. This disadvantage is circumvented by using hollow cylindrical specimens which can be internally pressurized and simultaneously tested in tension or compression [87, 88]. This allows to continuously vary the state of stress from uniaxial compression to biaxial tension. With this method it was shown by Lesser and Kody [89] for model epoxy systems that μ is unaffected by the applied strain rate and the crosslink density. We will use the average value of 0.166 they found in their study. With the value of μ set, the strain hardening modulus G_r and the characteristic stress τ_0 are determined from the experimental data using Equations (3.5) and (3.6). The elastic bulk modulus κ is determined from the Poisson's ratio ν using the elastic conversion formula

$$\kappa = \frac{E}{3(1 - 2\nu)}, \quad (3.7)$$

where the Young's modulus E is obtained from the initial slope of the experimental stress-strain response. For ν a value of 0.37 is chosen, as other authors found similar values for different epoxy systems [80, 90, 91].

Now that the set of input-parameters is established, see Table 3.1, the relaxation spectrum can be determined. For a full explanation of the procedure, the reader is referred to Van Breemen et al. [44]. It proved that the pre-yield regime is accurately captured by 12 relaxation times, tabulated in Table 3.2. This only leaves the three parameters describing the shape of the softening function r_0 , r_1 and r_2 , which are obtained via a least-square data fit on the experimental softening characteristic, as described in detail by [43]. Figure 3.2a shows that with this set of material parameters the multimode EGP-

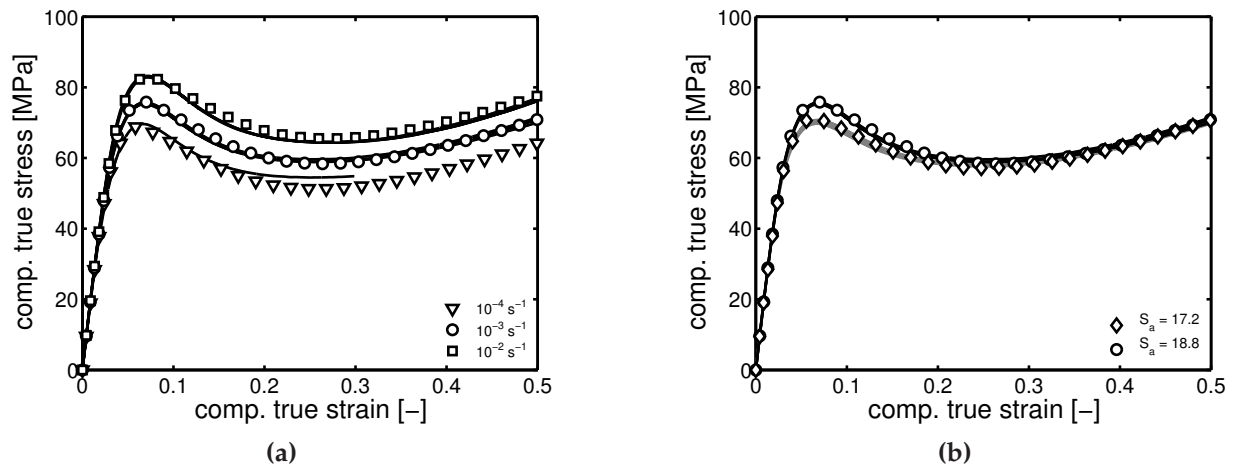


Figure 3.2: Stress-strain response of the unfilled epoxy in uniaxial compression, model predictions (symbols) compared to experimental results (solid lines), (a) for different strain rates applied ($S_a = 18.8$), and (b) for different thermal histories at a strain rate of 10^{-3} s^{-1} .

model indeed accurately captures the stress-strain response for the different strain rates applied. Moreover, by only changing the state parameters S_a , samples with different cooling histories are quantitatively captured as well, see Figure 3.2b.

3.4.3 Particle filled epoxy

Experimental results

Figure 3.3a shows the stress-strain responses of the unfilled epoxy sample and the two particle-filled samples, measured at a constant compressive strain rate of 10^{-3} s^{-1} . Each experiment was repeated at least four times and excellent reproducibility is found. Addition of 20 vol% soft SR filler results in a substantial decrease in yield stress, while simultaneously strain softening is almost completely eliminated. Adding 20 vol% TiO_2 particles results in an increased yield stress and interestingly, similar to the SR filled sample, strain softening has almost disappeared. The largest influence of the addition of hard fillers is found in the strain hardening regime. The stress response at 0.5 strain has almost doubled compared to that in the unfilled epoxy. The strain-rate dependence of the yield stress shows a slight increase for the TiO_2 -filled samples, see Figure 3.3b. Although less clear, the strain-rate dependence appears to decrease somewhat for the SR-filled sample.

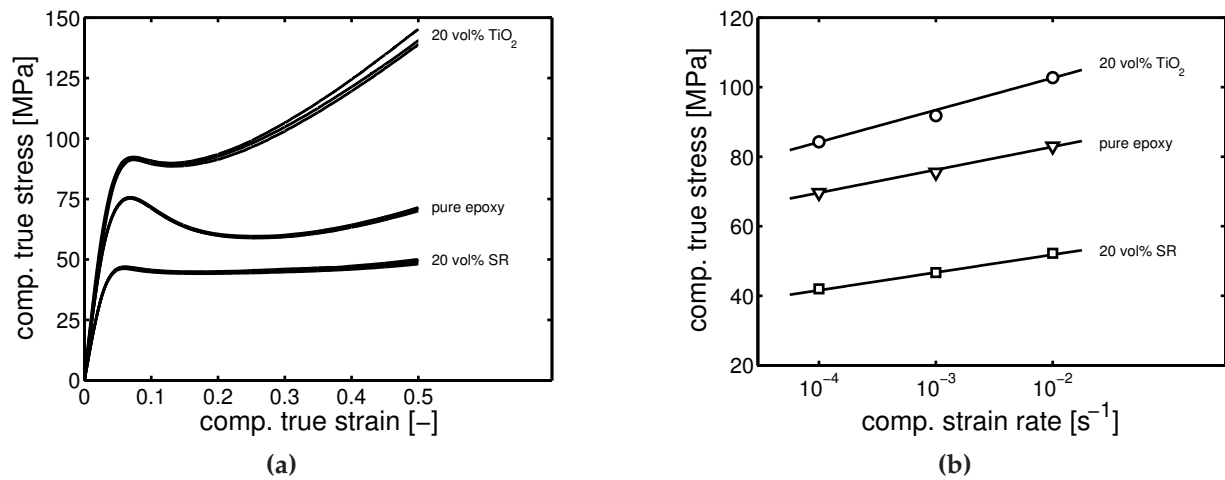


Figure 3.3: Response of particle-filled epoxy in uniaxial compression, with (a) the stress-strain response at a strain rate of 10^{-3} s^{-1} , and (b) the yield stress versus the strain rate applied. The symbols in (b) are the experimental results and solid lines are guides-to-the-eye.

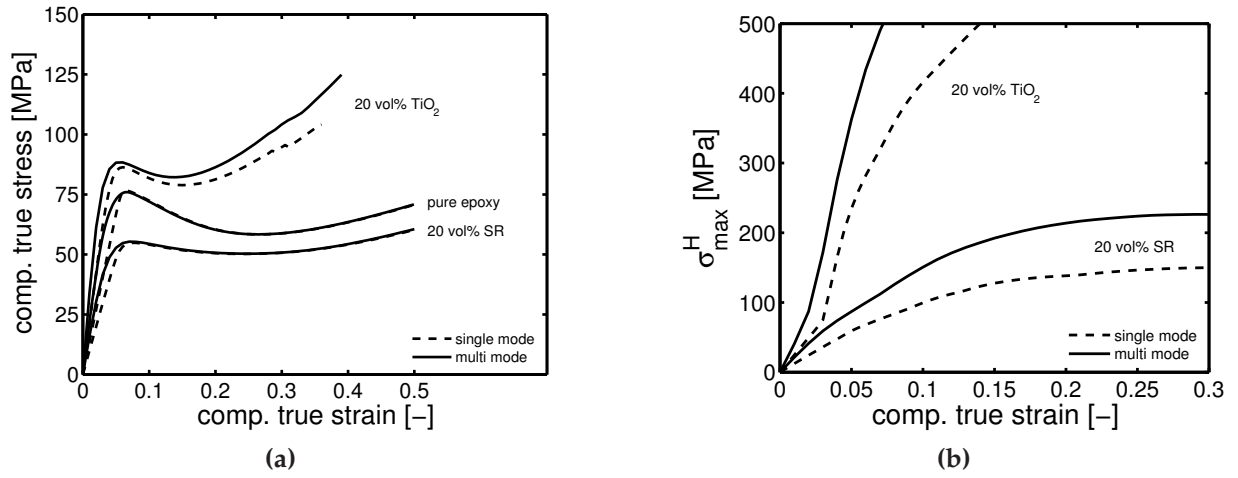


Figure 3.4: Comparison of numerical simulations using a single-mode (dashed lines) or the full multi-mode spectrum (solid lines) at a strain rate of 10^{-3} s^{-1} . (a) Simulated macroscopic stress-strain response from the 20 vol% hard- and soft-particle filled RVEs, together with the model prediction of the epoxy matrix. (b) Maximum positive hydrostatic stress inside the RVEs as a function of the macroscopically imposed compressive strain. The lines are the mean of the different RVEs.

Numerical results

Since both hard- and soft-particle modified systems contain 20 vol% fillers, the same RVEs are used, only changing the properties of the fillers. Three different RVEs are generated, each containing 32 spheres with a minimum allowed distance of $h_{min} = 0.4R$ in between these spheres. The gap between two inclusions closest to one another is meshed with at least three elements, as this gives an optimal compromise between accuracy and computational costs, see Chapter 2. The resulting RVEs contain about 900,000 elements. For each RVE three simulations are performed: compression in each of the three perpendicular directions, resulting in a total of nine simulations per model system. First, the influence of using multiple relaxation times is investigated. Simulations are performed with either the full spectrum of relaxation times from Table 3.2, or with only the first mode of the spectrum active, as was done in Chapter 2. As expected, with one mode the stress-strain response of the matrix can not be quantitatively captured anymore in the pre-yield regime. However, yield stress and the post-yield stress-strain responses of the single- and multi-mode simulations of the unfilled epoxy are identical, see Figure 3.4a. For the soft SR-filled system exactly the same result is obtained: the pre-yield regime shows a strong non-linear response when using multiple modes, while the (macroscopic) yield stress and the post-yield responses are identical. For the hard-

particle filled systems, however, things are completely different. Not only the pre-yield regime has changed when using the full relaxation spectrum, but the (macroscopic) yield stress has slightly increased and shifted to a lower strain, while with further increasing the strain the difference in stress responses between the single- and multi-mode modeling continues to increase.

These substantial differences between the responses of soft- and hard-particle filled systems originate from the fact that stress gradients in a hard-particle filled system are much more extreme. Different sites locally in the RVE start yielding at gradually increasing macroscopic strains. A sequential yielding process results that covers a large macroscopic strain region. As a consequence, also a large volume of the matrix material is still in the small strain regime, also at large macroscopic strains. This, finally, results in the different response observed when using the multi-mode spectrum. Since soft-particle fillers are intended to delocalize the stress in the first place, stress gradients are considerably less extreme during deformations. Therefore, yielding events occur in a small macroscopic strain region, which makes the results of the simulations less sensitive for the modeling choice for the matrix in the pre-yield regime. It only affects the small strain, pre-(macroscopic)-yield regime.

Apart from the macroscopic response of the filled systems, local events are also captured differently when using the multi-mode approach. This is illustrated in Figure 3.4b, where the maximum value of the positive hydrostatic stress (σ_{max}^h), present in the RVEs polymer matrix, is shown as a function of the macroscopically applied compressive strain. Although the exact values of these extrema should be interpreted with care, due to the constraints imposed on the minimum inter-particle distance h_{min} , they clearly show that the local tri-axial stresses that are predicted with the multi-mode modeling are higher compared to the predictions from the single-mode case, for both the hard- and the soft-particle filled systems.

Combining experimental and numerical results

In comparing experimental results with simulations, the full spectrum of relaxation modes is used. That leaves only one unknown material parameter: the state parameter S_a that defines the initial age of the epoxy matrix. Due to small variations during sample preparation, and subsequent cooling history, small variations in the initial age are likely to occur. Therefore, during the preparation of each particle-filled sample an unfilled control batch was prepared as well, to determine its S_a value via a compression

test. For the SR-filled sample $S_a = 18.5$ was found, while for the TiO_2 -filled sample a value of $S_a = 19.3$ fits the unfilled control sample. Results of numerical simulations using these values for S_a are shown as the symbols in Figure 3.5, where the solid lines are the experimental results from Figure 3.3.

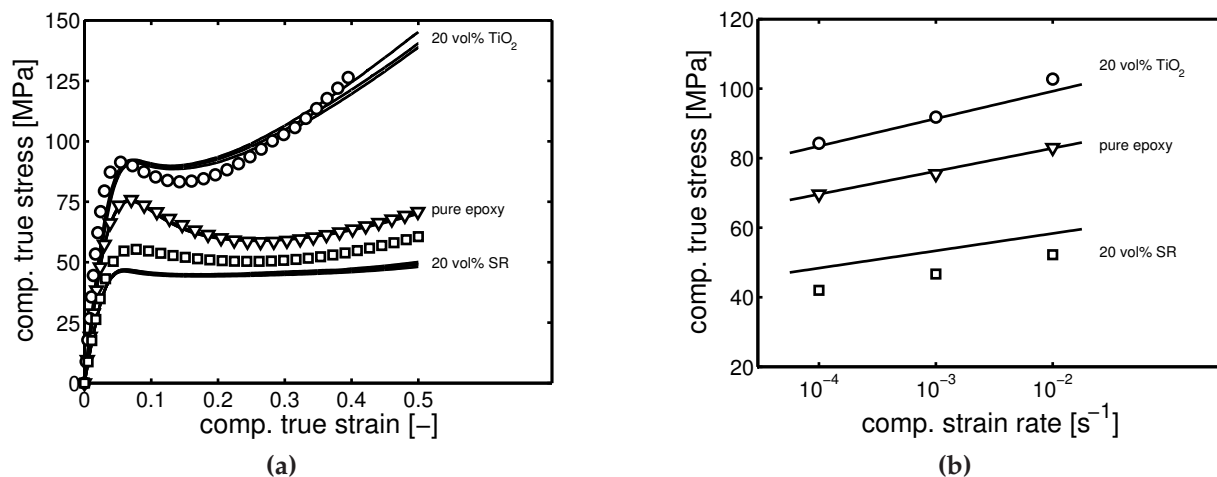


Figure 3.5: (a) Stress-strain response of the particle-filled epoxy in uniaxial compression at a strain rate of 10^{-3} s^{-1} , RVE model predictions (symbols) compared to experimental results (solid lines). (b) Yield stress versus strain rate applied, experimental results (symbols) compared with numerical predictions (solid lines).

The response of the TiO_2 -filled samples is captured well. The pre-yield regime, although only slightly over-predicted by the simulations, shows the same non-linear response as the experiments, and both the yield stress and large strain response are described quantitatively, see Figure 3.5a. Moreover, the strain-rate dependent yield stress (Figure 3.5b) is also quantitatively predicted. For the SR-filled sample, however, the simulations over-predict the stress response in all regions but the pre-yield regime where the modulus is captured well, see Figure 3.5a. Strikingly, the over-prediction of the yield stress is constant for all strain rates, see Figure 3.5b. This indicates that the rate-dependence is still captured well by the model. The explanation of the discrepancy in the magnitude of the stress response is twofold.

First, the T_g of the SR-filled sample is $6 \text{ }^\circ\text{C}$ below that of the neat epoxy. The exact cause of this decreased T_g is ambiguous, but as a result the experiments are performed at a different $T - T_g$ compared to those with the hard- and un-filled samples. Under the assumption that the epoxy matrix shows the same response at a constant $T - T_g$, compression tests are performed at a temperature $6 \text{ }^\circ\text{C}$ below the previous experiments, i.e.

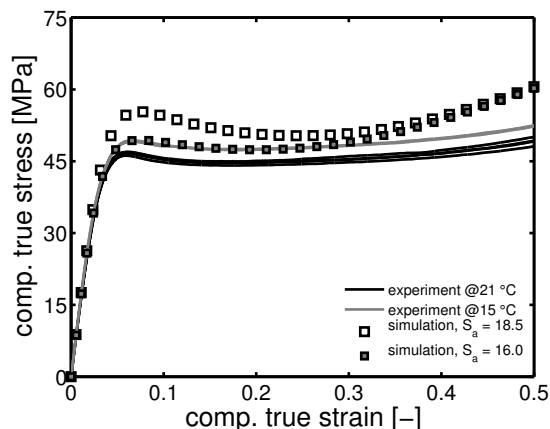


Figure 3.6: Stress-strain response of epoxy filled with 20 vol% SR at a strain rate of 10^{-3} s^{-1} . Solid lines are experimental results, symbols are simulation results. Experiments (solid lines) performed at different temperatures, and simulation results (symbols) with different S_a . Values are indicated in the legend.

at 15 °C. The effect of this change in temperature, as shown in Figure 3.6 by the gray solid line, is that the yield- and post-yield response increase with 2.5–3 MPa. Evidently, epoxy is quite sensitive to temperature changes, so care should be taken when comparing results from experiments that are either not properly temperature controlled, or from samples that show small deviations in T_g .

Second, the SR filler-particles are modified with a thin epoxy-functional layer, that confines the epoxy-matrix at the particle-matrix interface. This on one hand may help explaining the change in T_g observed, and on the other hand can lead to a change in aging rate [68, 70], although the results differ dramatically for different systems. Since still an over-prediction in stress is observed in Figure 3.6, we anticipate that for our system aging is suppressed at the particle-interface and like in Chapter 2 an effective S_a is introduced. With $S_a = 16$ the pre-yield and yield regime is accurately described, see Figure 3.6, when combined with the effect of T_g . The large-strain regime, however, is still over-predicted.

Local analyses

The method used predicts the macroscopic responses with reasonable accuracy, but moreover provides valuable information on local, inter-particle scale events. This was already demonstrated in Chapter 2, for polycarbonate, filled with either hard- or soft particles, but in that study only the extremes in the positive hydrostatic (or tri-axial)

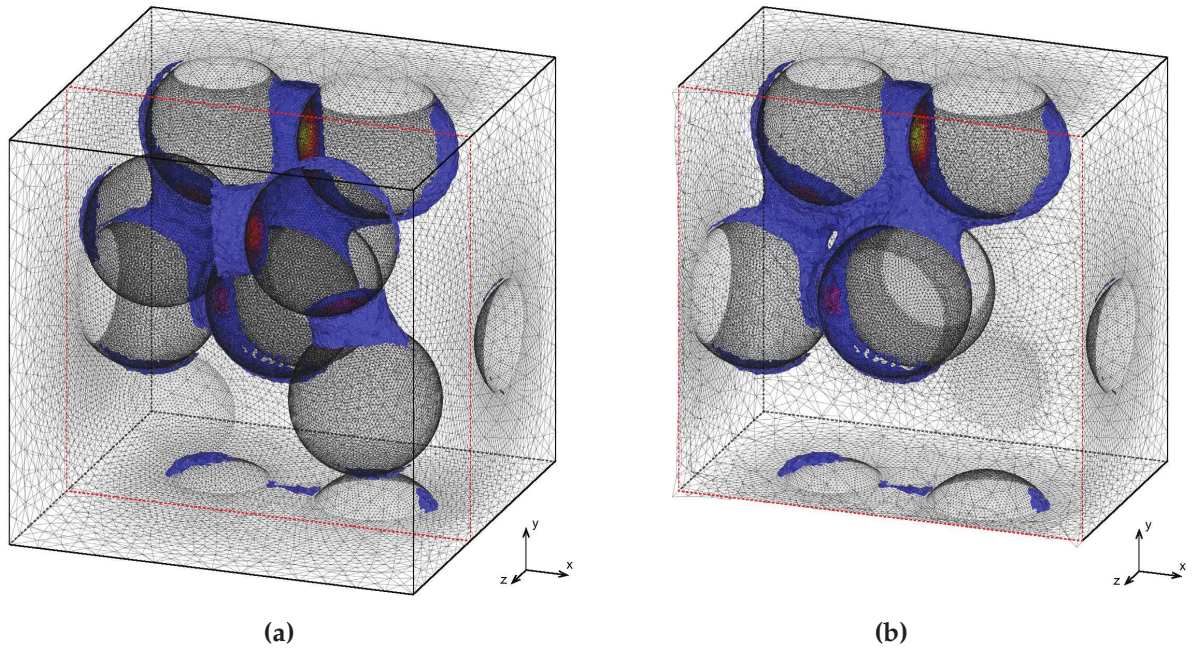


Figure 3.7: Iso-surfaces of positive hydrostatic stresses in a hard-particle filled system (lower threshold at 10 MPa). The RVE is deformed in compression in the z -direction, the macroscopic strain is 2.5%. (a) Complete RVE. (b) Front part cut away to show simultaneous interaction between four fillers.

stress were considered at each macroscopic strain increment. Figure 3.4 shows that by more accurately capturing the pre-yield regime with a multi-mode spectrum, the extremes at the local scale increase, indicating that damage commences at an even earlier stage. The hydrostatic stress in the RVE of Figure 3.4b, is one maximum value only and susceptible to the mesh quality. It is, therefore, instructive to consider the total positive-hydrostatic-stress field. They are shown in Figures 3.7 and 3.8 for the hard- and soft-particle filled systems, respectively. The figures intend to only illustrate the importance of the occurrence of local events, and therefore only eight spherical inclusions are considered. To emphasize the effect of closely packed particles, the allowable inter-particle distance is set to $h_{min} = 0.1R$.

The figures nicely demonstrate that, although deformed in compression, positive tri-axial stresses occur in the complex 3D geometries present. With hard fillers, see Figure 6.13a, these positive stresses occur between particles in an equatorial plane, perpendicular to the loading direction. In the example presented, the stress-bands between three particles is clearly recognized in the foreground. More complex situations may

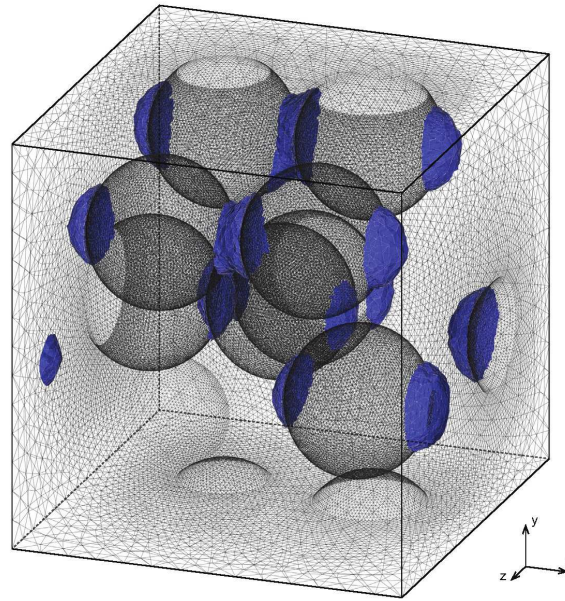


Figure 3.8: Iso-surfaces of positive hydrostatic stresses in a soft-particle filled system (lower threshold at 10 MPa). The RVE is deformed in compression in the x -direction, the macroscopic strain is 2.5%.

occur, however, as illustrated in Figure 3.7b, where the three front-most particles are via post-processing made invisible, to reveal the four particles in the background that are also in a plane. They visualize the strong, complex interaction between them.

Positive hydrostatic stresses also appear in the system filled with soft particles, see Figure 3.8. The RVE is now deformed in the x -direction and high hydrostatic stresses clearly appear at the poles of the fillers along the axis of deformation. Although the threshold value of 10 MPa implies that approximately the same volume is subjected to tensile stresses compared to the hard-particle filled system, it is obvious that the maximum stresses in the soft-particle filled systems are much lower. When the dispersion is good, these positive-hydrostatic-stress zones remain concentrated at the filler-poles, but as illustrated by Figure 3.8, in the case of two fillers closely packed in the loading direction these zones may coalesce. Thus, in the event that the critical hydrostatic stress of the matrix material is reached, this may result in damage that propagates through the areas between these fillers. Therefore, instead of improving toughness, fillers may have the opposite effect by actually promoting the propagation of cracks in localized zones through the system.

3.5 Conclusions

Multi-mode analyses of periodic, 3D RVEs are successfully applied to particle filled thermoset systems. The epoxy matrix is characterized first and it is shown that cooling rates after curing only affect the yield stress; the strain hardening regime, and the strain rate dependence, is unaffected. This indicates that, for the same curing protocol, the subsequent cooling history only induces physical aging of the polymer system. Ageing affects the intermolecular forces at the segmental scale; at large deformations this thermodynamic history is erased and the polymer network becomes dominant.

Comparing numerical simulations of the 3D, periodic, RVEs with experimental results demonstrates that especially for the hard-particle filled system key features such as yield stress, the rate-dependence of the yield stress, strain softening, and even strain hardening are all captured well. It is demonstrated that also for the particle filled systems the cooling history is influencing the intrinsic response. For the hard particle filled systems the effect is at yield; for the soft particle filled systems the effect is smeared out to larger strains, causing the apparent strain hardening modulus to decrease with increasing age.

Predictions in the small strain regime improve when multiple relaxation modes are used. Multi-mode modeling implies that the matrix material is modeled stiffer, as it is in reality. The sum of the shear moduli is larger than the shear modulus in the single-mode case, and therefore we find in the numerical simulations a more pronounced increase in local stresses with macroscopic deformation. As a result, the critical hydrostatic stress, although still experimentally to be determined for this matrix material, is reached at earlier stage than suggested in the simulations with a single mode. By multi-mode modeling, the cause of filler-induced brittleness is therefore more quantitatively understood.

3.A Material parameters

Table 3.1: *Material parameters for the epoxy matrix.*

G_r [MPa]	ν [-]	τ_0 [MPa]	S_a [-]	μ [-]	r_0 [-]	r_1 [-]	r_2 [-]
37	0.37	1.5	-	0.166	0.977	9	-3.5

Table 3.2: *Reference spectrum for the epoxy matrix.*

mode	$\eta_{0,i,ref}$ [MPa·s]	G_i [MPa]	λ_i [s]
1	$1.53 \cdot 10^5$	$4.64 \cdot 10^2$	$3.30 \cdot 10^2$
2	$1.48 \cdot 10^3$	$8.40 \cdot 10^1$	$1.77 \cdot 10^1$
3	$1.87 \cdot 10^2$	$5.09 \cdot 10^1$	$3.68 \cdot 10^0$
4	$3.82 \cdot 10^1$	$4.41 \cdot 10^1$	$8.66 \cdot 10^{-1}$
5	$4.96 \cdot 10^0$	$2.44 \cdot 10^1$	$2.03 \cdot 10^{-1}$
6	$1.41 \cdot 10^0$	$1.81 \cdot 10^1$	$7.75 \cdot 10^{-2}$
7	$3.29 \cdot 10^{-1}$	$1.80 \cdot 10^1$	$1.82 \cdot 10^{-2}$
8	$5.03 \cdot 10^{-2}$	$3.52 \cdot 10^0$	$1.43 \cdot 10^{-2}$
9	$4.48 \cdot 10^{-2}$	$1.70 \cdot 10^1$	$2.64 \cdot 10^{-3}$
10	$6.57 \cdot 10^{-3}$	$1.35 \cdot 10^1$	$4.88 \cdot 10^{-4}$
11	$1.71 \cdot 10^{-3}$	$1.49 \cdot 10^1$	$1.15 \cdot 10^{-4}$
12	$3.09 \cdot 10^{-4}$	$2.37 \cdot 10^1$	$1.31 \cdot 10^{-5}$

CHAPTER 4

Finite element modeling and experimental validation of single-asperity sliding friction on particle filled polycarbonate

Abstract

Polymer composites used as protective coatings are important, tribology-critical applications. In this study, hard or soft particle-filled model systems with a polycarbonate matrix are tested in single asperity sliding friction tests against diamond tips. A numerical approach developed to simulate scratching on unfilled polycarbonate was adapted by computing the effective material parameters for the hard and soft particle filled systems using representative volume elements. Combining this proper constitutive framework with a rate-independent friction model correlated quantitatively with the results of the current scratching experiments.

Reproduced from: S. Krop, H.E.H. Meijer, and L.C.A. van Breemen. "Finite element modeling and experimental validation of single-asperity sliding friction of diamond against reinforced and non-filled polycarbonate," *Wear*, in press (2016).

4.1 Introduction

Filled polymer systems are important in direct tribological applications, but also in scratch and wear resistant coatings. Scratching surfaces is a challenging subject because of the complex contact conditions involving many variables [11, 92–94]. Therefore, simplifications are required to arrive at well-defined contact situations and, in this chapter, we focus on the single-asperity sliding friction test, often referred to as ‘scratch test’. This test allows studying a wide range of surface mechanical properties in a controlled manner [6, 95]. Generally, friction is understood as the resistance encountered by a body sliding over another. Important for a proper description of friction is the real contact area between the two bodies, in our case the contact area between the indenter-tip and the polymer surface.

Usually this contact area is approximated by the projected area resulting from either ideal elastic or ideal plastic deformation, or a combination thereof [7, 92, 95, 96]. For polymers, characterized by their visco-elastic nature, this is a strong assumption. During scratching the polymer already relaxes in the wake of the indenter tip and to determine the real contact area proves challenging. It is either estimated by analyzing the residual scratch geometry [97] or, in the case of transparent samples, in situ monitored with a microscope mounted underneath the sample [98, 99].

The rise of Finite Element Methods (FEM) opened up new possibilities to study non-linear contact problems and simulations confirm that standard assumptions concerning contact areas are inaccurate for polymeric materials [100]. Therefore, instead, advanced FEM computations are increasingly employed to analyze complex responses in sliding friction [101–108]. Most studies provide a valuable, but still only qualitative, description of the scratch response, and quantitative predictions based on the polymers’ intrinsic mechanical response are challenging.

In our previous study we employed a hybrid experimental–numerical approach to analyze scratching a well characterized model polymer, which was unfilled polycarbonate [12]. The rate-dependent macroscopic friction force proved to be the result of a complex process. It is covered by the subtle interplay between the (size of the) bow wave in front of the indenter, that determines the deformation zone, and the rate dependent intrinsic mechanical behavior of the polymer substrate. In contrast to common practice in tribology, in this more complex, correct, detailed, and quantitative deformation analysis, a simple constant friction coefficient could be used.

Most polymers used in coatings are filled to improve mechanical properties like scratch and wear resistance [109], or to change the appearance through colorants. Additives change the intrinsic mechanical response, and could influence the adhesive interaction with the indenter tip, as expressed in the –constant– friction coefficient. This study aims to quantitatively relate the homogenized mechanical properties of well-defined, particle-filled polymer systems to their response in sliding friction. We use hard- and soft-particle filled PC, as an extension of our previous work on unfilled PC [12]. Material parameters representing the particle-filled PC samples are required in the homogenized macroscopic constitutive equation used and are computed using Three-Dimensional Representative Volume Elements (3D-RVEs); for details see Chapter 2. Comparing the results of numerical simulations with experiments confirms that also in these systems the scratch response originates from the intrinsic mechanical materials' response.

4.2 Experimental

4.2.1 Materials and sample preparation

The matrix material used for the unfilled and hard-particle filled systems is Lexan 101R, an extrusion grade of polycarbonate (PC), while for the soft-particle filled system we used Lexan 141R (Sabic Innovative Plastics, Bergen op Zoom, the Netherlands), an injection molding grade of PC, filled with 9 vol% of Paraloid EXL-2600 (Rohm & Haas). This low temperature impact modifier is a methacrylate-butadiene-styrene (MBS) core-shell copolymer. The particles have a diameter of 100 nm. The rectangular shaped scratch sample ($10 \times 10 \times 4 \text{ mm}^3$) is cut from the mid-section of an injection molded bar ($80 \times 10 \times 4 \text{ mm}^3$). The exact preparation method of the injection molded bars is described elsewhere [64].

The hard-particle filled system consists of Lexan 101R filled with 10 vol% Ti-Pure R-706 (DuPont Titanium Technologies), a dry grade titanium dioxide (TiO_2) with a particle size of 350 nm. The compounding procedure is described in full detail in Chapter 2. Pellets of unfilled and TiO_2 -filled PC are dried at 80 °C under vacuum for 12 hours before further processing. The dried pellets are heated in a mold ($12 \times 10 \times 4 \text{ mm}^3$) for 30 minutes at 190 °C and then compressed in seven subsequent intervals of 1 minute, progressively increasing the force with each step to a final force of 100 kN. Between each compression step, the force is released to allow for degassing. Finally the mold is placed

in a cold press and cooled to room temperature. To minimize the surface roughness, the samples are placed back in the hot press at 190 °C for 15 minutes, and then compressed with a pre-heated optically flat steel plate at a 100 kN normal force for 5 minutes. During this compression step, spacers ensure a uniform thickness of 3 mm. To remove stresses in the surface layer introduced during the preparation process, the sample is placed in an oven at 190 °C for 15 minutes and subsequently air-cooled to room temperature.

4.2.2 Testing

The single-asperity scratch experiments are performed with a Nano Indenter XP (MTS Nano-Instruments, Oak Ridge, Tennessee), extended with the lateral force measurement option. During the scratch experiments, a constant normal load of 300 mN is applied. After the initial indentation step, a constant sliding velocity is applied, ranging 0.1–100 $\mu\text{m/s}$. The conical diamond indenter tip used for all scratch experiments has the following specified dimensions: 90° top angle and 50 μm top radius. The indenter setup is mounted on a vibration isolation table. Thermal and acoustic disturbances are prevented by a cabinet that encloses this whole system. Experiments are performed at room temperature.

4.2.3 Experimental results

The scratch response at 0.1 $\mu\text{m/s}$ is shown in Figure 4.1. The lines representing the measurements are the average of at least 3 consecutive experiments with identical input parameters. The response of the unfilled-PC sample is nearly identical to that reported by Van Breemen et al. [12]. In the penetration into the surface (Figure 4.1a), three points of interest are observed: (i) initial indentation, (ii) with the onset of sliding the contact area decreases compared to initial indentation (the wake of the indenter detaches from the substrate), which results in an increased penetration depth, and finally (iii) a steady state is reached at a lower penetration depth due to the formation of a bow wave in front of the indenter-tip. The effect of filler particles embedded in the PC matrix is as expected. Hard TiO_2 -fillers increase the resistance against deformation, resulting in a decreased penetration depth, whereas this resistance is decreased by the soft MBS-particles, resulting in an increase in penetration. The lateral-force response, see Figure 4.1b, is somewhat less straightforward. With hard fillers the penetration has decreased compared to unfilled PC, and a smaller contact area between the two bodies results. As a consequence, the lateral force decreases, despite of the higher resistance to deformation of this substrate material itself. This influence is similar to that of the slid-

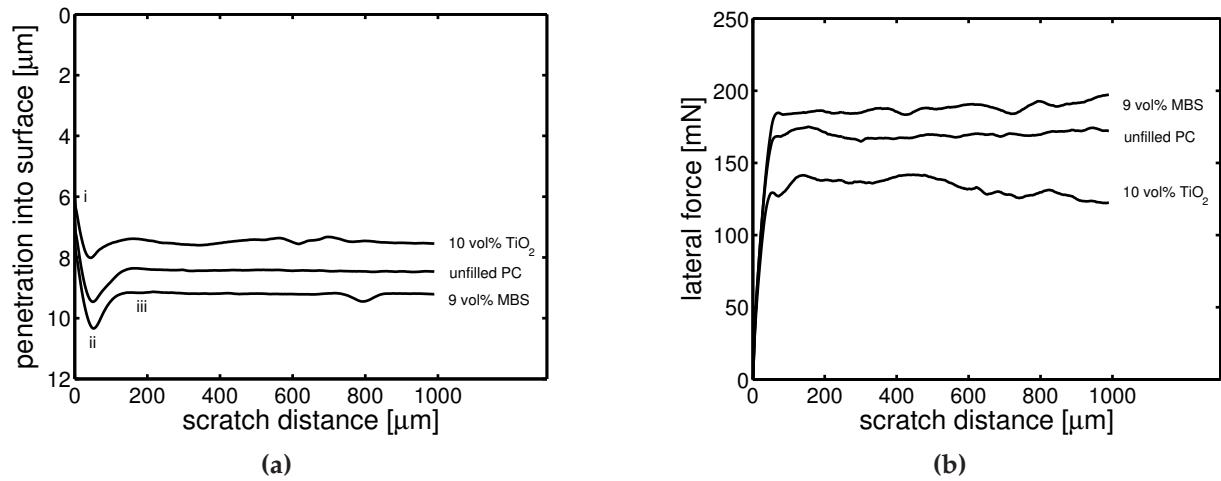


Figure 4.1: Penetration into the surface (a) and lateral friction force (b) as a function of scratch distance for unfilled PC, and PC filled with TiO₂- or MBS-particles. Scratch velocity is 0.1 μm/s and normal force applied is 300 mN.

ing velocity, where higher rates give also higher resistances to deformation resulting in a lower lateral force. The opposite effect is observed with the soft fillers.

Figure 4.2 shows the steady state response (region iii) as function of the sliding velocity applied. Since the yield stress of PC depends linearly on the logarithm of the strain rate, see Figure 4.4b, the velocity-axis is chosen logarithmic, and indeed a linear dependence of the scratch response on the logarithm of the rate is found for all three systems. The addition of filler particles results in a vertical shift of the penetration into the surface only, the velocity-dependence itself is unaffected, see Figure 4.2a. Figure 4.2b confirms that the influence of adding particles on the lateral friction force is less straightforward. The hard-particle filled samples show, compared with the unfilled ones, a constant shift in friction force over the whole velocity-range, which is expected since this is also the case for the surface penetration. For the soft-particle filled sample, no clear change in the lateral-force response results when compared to the unfilled samples over the whole velocity range, despite a 10% increase in penetration depth. At the lowest sliding velocity a slightly higher friction force is found, see also Figure 4.1b, while at the higher velocities a somewhat lower force results. The discrepancy is partly due to inaccuracies in measurements at the lowest speed, see the error bar in Figure 4.2b.

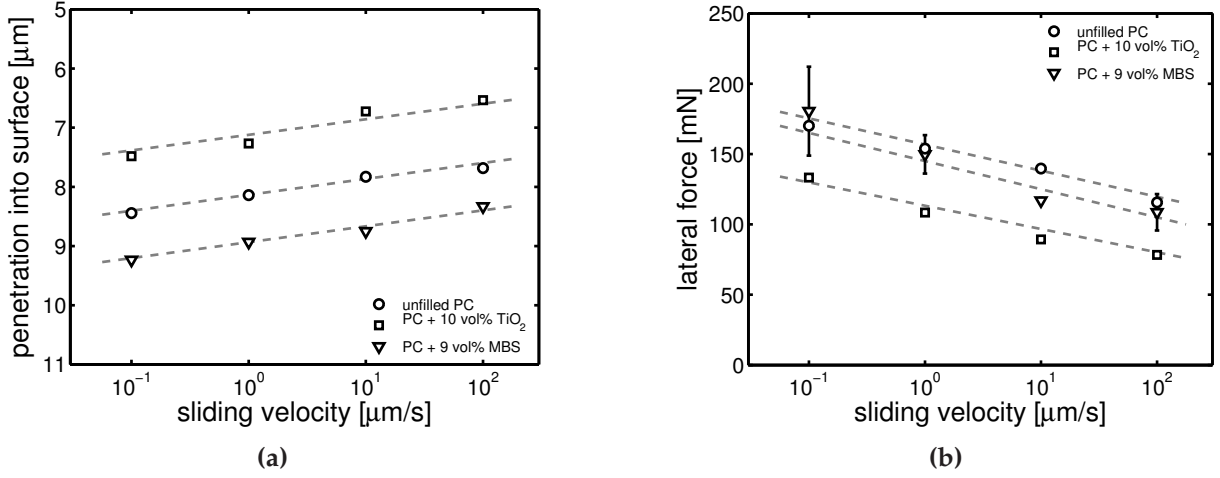


Figure 4.2: The mean of the steady-state penetration into the surface (a) and lateral friction force (b) as a function of scratch velocity for unfilled PC, and PC filled with TiO₂- or MBS-particles. Symbols are experiments and dashed lines are to guide the eye only.

4.3 Modeling

4.3.1 Constitutive model

The constitutive model employed is the EGP model [43, 44]; it is based on an additive decomposition of the Cauchy stress into a hardening stress σ_r and a driving stress σ_s :

$$\sigma = \sigma_r + \sigma_s, \quad (4.1)$$

where σ_r accounts for the stress contribution of the entangled network, modeled with a neo-Hookean spring (G_r), and σ_s is attributed to intermolecular interactions. σ_s is additively decomposed into a hydrostatic (volumetric) part (σ_s^h) and a deviatoric part (σ_s^d), where the latter is modeled as a combination of n parallel linked Maxwell elements.

$$\sigma_s = \sigma_s^h + \sum_{i=1}^n \sigma_{s,i}^d = \kappa(J - 1)\mathbf{I} + \sum_{i=1}^n G_i \tilde{\mathbf{B}}_{e,i}^d, \quad (4.2)$$

with the bulk modulus κ , the volume change ratio J , the unity tensor \mathbf{I} , the shear modulus G , and the elastic part of the isochoric left Cauchy-Green strain tensor $\tilde{\mathbf{B}}_e^d$. The specific modes are denoted by subscript $i = [1, 2, \dots, n]$. The plastic deformation rate tensors $D_{p,i}$ relate to the deviatoric driving stresses $\sigma_{s,i}^d$ by a non-Newtonian flow rule,

that for the isothermal case reads

$$D_{p,i} = \frac{\sigma_{s,i}^d}{2\eta_i(\bar{\tau}, p, S_a)}. \quad (4.3)$$

Here, the viscosities η_i depend on the total equivalent stress $\bar{\tau}$, the hydrostatic pressure p and the thermodynamic state of the material S_a . The viscosities are described by an Eyring flow rule, which has been extended to take pressure dependence and intrinsic strain softening into account:

$$\eta_i = \eta_{0,i,ref} \underbrace{\frac{\bar{\tau}/\tau_0}{\sinh(\bar{\tau}/\tau_0)}}_{(I)} \underbrace{\exp\left(\frac{\mu p}{\tau_0}\right)}_{(II)} \underbrace{\exp(S_a R(\bar{\gamma}_p))}_{(III)}, \quad (4.4)$$

where the initial viscosities $\eta_{0,i,ref}$ define the so-called reference (un-aged) state. Part I represents the stress dependence on the deformation kinetics with the characteristic stress τ_0 ; the pressure dependence, part II, is governed by the parameter μ , and part III captures the dependency of the viscosities on the thermodynamic history via S_a . Strain softening is described by the softening function $R(\bar{\gamma}_p)$, a modified Carreau-Yasuda relation with fitting parameters r_0 , r_1 and r_2 . This model is implemented as a user subroutine in the FEM package MSC.Marc. The material parameters for PC are taken from Van Breemen et al. [44] and are summarized in Table 4.1, with the reference spectrum in Table 4.2.

4.3.2 Homogenization procedure

For the particle-filled systems homogenized material parameters are used, which is justified by the two orders of magnitude difference in length scale between the filler particles ($<0.5 \mu\text{m}$) and the indenter tip ($50 \mu\text{m}$). Moreover, directly capturing the detailed micro-structure in a finite element mesh is unfeasible since the simulation box would contain over 10^6 particles. Alternatively, application of the ML-FEM, multi-level finite element method, with RVEs in the integration points of every element [110], and over 30 particles in each RVE, is impossible in 3D, given similar arguments about limitations in storage and computation time. For the homogenization procedure we use a combination of experimental results and numerical simulations on 3D representative volume elements (3D-RVEs) of the particle-filled model systems, as presented in Chapter 2.

The 3D-RVEs are periodic cubic unit cells containing 32 particles that are used as a simplified model for the heterogeneous micro-structure. Particles are assumed spherical,

mono-sized, and with perfect adhesion to the PC matrix. The random spatial distribution of the spheres in the 3D-RVEs is generated in a MATLAB (The Mathworks Inc.) program using a build-in random number generator. With the number of spheres fixed, their radius (R) is computed from the desired volume fraction. For each generated coordinate it is checked whether it fulfills a minimal allowed distance ($h_{min} = 0.6R$) to its closest neighbor: it is rejected if $x \leq 2R + h_{min}$. After each rejection a new coordinate is generated and checked, until the desired number of spheres is placed in the simulation box. Spheres crossing the cubic cell faces are copied to the opposite side to obtain periodicity. A finite element mesh of the 3D-RVE is generated, ensuring periodicity of the opposite cell faces and a minimum of three elements between closely packed spheres. An example of a 3D-RVE is shown in Figure 4.3a. With the limited amount of 32 fillers, this 3D-RVE already contains 10^6 elements. As mentioned before, a simulation box for direct scratch simulations requires about 10^6 spheres. Clearly this is simply impossible to capture in a finite element mesh, illustrating the need for homogenization.

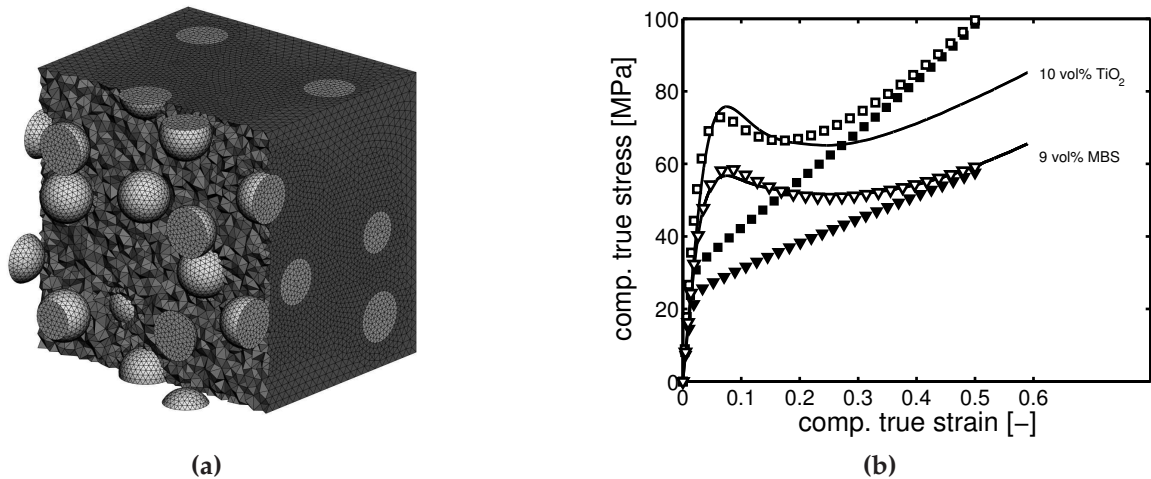


Figure 4.3: (a) Example of a meshed RVE with part of the matrix made invisible. (b) Stress-strain response of PC filled with 10 vol% TiO_2 or 9 vol% MBS, at a strain rate of 10^{-3} s^{-1} and a temperature of $23 \text{ }^\circ\text{C}$. Lines are experimental results taken from Chapter 2. Symbols are the result of FE simulations of the RVEs, using either $S_a = 28$ (open symbols) or $S_a = 0$ (closed symbols) for the PC matrix.

In these 3D-RVEs, the TiO_2 particles are modeled as a linear elastic material with an elastic modulus of 230 GPa and a Poisson ratio of 0.27; the rubber particles are modeled neo-Hookean with a shear modulus of 5 MPa. Simulations are performed in both uniaxial tension and compression loadings at different strain rates, to obtain homogenized material parameters that will be used in the scratch simulations. Figure 4.3b

shows the stress-strain response in compression, obtained using $S_a = 28$ for the PC matrix (open symbols), compared to experimental results taken from Chapter 2. The response of the MBS-filled sample is captured well by the simulations, including the initial slope, the yield point, subsequent strain softening, and the strain hardening regime. The TiO₂-filled sample is also captured well initially, but in the strain softening regime the response from the 3D-RVEs starts to deviate from the experiment: the RVE simulations show a more pronounced strain hardening response. In Chapter 2 this was attributed to the accumulation of damage in the system which becomes macroscopically noticeable above 20% strain and, since damage is not incorporated in the RVE-simulations, an over-prediction results. Therefore, for the filled systems, we take the effective strain hardening modulus G_r at large deformations directly from the experimental stress-strain responses.

Comparing simulations with experiments, the values for τ_0 , μ and the Poisson's ratio ν are obtained. The elastic bulk modulus κ is determined using the elastic conversion formula

$$\kappa = \frac{E}{3(1 - 2\nu)}, \quad (4.5)$$

where the Young's modulus E is obtained from the initial slope of the stress-strain response. The reference (or rejuvenated) state of the filled systems ($\eta_{0,r}$) is obtained by setting $S_a = 0$ for the PC matrix, see the closed symbols in Figure 4.3b. With the set input-parameters established, the relaxation-time spectrum can be determined. The material parameters are tabulated in Table 4.3 and the relaxation spectra in Tables 4.4 and 4.5. Figure 4.4a shows the experimental stress-strain responses of the unfilled and particle filled systems, taken from Chapter 2, compared to the EGP-model descriptions using this set of material parameters. The rate-dependence is also captured well, as shown in Figure 4.4b where the yield stress for different strain-rates is compared to the model predictions.

4.3.3 FE mesh and friction modeling

For the scratch simulations only half of the surface is meshed, since the problem analyzed is symmetric in the plane perpendicular to the sliding direction. The meshed area is $0.2 \times 0.2 \times 0.8 \text{ mm}^3$, see Figure 4.5, and the dimensions of the mesh are chosen such that the edges have no influence on the stress field. To reduce the total amount of elements, only the mesh in the region of interest is refined using the automatic local adaptivity function of Marc, resulting in a total of 66936 linear brick elements. The

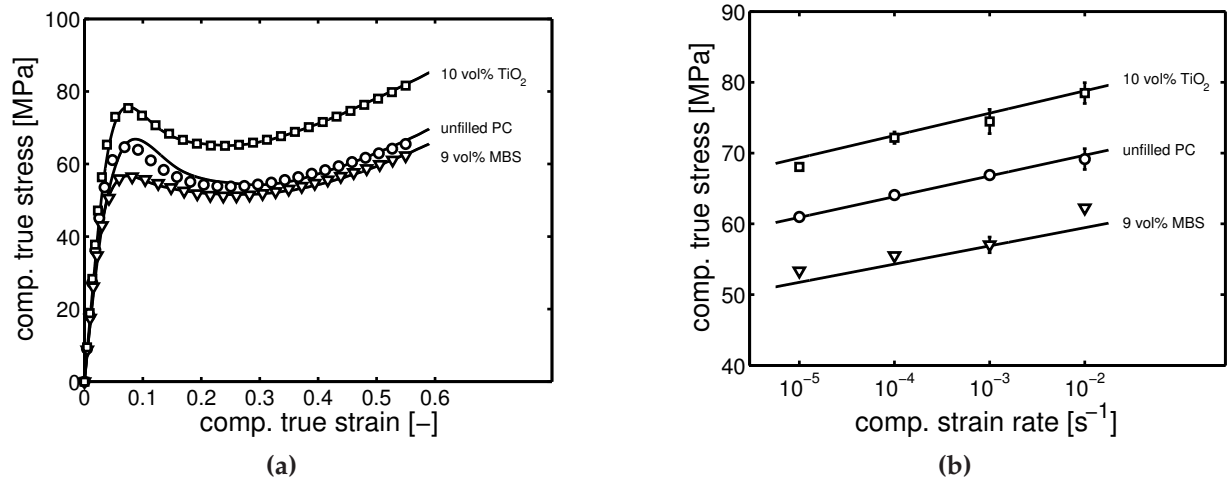


Figure 4.4: (a) Stress-strain response of unfilled PC, and PC filled with 10 vol% TiO₂ or 9 vol% MBS, at a strain rate of 10^{-3} s^{-1} and a temperature of 23 °C. Lines are experimental results taken from Chapter 2, symbols are the model predictions. (b) Yield stress as a function of the strain rate applied. Symbols are experimental results and lines are the model predictions.

symmetry plane is fixed in z-direction and the sides are restrained in z- and y-direction. Scratching occurs from the top and the sliding velocity is prescribed to the meshed block in the negative x-direction. The tip geometry is modeled as a rigid impenetrable surface. A control node on the indenter's surface is used to prescribe the normal force and to retain the indenter in x- and z-direction.

Friction is considered as a complex physical phenomenon, where complexity finds its origin in interactions at the molecular scale up to the micrometer scale. It moreover involves the influences from surface roughness, temperature, contact stresses, combination of indenter- and sample-material, etc. Usually tribology uses simple analyses where all complexity is incorporated in the friction coefficient, the ratio between lateral and normal force, and also in MSC.Marc several friction models are implemented. We here adapt a different approach, focussing on introducing more complexity in the local deformation processes, meanwhile simplifying the friction model [12]. We select the most simple one, Coulomb friction, which is characterized by a constant, velocity independent, friction coefficient μ_f :

$$\|\vec{f}_t\| < \mu_f f_n \quad (\text{sticking}) \quad \text{and} \quad \vec{f}_t = -\mu_f f_n \vec{t} \quad (\text{relative sliding}). \quad (4.6)$$

When a node is in contact with the rigid indenter-surface, the node's normal force (f_n) and relative sliding velocity ($\vec{v}_r = \|\vec{v}_r\| \vec{t}$) with respect to the rigid surface are deter-

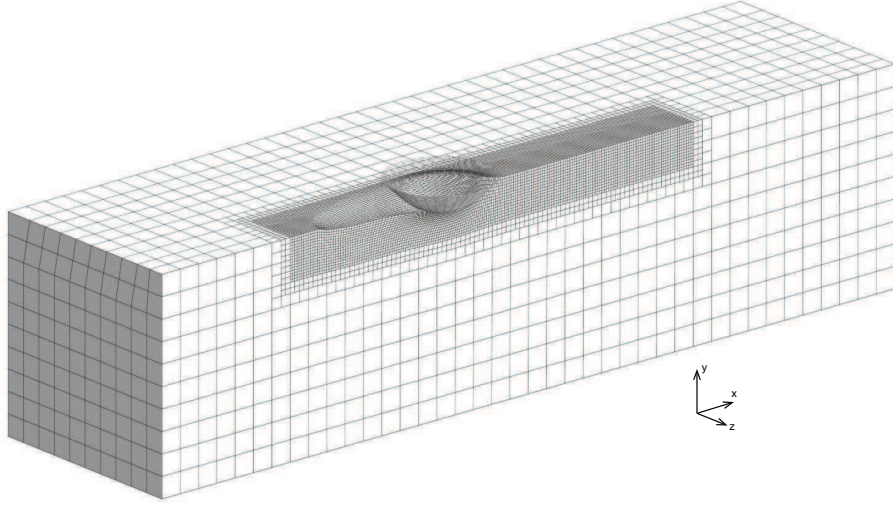


Figure 4.5: *Finite element mesh for the scratch simulations.*

mined, and evaluating these gives the tangential (friction) force \vec{f}_t , which, in the case of relative motion, has opposite direction to \vec{v}_r . The friction force has a step function behavior when the node switches from sticking to relative motion (and vice versa), and to avoid numerical difficulties arising from this discontinuity, the step function is approximated with an arctangent model:

$$\vec{f}_t = -\mu_f f_n \frac{2}{\pi} \arctan \left[\frac{\|\vec{v}_r\|}{\delta} \right] \vec{t}. \quad (4.7)$$

The interpretation of δ is the value of the relative velocity below which sticking occurs.

4.3.4 Influence of tip geometry

The scratch response, in particular the penetration depth, proved to be surprisingly sensitive to the precise geometry of the indenter tip. An optical profilometer (Sensofar Plu 2300) is used to measure the profile of the tip used, see Figure 4.6a. It appears that, in contrast to the specifications, the top of the indenter-tip is not spherical but somewhat flattened. The sensitivity to small deviations from perfect symmetry is demonstrated by comparing three responses: the indenter tip modeled according to (1) the specified geometry, (2) the flattened top part, and (3) the flattened top part of the Sensofar image. All three geometries are taken axisymmetric, and their cross-sections are shown in Figure 4.6b. For the simulations the material parameters of unfilled PC are

used, at $0.1 \mu\text{m/s}$ sliding velocity, and using a local friction coefficient of $\mu_f = 0.25$.

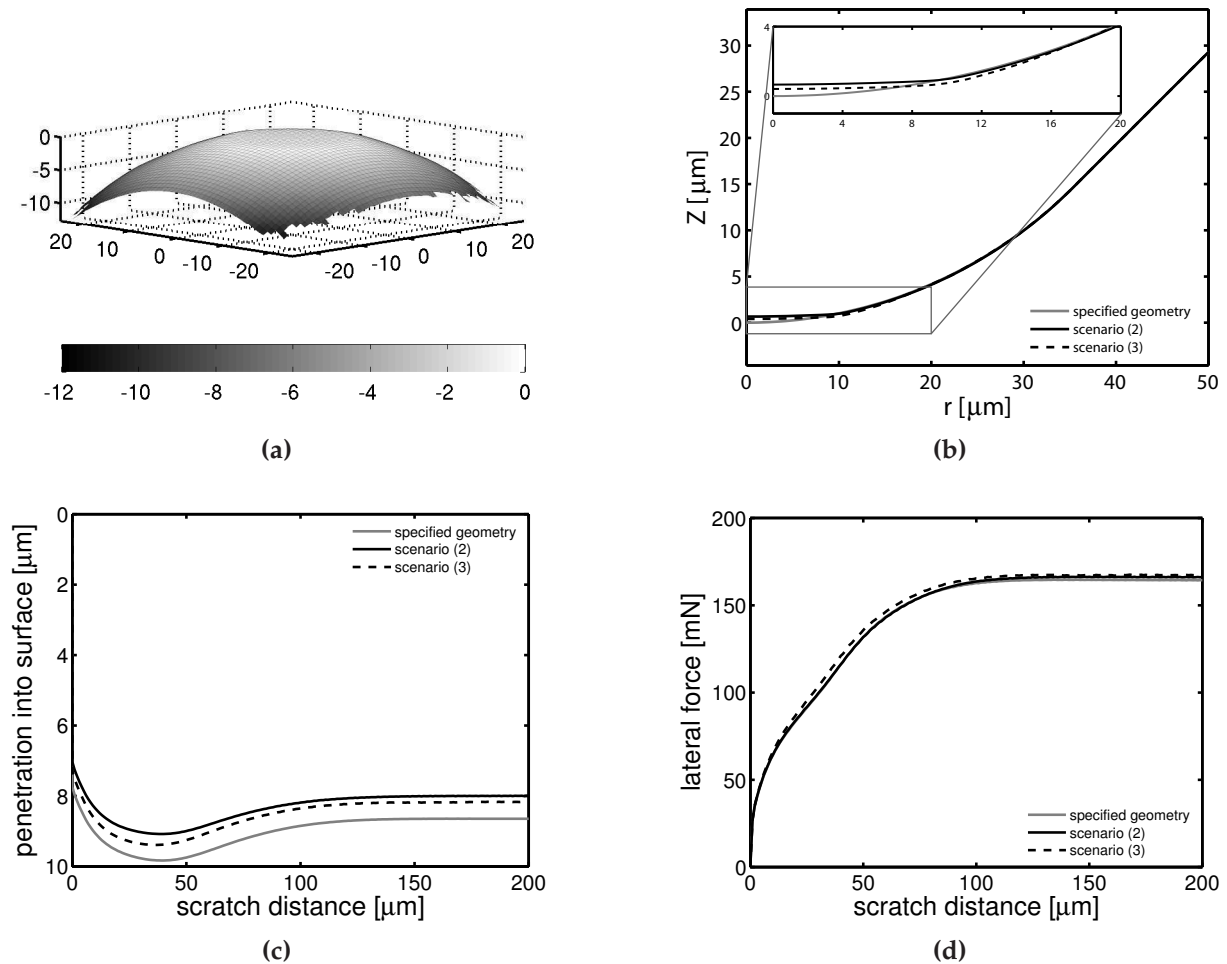


Figure 4.6: Influence of exact tip geometry. (a) 3D-view of indenter-tip geometry as it is determined with an optical profilometer. Dimensions are in micrometers. (b) The cross section of the indenter-tip geometries that are used in the simulations. This results in a difference in scratch response: (c) penetration into the surface and (d) the lateral friction force. In these simulations the material parameters of unfilled PC and $\mu_f = 0.25$ are used.

The resulting vertical-displacement responses are shown in Figure 4.6c. Compared to the specified geometry, for the slightly flattened top the penetration into the surface decreases by approximately 8%. Even the small difference in shape between scenarios (2) and (3) results in a 2% difference in penetration response. Remarkably, the lateral friction force is nearly insensitive to these differences in indenter geometry, see Figure 4.6d.

The actual geometry, i.e. scenario (3), will be used in the remainder of the simulations here.

4.3.5 Effect of local friction coefficient

In Van Breemen et al. [12] it was shown that the lateral force strongly depends on the value of the –constant– friction coefficient μ_f via the formation and size of the bow wave in front of the sliding tip. This bow wave causes the tip to be pushed out of the surface and drastically changes the deformation zone in the substrate material. In [12], a value of $\mu_f = 0.2$ gave a best representation of the experimental data. We repeat the procedure for filled PC and perform scratch simulations with different values for μ_f , see Figure 4.7. An increase in local friction results in both a decreased surface penetration

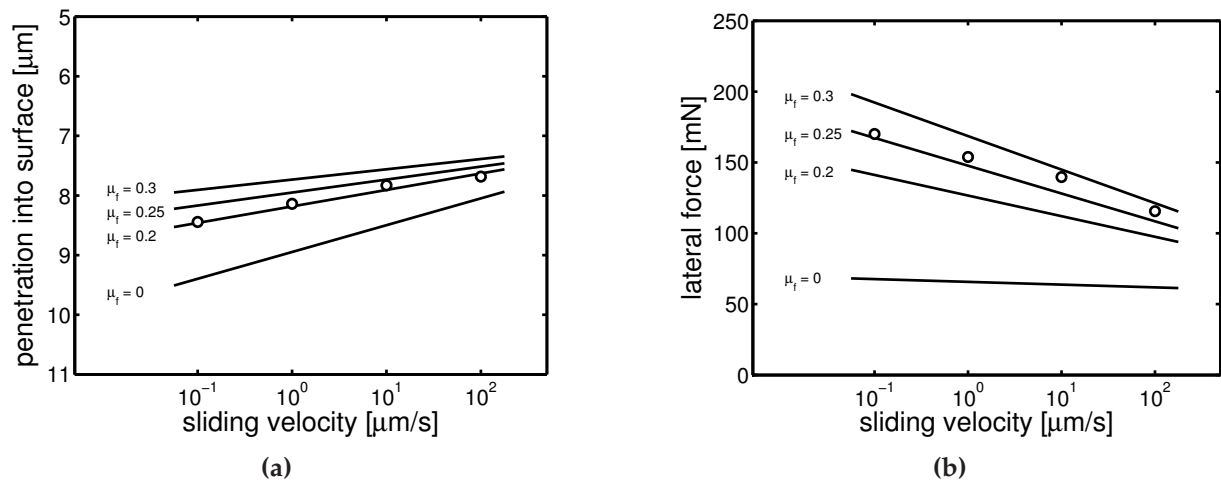


Figure 4.7: The steady-state scratch response of unfilled PC; penetration into the surface (a) and lateral force (b) as a function of sliding velocity; experiments (symbols) versus simulations (lines) performed with different values of μ_f .

and a decrease in velocity-dependency, see Figure 4.7a. For the lateral friction force the opposite is observed: friction between indenter and surface causes the formation of the bow wave, the lateral force required to maintain the velocity increases as does the sensitivity for the sliding velocity, see Figure 4.7b. A value of $\mu_f = 0.25$ is found to represent the data adequately. This is slightly higher than the value of $\mu_f = 0.2$ reported by Van Breemen et al. [12], which is explained by a difference in surface roughness of the tips used.

4.3.6 Comparing experiments with simulations

With the value of μ_f established, scratch simulations are performed using the material parameters describing the particle-filled PC samples. Without any adjustments in ma-

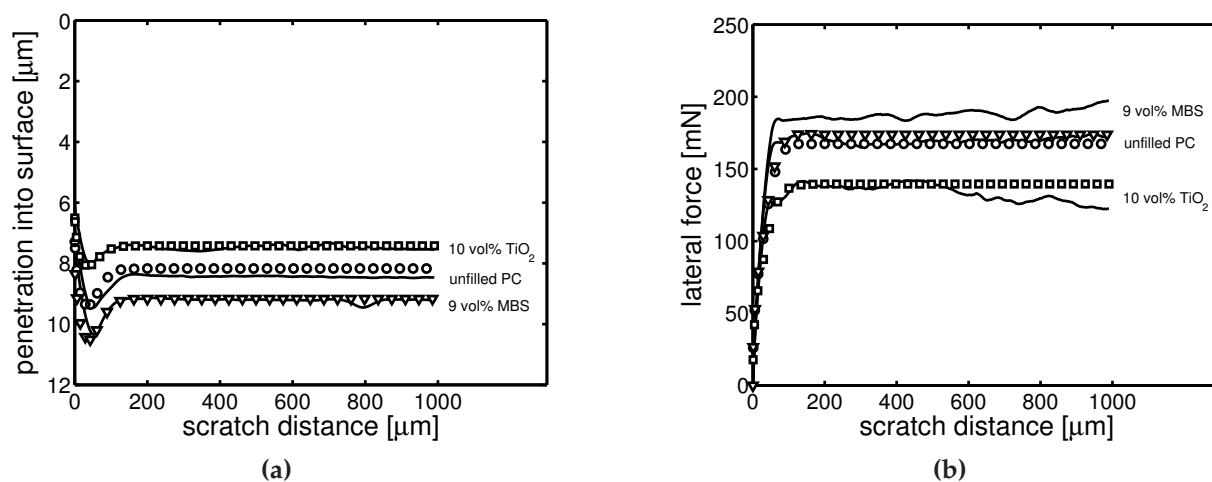


Figure 4.8: Penetration into the surface (a) and lateral friction force (b) as a function of scratch distance for unfilled PC, and PC filled with TiO_2 - or MBS-particles. Scratch velocity is $0.1 \mu\text{m/s}$ and applied normal force is 300 mN . Solid lines are experiments and symbols model predictions with $\mu = 0.25$.

terial parameters, as used in Figure 4.4a to cover the intrinsic behavior of the unfilled system and the homogenized response of the filled PC systems, particularly the thermodynamic state (S_a), and without changing the local friction coefficient ($\mu_f = 0.25$), the simulations predict the penetration into surface gratifyingly well, as shown in Figure 4.8a for $0.1 \mu\text{m/s}$ sliding velocity. The initial penetration depth during indentation, the indenter-tip sink-in at the onset of sliding, and the indenter-tip push out towards the steady state situation are all captured quantitatively. Figure 4.8b shows that the lateral friction force is also predicted well although the response for the MBS-filled sample is slightly under-predicted. Considering the relatively large scatter of this sample at this low speed of $0.1 \mu\text{m/s}$ sliding velocity, see Figures 4.2b and 4.9b, the predicted values are still well within bounds. The simulations also successfully predict the scratch response at different sliding velocities: The shift in penetration depth caused by the addition of fillers and by an increase in sliding velocity are captured quantitatively, see Figure 4.9a, as is the decrease in lateral force with increasing sliding speed and with the addition of 10 vol% hard fillers (TiO_2) whereas it is largely unaffected by adding 9 vol% soft fillers (MBS). This conclusively shows that the observed change in scratch response is solely attributed to the fillers' effect on the intrinsic mechanical response.

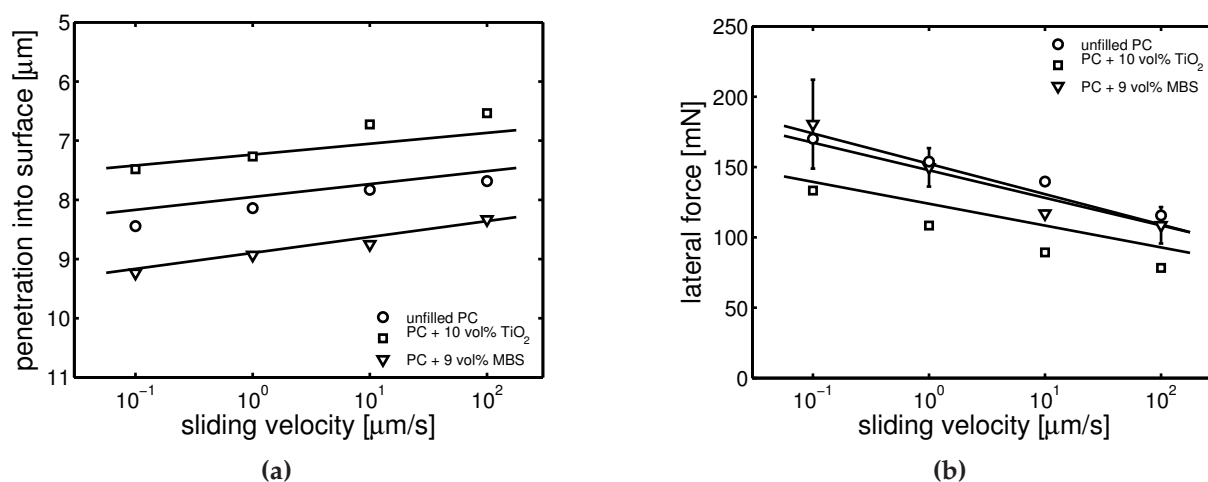


Figure 4.9: Penetration into the surface (a) and lateral friction force (b) as a function of scratch velocity for unfilled PC, and PC filled with TiO₂- or MBS-particles. Applied normal force is 300 mN. Symbols are experiments and lines are model predictions with $\mu_f = 0.25$.

4.3.7 Stress field

The interplay between the intrinsic mechanical response and the local friction results in the formation of a bow wave in front of the indenter tip. The shape of this bow wave, and therefore the contact area with the tip, depends on the total stress field in this region. This is shown in Figure 4.10, where the von Mises stresses (range 25–175 MPa) are shown in the steady state situation at 0.1 μm/s sliding velocity. Clearly, compared to unfilled PC (Figure 4.10a), the stress field is changed by the addition of fillers. With TiO₂-fillers, the yield stress and strain hardening have increased considerably, resulting in more intensified stresses in the contact zone, see Figure 4.10b. The MBS-fillers in contrast, decrease the yield stress but not strain hardening. This results in a decrease in the stresses at the contact zone, see Figure 4.10c. These stress fields, and the resulting stress maxima locally within the underlying 3D-REVs, will later be used in a future study to predict the onset of damage and wear for different microstructures in single asperity sliding friction.

This conclusively shows that the observed change in scratch response is mostly attributed to the fillers' effect on the macroscopic mechanical response. The material composition is likely to influence the adhesive interaction with the diamond tip as well, reflected in μ_f , but this effect seems marginal compared to the fillers' changing the constitutive behavior, and it will therefore lead to values close to $\mu_f = 0.25$.

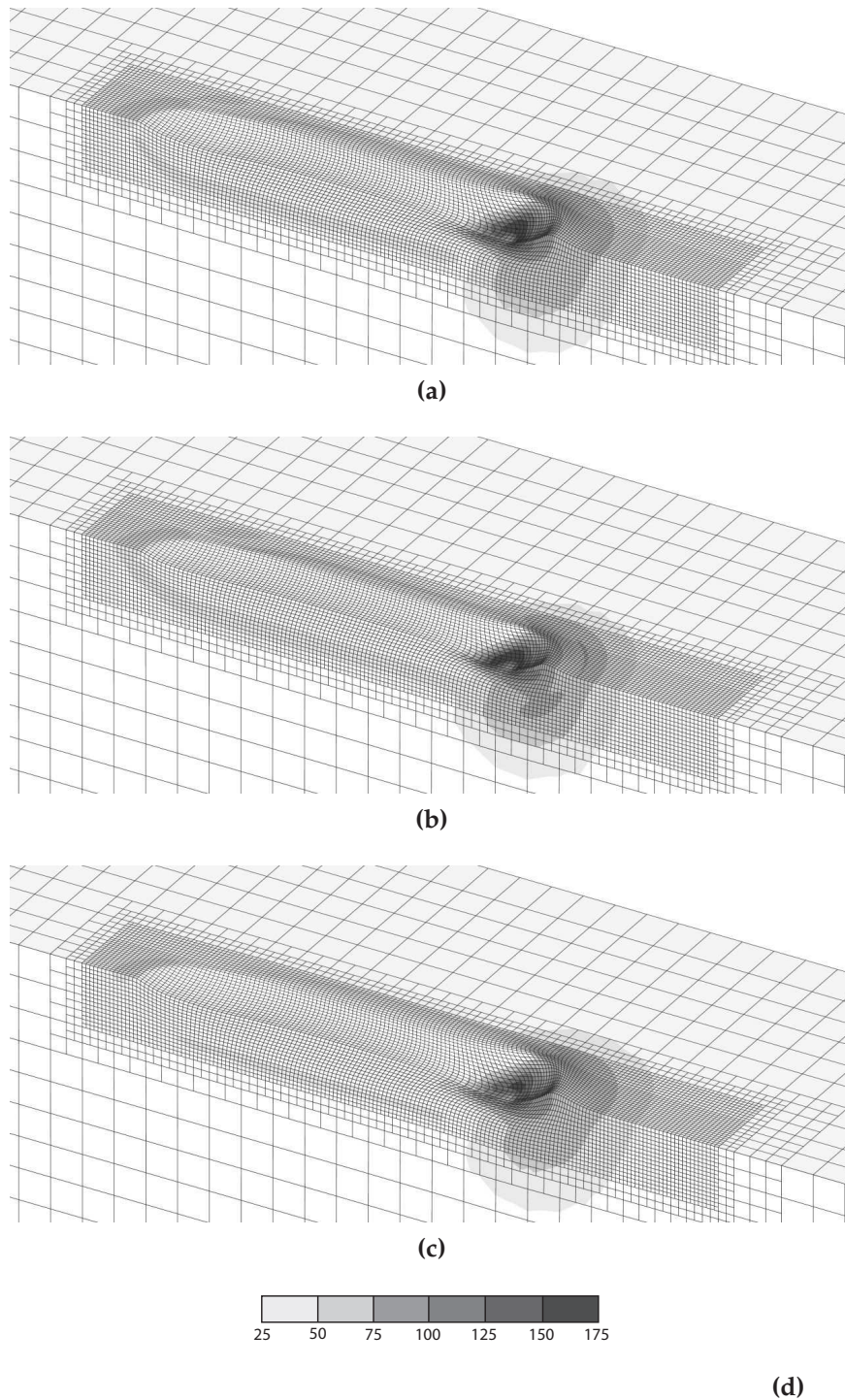


Figure 4.10: The von Mises stresses (25–175 MPa range) during steady-state scratching at $0.1 \mu\text{m/s}$ for (a) unfilled PC, and PC filled with (b) 10 vol% TiO_2 , and (c) 9 vol% MBS. For clarity, the indenter tip is made invisible. (d) Grayscale bar with stress-values in MPa.

4.4 Conclusions

The hybrid experimental-numerical approach is successfully used to quantify the frictional response of well characterized model systems consisting of soft and hard particle-filled PC. Finite-element simulations of the single asperity scratch test were performed using homogenized material parameters obtained via 3D-RVE simulations. Fillers change the intrinsic mechanical response, and therefore also the penetration into the surface during scratching. Soft-filler particles increase the scratch depth, hard-filler particles decrease the depth, and therefore enhance scratch resistance. The lateral-force response is a result of the total stress field in front of the indenter tip, including the influence of the bow wave that forms and changes the deformation region. Here, the effect of the addition of hard particles is obvious and in line with the decreased penetration depth, while that of soft fillers is in first instance less evident, since where penetration depths increase, the friction forces do not. This however, is completely captured by the simulations. Comparing modeling results with the experiments, we can conclude that the scratch response is governed by the fillers' changing the intrinsic mechanical response of the polymer used. Fillers do not change the local interactions between indenter tip and the surface.

4.A Material parameters

Table 4.1: *Material parameters for PC, adopted from Van Breemen et al. [44].*

G_r	κ	τ_0	S_a	μ	r_0	r_1	r_2
[MPa]	[MPa]	[MPa]	[-]	[-]	[-]	[-]	[-]
26	3750	0.7	26.5	0.08	0.965	50	-3

Table 4.2: *Reference spectrum for PC [44].*

mode	$\eta_{0,i,ref}$	G_i	λ_i
	[MPa·s]	[MPa]	[s]
1	$2.10 \cdot 10^{11}$	$3.52 \cdot 10^2$	$5.97 \cdot 10^8$
2	$3.48 \cdot 10^9$	$5.55 \cdot 10^1$	$6.27 \cdot 10^7$
3	$2.95 \cdot 10^8$	$4.48 \cdot 10^1$	$6.58 \cdot 10^6$
4	$2.84 \cdot 10^7$	$4.12 \cdot 10^1$	$6.89 \cdot 10^5$
5	$2.54 \cdot 10^6$	$3.50 \cdot 10^1$	$7.26 \cdot 10^4$
6	$2.44 \cdot 10^5$	$3.20 \cdot 10^1$	$7.63 \cdot 10^3$
7	$2.20 \cdot 10^4$	$2.75 \cdot 10^1$	$8.00 \cdot 10^2$
8	$2.04 \cdot 10^3$	$2.43 \cdot 10^1$	$8.40 \cdot 10^1$
9	$1.83 \cdot 10^2$	$2.07 \cdot 10^1$	$8.84 \cdot 10^0$
10	$1.68 \cdot 10^1$	$1.81 \cdot 10^1$	$8.28 \cdot 10^{-1}$
11	$1.51 \cdot 10^0$	$1.54 \cdot 10^1$	$9.81 \cdot 10^{-2}$
12	$1.40 \cdot 10^{-1}$	$1.36 \cdot 10^1$	$1.03 \cdot 10^{-2}$
13	$1.27 \cdot 10^{-2}$	$1.19 \cdot 10^1$	$1.07 \cdot 10^{-3}$
14	$1.10 \cdot 10^{-3}$	$9.80 \cdot 10^0$	$1.12 \cdot 10^{-4}$
15	$1.23 \cdot 10^{-4}$	$1.04 \cdot 10^1$	$1.18 \cdot 10^{-5}$
16	$2.62 \cdot 10^{-6}$	$2.11 \cdot 10^0$	$1.24 \cdot 10^{-6}$
17	$2.14 \cdot 10^{-6}$	$1.64 \cdot 10^1$	$1.30 \cdot 10^{-7}$

Table 4.3: *Material parameters for particle-filled PC.*

	G_r	κ	τ_0	S_a	μ	r_0	r_1	r_2
	[MPa]	[MPa]	[MPa]	[-]	[-]	[-]	[-]	[-]
10 vol% TiO ₂	35	3970	0.75	30	0.092	0.980	25	-2.8
9 vol% MBS	26	4212	0.62	26	0.068	0.965	15	-2.6

Table 4.4: Reference spectrum for PC filled with 10 vol% TiO₂ particles.

mode	$\eta_{0,i,ref}$ [MPa·s]	G_i [MPa]	λ_i [s]
1	$2.34 \cdot 10^{11}$	$4.23 \cdot 10^2$	$5.53 \cdot 10^8$
2	$1.14 \cdot 10^9$	$5.23 \cdot 10^1$	$2.18 \cdot 10^7$
3	$9.83 \cdot 10^7$	$1.77 \cdot 10^1$	$5.55 \cdot 10^6$
4	$7.41 \cdot 10^7$	$3.61 \cdot 10^1$	$2.05 \cdot 10^6$
5	$1.04 \cdot 10^7$	$3.43 \cdot 10^1$	$3.03 \cdot 10^5$
6	$1.39 \cdot 10^6$	$2.58 \cdot 10^1$	$5.39 \cdot 10^4$
7	$1.28 \cdot 10^5$	$2.06 \cdot 10^1$	$6.21 \cdot 10^3$
8	$2.12 \cdot 10^4$	$1.24 \cdot 10^1$	$1.71 \cdot 10^3$
9	$5.10 \cdot 10^3$	$1.09 \cdot 10^1$	$4.68 \cdot 10^2$
10	$2.26 \cdot 10^3$	$1.14 \cdot 10^1$	$1.98 \cdot 10^2$
11	$7.67 \cdot 10^2$	$9.23 \cdot 10^0$	$8.31 \cdot 10^1$
12	$4.22 \cdot 10^2$	$1.20 \cdot 10^1$	$3.52 \cdot 10^1$
13	$1.16 \cdot 10^2$	$1.21 \cdot 10^1$	$9.59 \cdot 10^0$
14	$2.01 \cdot 10^1$	$1.81 \cdot 10^1$	$1.11 \cdot 10^0$
15	$1.98 \cdot 10^0$	$1.55 \cdot 10^1$	$1.28 \cdot 10^{-1}$

Table 4.5: Reference spectrum for PC filled with 9 vol% MBS particles.

mode	$\eta_{0,i,ref}$ [MPa·s]	G_i [MPa]	λ_i [s]
1	$1.66 \cdot 10^{11}$	$3.16 \cdot 10^2$	$5.26 \cdot 10^8$
2	$8.02 \cdot 10^8$	$3.29 \cdot 10^1$	$2.44 \cdot 10^7$
3	$1.38 \cdot 10^8$	$2.11 \cdot 10^1$	$6.54 \cdot 10^6$
4	$4.22 \cdot 10^7$	$2.41 \cdot 10^1$	$1.75 \cdot 10^6$
5	$8.45 \cdot 10^6$	$2.26 \cdot 10^1$	$3.74 \cdot 10^5$
6	$1.64 \cdot 10^6$	$2.06 \cdot 10^1$	$7.97 \cdot 10^4$
7	$3.22 \cdot 10^5$	$1.90 \cdot 10^1$	$1.70 \cdot 10^4$
8	$6.32 \cdot 10^4$	$1.74 \cdot 10^1$	$3.63 \cdot 10^3$
9	$1.23 \cdot 10^4$	$1.59 \cdot 10^1$	$7.73 \cdot 10^2$
10	$2.40 \cdot 10^3$	$1.46 \cdot 10^1$	$1.65 \cdot 10^2$
11	$4.64 \cdot 10^2$	$1.32 \cdot 10^1$	$3.51 \cdot 10^1$
12	$9.02 \cdot 10^1$	$1.20 \cdot 10^1$	$7.49 \cdot 10^0$
13	$1.73 \cdot 10^1$	$1.09 \cdot 10^1$	$1.60 \cdot 10^0$
14	$3.38 \cdot 10^0$	$9.93 \cdot 10^0$	$3.41 \cdot 10^{-1}$
15	$6.44 \cdot 10^{-1}$	$8.86 \cdot 10^0$	$7.27 \cdot 10^{-2}$
16	$1.29 \cdot 10^{-1}$	$8.30 \cdot 10^0$	$1.55 \cdot 10^{-2}$
17	$2.41 \cdot 10^{-2}$	$7.30 \cdot 10^0$	$3.30 \cdot 10^{-3}$
18	$4.74 \cdot 10^{-3}$	$6.74 \cdot 10^0$	$7.04 \cdot 10^{-4}$
19	$9.37 \cdot 10^{-4}$	$6.24 \cdot 10^0$	$1.50 \cdot 10^{-4}$
20	$1.81 \cdot 10^{-4}$	$5.64 \cdot 10^0$	$3.20 \cdot 10^{-5}$
21	$2.58 \cdot 10^{-5}$	$3.77 \cdot 10^0$	$6.83 \cdot 10^{-6}$
22	$7.62 \cdot 10^{-6}$	$5.24 \cdot 10^0$	$1.46 \cdot 10^{-6}$
23	$2.30 \cdot 10^{-6}$	$7.40 \cdot 10^0$	$3.10 \cdot 10^{-7}$
24	$1.26 \cdot 10^{-7}$	$1.90 \cdot 10^0$	$6.62 \cdot 10^{-8}$

Sliding friction on particle filled epoxy: Developing a quantitative model for complex coatings

Abstract

Epoxy resins represent an important class of thermosetting polymers that are extensively used in demanding applications like in scratch resistant coatings. Usually fillers, either hard (inorganic) or soft (rubbery), are added. Here we test hard and soft particle-filled epoxy systems in single asperity sliding friction experiments, and analyze the results with the hybrid numerical-experimental approach presented earlier. The focus is on the detailed modeling of the local deformation processes and it is confirmed that a rate-independent friction model proves appropriate to quantitatively model this complex process. The constitutive framework developed for amorphous thermoplastic polymers adequately describes also these thermoset systems. The materials response during scratching is likewise. Hard fillers decrease the penetration of the indenter into the surface, and consequently enhance scratch resistance; they cause the lateral friction force to decrease, since less material flows in front of the indenter tip. Soft fillers increase the penetration into the surface, according to expectations, but surprisingly also decrease the friction force. Simulations do not predict this, and suggest an alternative explanation. Migration of rubber particles during sample preparation to the surface could have occurred. Adding a thin rubbery layer to the surface makes the model quan-

Reproduced from: S. Krop, H.E.H. Meijer, and L.C.A. van Breemen. "Sliding friction on particle filled epoxy: Developing a quantitative model for complex coatings," *Wear*, submitted for publication (2016).

titative, but SEM and TEM pictures of the cross-sections do not confirm this phase separation and instead show the presence of a large number of very small voids. Including these voids in the modeling allows to predict the penetration depth into the surface and lateral force quantitative for all sliding speeds.

5.1 Introduction

Apart from polyesters also epoxy-based resins are commonly used in scratch resistant coatings. Investigating the scratch and wear resistance of materials is challenging because of the complex contact conditions that involve many variables [11, 92–94]. Here we focus on the single-asperity sliding friction test, often referred to as ‘scratch test’, to create well-defined contact situations. Friction is the resistance between surfaces in relative motion. Therefore, a proper description of the real contact area between the two bodies is key. Historically this contact area is approximated by the projected area resulting from either ideal elastic or ideal plastic deformation, or a combination thereof [7, 92, 95, 96], but for visco-elastic materials such as polymers this is a strong assumption.

We employ a hybrid experimental–numerical approach instead and started to analyze the scratch response of a model polymer, polycarbonate (PC) [12]. Subsequently, the scratch response of soft and hard particle-filled PC (Chapter 4) was investigated. The material parameters in the homogenized macroscopic constitutive equation used were computed using Three-Dimensional Representative Volume Elements (3D-RVEs), for details see Chapter 2. The scratch response, including its rate dependence, proved to originate from the materials’ intrinsic mechanical response.

For practical coating applications thermoplastic systems such as (particle-filled) polycarbonate are irrelevant since thermosets dominate. Therefore, in this chapter we extend our modeling of the scratch test to the standard epoxy that was already quantitatively characterized in Chapter 3. In coating applications fillers are incorporated, hard (inorganic) ones as colorants or stiffness and scratch reinforcements; soft ones to improve the inherently low toughness and impact resistance of the epoxies used, and to relieve residual stresses that originate from the curing process and that could cause warpage and early fracture. This study aims to quantitatively relate the intrinsic mechanical properties of particle-filled epoxy systems to their response in sliding friction.

5.2 Experimental

5.2.1 Materials and sample preparation

The epoxy resin used is Epon 828 (Hexion Inc.), a standard diglycidyl ether of bisphenol-A (DGEBA) with an epoxide equivalent weight (EEW) of 185–192 g/eq. The curing agent is Jeffamine D230, a polypropyleneoxide diamine with an average molecular weight of 230 g/mol and an amine hydrogen equivalent weight (AHEW) of 60 g/eq, supplied by Huntsman Performance Products. The soft-particles are polysiloxane core-shell rubber (CSR) particles, supplied by Evonik Hanse GmbH as a masterbatch of particles pre-dispersed at 40 wt% in a standard DGEBA resin (trade name Albidur EP2240-A). The particle size is specified as 0.1–3 μm . The thin shell consists of epoxy-functional molecules grafted on the elastomer core. The density of resin and elastomer fillers is assumed to be equal, which entails that weight- and volume fraction have the same value. Samples are prepared with a filler fraction of 10 vol% elastomer content by diluting the masterbatch with standard DGEBA resin. The EEW of the mixture is calculated and the hardener is added in a stoichiometric amount.

The hard-particle fillers are Ti-Pure R-706, a dry grade titanium dioxide (TiO_2) with an average particle size of 350 nm and a density ρ of 4.0 g/cm³, supplied by DuPont Titanium Technologies. First, resin and hardener are mixed in a stoichiometric ratio. Subsequently, TiO_2 -particles are added in a ratio of 90/10 vol% epoxy/ TiO_2 . To calculate this ratio, a density of 1.16 g/cm³ is assumed for the cured epoxy. The pre-mixed samples are thoroughly stirred and degassed under vacuum. The samples are cured for two hours at 80 °C followed by three hours at 125 °C. After the curing protocol, the oven is switched off and allowed to cool to room temperature. To check the quality of curing, the glass transition temperature (T_g) is determined with differential scanning calorimetry (DSC) experiments (Mettler Toledo DSC823e).

Samples of approximately 15 mg are heated to 150 °C, the subsequent scan is performed at a cooling rate of 10 K/min to 25 °C. The T_g of the unfilled samples is 85 °C, which is consistent with results from Chapter 3. The TiO_2 -fillers have no effect on the curing of the matrix as a value of 85.1 °C is found. For the 10 vol% SR-filled samples the T_g is determined at 83.5 °C. This is only slightly lower compared to the unfilled matrix, so it is concluded that also the effect of adding soft particles on curing is minimal.

The samples for the scratch tests are prepared in silicone-rubber containers (10 mm × 10 mm area). A 2 mm layer is poured in the mold, degassed in vacuum, and cured. The scratch tests are performed on the free surface of these samples. The batches for the compression tests are cured in aluminium cups with a diameter of 45 mm and 30 mm in height, from which cylindrical samples (\varnothing 5 mm × 5 mm) are machined.

5.2.2 Testing

The scratch tests are performed with a Nano Indenter XP (MTS Nano-Instruments, Oak Ridge, Tennessee), extended with the lateral force measurement option. The normal force is load controlled, and it is kept constant during the scratch experiments. After the initial indentation step, a constant sliding velocity is applied, ranging 0.1–100 $\mu\text{m/s}$. The diamond indenter tip used for all scratch experiments is cone-shaped, with dimensions specified as 90° top angle and 50 μm top radius. The indenter setup is mounted on a vibration isolation table. Thermal and acoustic disturbances are prevented by a cabinet that encloses this whole system.

Uniaxial compression tests are performed on a Zwick 1475 tester. Cylindrical samples are compressed between two parallel flat steel plates at a constant true strain rate of 10^{-3} s^{-1} . To prevent bulging due to friction between plates and samples, a thin PTFE film (3M 5480 skived plastic film tape) is applied on both ends of the sample and a lubricant (Griffon PTFE spray TF 089) is used on both contact areas between plates and samples. All experiments are performed at room temperature.

5.2.3 Experimental results

Intrinsic response

Figure 5.1 shows the stress-strain responses of the unfilled epoxy sample and the two particle-filled samples, measured at a constant compressive strain rate of 10^{-3} s^{-1} . Interestingly, the intrinsic mechanical response of these thermosetting polymer systems is almost identical to those of their well-studied amorphous thermoplastic counterparts. We find a non-linear viscoelastic response up to yield, followed by strain softening and subsequent strain hardening. Furthermore, the addition of 10 vol% soft SR fillers results in a substantial decrease in yield stress, i.e. the first maximum upon loading,

while the stress decrease to a local minimum after yield (strain softening) is less pronounced. Adding 10 vol% TiO₂ particles results in a slightly increased yield stress and interestingly, similar to the SR filled sample, a substantially reduced strain softening. Upon further loading, the strain hardening regime is entered. Hard fillers increase the

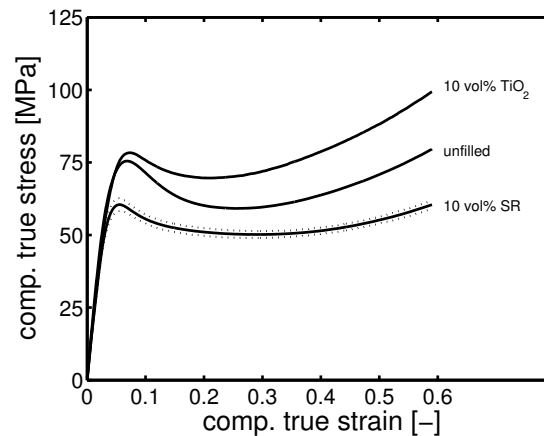


Figure 5.1: Stress-strain response of unfilled and particle-filled epoxy in uniaxial compression at a strain rate of 10^{-3} s^{-1} .

large-strain stress-response, soft fillers decrease the response here. The SR-filled samples showed slightly more scatter in the stress-strain response, compared to the unfilled and TiO₂-filled samples, indicated by the dotted lines in Figure 5.1.

Scratch response

The scratch response at $0.1 \mu\text{m/s}$ is shown in Figure 6.3. The lines representing the measurements are the average of at least 3 consecutive experiments with identical input parameters. In the penetration into the surface (Figure 5.2a), three points of interest are observed: (i) initial indentation, (ii) with the onset of sliding the contact area decreases compared to initial indentation, which, given the constant normal load, results in an increased penetration depth, and finally (iii) a steady state is reached at a lower penetration depth due to the formation of a bow wave in front of the indenter-tip. Qualitatively, the effect of embedding filler particles in the epoxy matrix on the surface penetration is as expected. The hard TiO₂-fillers increase the resistance against deformation, resulting in a decreased penetration depth, whereas this resistance is decreased by the soft SR-particles, resulting in an increase in penetration.

Quantitatively, however, the influence of the soft rubbery particles appears much stronger

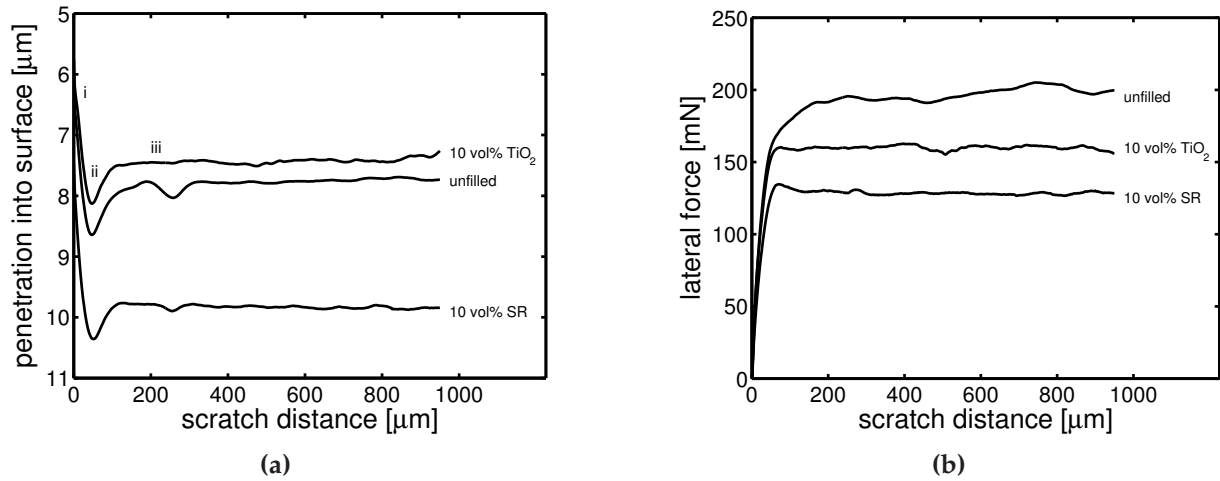


Figure 5.2: Penetration into the surface (a) and lateral friction force (b) as a function of scratch distance for unfilled epoxy, and epoxy filled with TiO₂- or SR-particles. Scratch velocity is 0.1 μm/s and normal force applied is 300 mN.

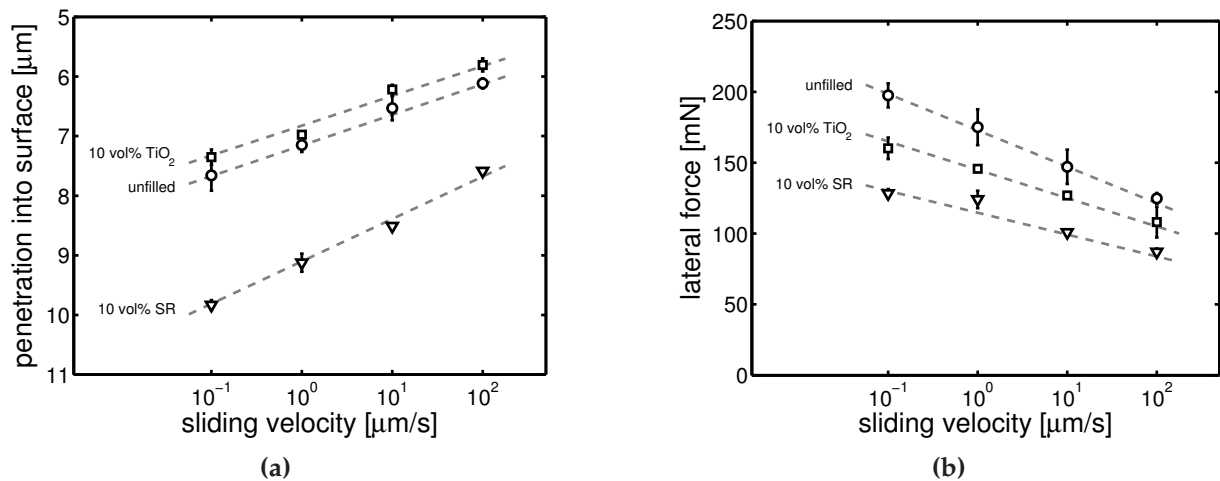


Figure 5.3: The mean of the steady-state penetration into the surface (a) and lateral friction force (b) as a function of scratch velocity for unfilled epoxy, and epoxy filled with TiO₂- or SR-particles.

compared to that of the hard TiO_2 -particles. The effect of these fillers on the lateral-force response, see Figure 5.2b, is really surprising and much less straightforward to interpret. Since with hard fillers the penetration has decreased compared to unfilled epoxy, a smaller contact area between the two bodies results. As a consequence, the lateral force decreases, despite the higher resistance to deformation of this material. This rationale implies that the lateral friction of the SR-filled sample would increase considerably, since this is also the case for the surface penetration. Clearly this is not the case: the lateral force shows an extensive decrease, even compared to the TiO_2 -filled sample.

The steady state response (region iii) shows the same linear dependence on the logarithm of the sliding velocity applied, see Figure 5.3, as observed earlier for unfilled and particle-filled polycarbonate, see Chapter 4. This linear dependence originates from the visco-elastic nature of these polymers, shown by a linear dependence of their yield stress on the logarithm of the strain rate. The addition of filler particles results in a vertical shift of the penetration into the surface only, see Figure 5.3a, the velocity-dependence itself is unaffected. This is also the case for the lateral friction force, see Figure 5.3b.

5.3 Modeling

5.3.1 Intrinsic mechanical response

Constitutive model

The constitutive model employed is the EGP model [43, 44]. It is based on an additive decomposition of the Cauchy stress into a hardening stress σ_r and a driving stress σ_s :

$$\sigma = \sigma_r + \sigma_s. \quad (5.1)$$

Here σ_r accounts for the stress contribution of the network, either entangled or cross-linked, and is modeled with a neo-Hookean spring with modulus G_r . σ_s is attributed to intermolecular interactions. It is additively decomposed into a hydrostatic (volumetric) part (σ_s^h) and a deviatoric part (σ_s^d) that is modeled as a combination of n parallel linked Maxwell elements:

$$\sigma_s = \sigma_s^h + \sum_{i=1}^n \sigma_{s,i}^d = \kappa(J-1)\mathbf{I} + \sum_{i=1}^n G_i \tilde{\mathbf{B}}_{e,i}^d, \quad (5.2)$$

with bulk modulus κ , volume change ratio J , unity tensor \mathbf{I} , shear modulus G , and the elastic part of the isochoric left Cauchy-Green strain tensor $\tilde{\mathbf{B}}_e^d$. The specific modes are

denoted by subscript $i = [1, 2, \dots, n]$. The plastic deformation rate tensors $D_{p,i}$ relate to the deviatoric driving stresses $\sigma_{s,i}^d$ by a non-Newtonian flow rule, that for the isothermal case reads

$$D_{p,i} = \frac{\sigma_{s,i}^d}{2\eta_i(\bar{\tau}, p, S_a)}. \quad (5.3)$$

Here, the viscosities η_i depend on the total equivalent stress $\bar{\tau}$, the hydrostatic pressure p and the thermodynamic state of the material S_a . The viscosities are described by an Eyring flow rule, which has been extended to take pressure dependence and intrinsic strain softening into account:

$$\eta_i = \eta_{0,i,ref} \underbrace{\frac{\bar{\tau}/\tau_0}{\sinh(\bar{\tau}/\tau_0)}}_{(I)} \underbrace{\exp\left(\frac{\mu p}{\tau_0}\right)}_{(II)} \underbrace{\exp(S_a R(\bar{\gamma}_p))}_{(III)}, \quad (5.4)$$

where the initial viscosities $\eta_{0,i,ref}$ define the so-called reference (un-aged) state. Part I represents the stress dependence of the deformation kinetics with the characteristic stress τ_0 ; the pressure dependence, part II, is governed by the parameter μ , and part III captures the dependency of the viscosities on the thermodynamic history via S_a . Strain softening is described by the softening function $R(\bar{\gamma}_p)$, a modified Carreau-Yasuda relation with fitting parameters r_0 , r_1 and r_2 . This model is implemented as a user subroutine in the FEM package MSC.Marc. The procedure to obtain the material parameters

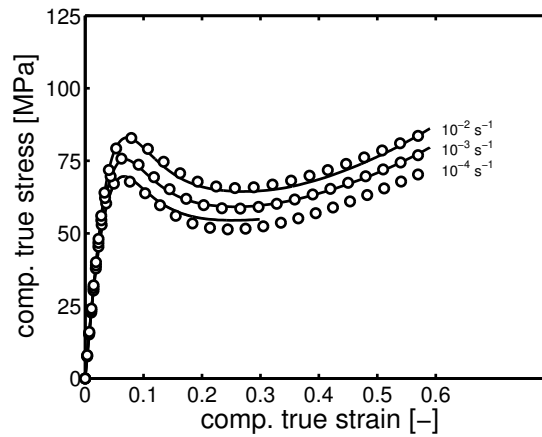


Figure 5.4: Stress-strain response of unfilled epoxy at different strain-rates (solid lines), compared to model predictions using parameter set 1 (open symbols).

for the (unfilled) epoxy matrix is explained in full detail in Chapter 3 and [44], and the parameters are summarized in Table 5.1, denoted as set 1, with the reference spectrum in Table 5.2. Figure 5.4 shows that model predictions using this parameter set are quantitative in describing experimental data at all different strain rates applied.

Homogenization procedure

The homogenization procedure used to obtain the material parameters for the particle-filled epoxy samples is described in full detail in Chapter 4. This method uses a combination of numerical simulations and experimental compression data. Full three dimensional representative volume elements (3D-RVEs), periodic cubic unit cells containing 32 particles, are used as a simplified model for the heterogeneous micro-structure. Particles are assumed spherical, mono-sized, and adhere perfect to the epoxy matrix. A finite element mesh of the 3D-RVE is generated and material properties are assigned. Simulations are performed in both uniaxial tension and compression loadings at different strain rates, to obtain homogenized material parameters. Figure 5.5a shows the

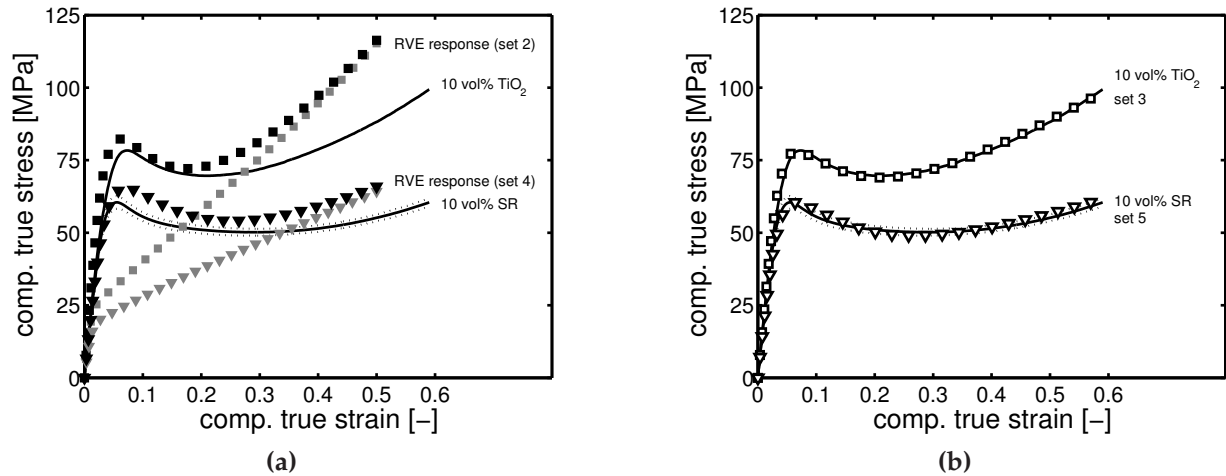


Figure 5.5: (a) Stress-strain response of epoxy filled with either 10 vol% TiO₂ or 10 vol% rubber, at a strain rate of 10^{-3} s^{-1} . Lines are experimental results as in Figure 5.1, compared to predictions from FE-simulation of 3D-RVEs using either $S_a = 17.7$ (closed black symbols) or $S_a = 0$ (closed gray symbols) for the epoxy matrix. (b) Same as (a), but here experiments are compared to model predictions resulting from the homogenization procedure, where parameters are adapted to the large-strain experimental response as described in the text (open symbols)

stress-strain response of these RVEs in compression at 10^{-3} s^{-1} strain rate (closed black symbols), obtained using parameter set 1 for the epoxy matrix, while the TiO₂ particles are modeled as a linear elastic material ($E = 230 \text{ GPa}$ and $\nu = 0.27$) and the rubber particles are modeled neo-Hookean ($G = 5 \text{ MPa}$), compared to experimental results as shown in Figure 5.1.

In the homogenization procedure the stress-strain responses that result from these RVE

simulations is fitted using the Equations (5.1)–(5.4) to provide values for τ_0 , μ and G_r , while the transverse deformation of the RVE provides the Poisson's ratio ν . From the Poisson's ratio, the elastic bulk modulus κ is determined using the elastic conversion formula

$$\kappa = \frac{E}{3(1 - 2\nu)}, \quad (5.5)$$

where the Young's modulus E is obtained from the initial slope of the stress-strain response. The reference state of the filled samples results from simulations with $S_a = 0$ for the epoxy matrix (closed gray symbols in Figure 5.5a). The relaxation spectra are subsequently established using this set of input-parameters, following the procedure described in [44]. This results in parameter set 2 for TiO₂-filled epoxy and set 4 for SR-filled epoxy (see Table 5.1).

Clearly, these parameter sets fail to correctly describe the experimental data (solid lines). The discrepancy is attributed to an accumulation of damage in the systems, which is not taken into account in the simulations, and a difference in aging kinetics of the polymer matrix as a result of matrix-filler interactions, see Chapters 2 and 3. Following the same procedure as used in Chapter 4, the material parameters, specifically G_r and S_a , are adapted such that the experimentally obtained response is captured, see Figure 5.5b (open symbols). This leads to adapted parameter sets for both TiO₂-filled epoxy (set 3) and SR-filled epoxy (set 5). All the material parameters are summarized in Table 5.1. In the remainder, unless specified otherwise, we will use parameter set 1 for unfilled epoxy, set 3 for TiO₂-filled epoxy, and set 5 for SR-filled epoxy. The relaxation spectra of the filled samples are summarized in Tables 5.3 and 5.4.

5.3.2 Scratch simulations

FE-mesh and friction modeling

For the scratch simulations only half of the surface is meshed, since the problem analyzed is symmetric in the direction perpendicular to the sliding direction. The meshed area is $(0.2 \times 0.2 \times 0.8) \text{ mm}^3$, see Figure 5.6, and the dimensions of the mesh are chosen such that the edges have no influence on the stress field. To reduce the total amount of elements only the mesh in the region of interest is refined using the automatic local adaptivity function of Marc, resulting in a total of 73,088 linear brick elements. The symmetry plane is fixed in z-direction and the sides are restrained in z- and y-direction. Scratching occurs from the top and the sliding velocity is prescribed to the meshed block

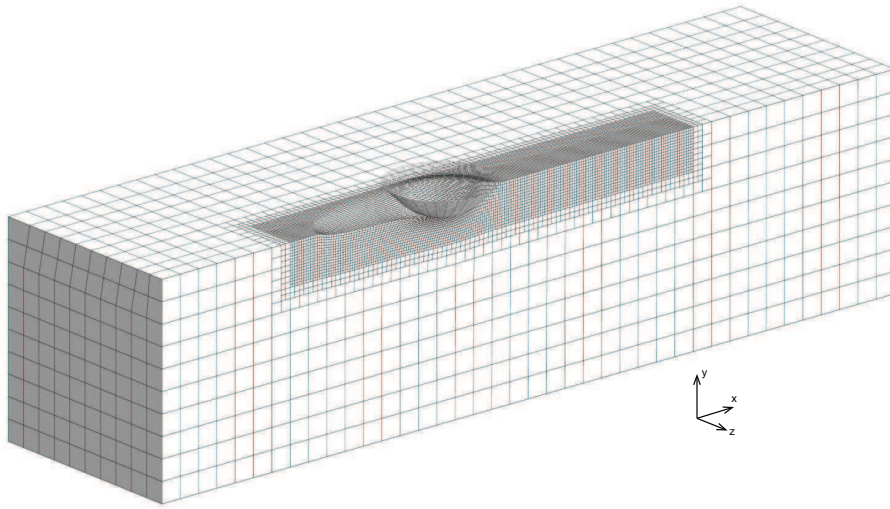


Figure 5.6: *Finite element mesh for the scratch simulations.*

in the negative x-direction. The tip geometry is modeled as a rigid impenetrable surface. A control node on the indenter's surface is used to prescribe the normal force and to retain the indenter in x- and z-direction. Since the scratch response is very sensitive to the exact tip geometry, Chapter 4, an optical profilometer (Sensofar Plu 2300) is used to measure the profile of the indenter tip. This measured profile is used in the simulations.

Local friction is modeled with the most simple model that is implemented in MSC.Marc, Coulomb friction. This model is characterized by a constant, velocity independent, friction coefficient μ_f via:

$$\|\vec{f}_t\| < \mu_f f_n \quad (\text{sticking}) \quad \text{and} \quad \vec{f}_t = -\mu_f f_n \vec{t} \quad (\text{relative sliding}), \quad (5.6)$$

with the tangential (friction) force \vec{f}_t , the normal force f_n , the local friction coefficient μ_f , and the tangential vector \vec{t} in the direction of the relative velocity \vec{v}_r , defined as:

$$\vec{t} = \frac{\vec{v}_r}{\|\vec{v}_r\|}. \quad (5.7)$$

The approach of simplifying the friction model and focusing on introducing more complexity in the local deformation processes was successfully used to capture the scratch response of unfilled and hard- and soft-particle filled polycarbonate, see Van Breemen et al. [12] and Chapter 4.

5.3.3 Comparing experiments with simulations

With the material parameters of the particle-filled samples established (parameter sets 1, 3, and 5), scratch simulations are performed. In Chapter 4, using the same indenter, a value of $\mu_f = 0.25$ was found to best describe the experimental data of unfilled and filled PC, whereas here, a slightly higher value of $\mu_f = 0.27$ is necessary to capture the scratch response of the unfilled epoxy sample. This small difference is explained by differences in the surface chemistry between this epoxy system and PC. At the molecular scale, friction is influenced by factors such as the presence and type of chain ends at the polymer surface, bond-breaking of the polymer chains, and surface and subsurface relaxation modes [111, 112]. Since only one μ_f was capable of capturing the responses of both unfilled and particle-filled PC (Chapter 4), we assume the same here.

Figure 5.7 shows the scratch responses obtained from simulations compared to the experimental results. For both unfilled and TiO₂-filled epoxy the penetration into the surface (Figure 5.7a) and the lateral friction force (Figure 5.7b) are quantitatively described by the simulations for all scratch velocities applied. This is in large contrast with the predictions for the rubber-filled sample. The simulations underestimate both the absolute penetration into the surface and its dependence on the scratch velocity, see Figure 5.7a (gray line). The result is a discrepancy of about 15% at the lowest sliding velocity and, interestingly, the velocity-dependence is predicted parallel to that of unfilled and TiO₂-filled epoxy. With a lower predicted penetration depth, resulting in a smaller indenter–substrate contact area, it is expected that the lateral friction force would be underestimated as well. This is clearly not the case, see the gray line in Figure 5.7b (close to the unfilled line). At the lowest sliding velocity the lateral force is over-predicted with about 50%, and also the decay with increasing velocity is overestimated.

To check whether this discrepancy results from the larger absolute value of the penetration depth itself, i.e. that it results from shortcomings in our approach (e.g. subtle geometry or surface roughness effects on the indenter cone), both the unfilled and the TiO₂-filled samples are tested at a higher normal load of 500 mN. This results in penetration depths that exceed those of SR-filled epoxy at 300 mN, see Figure 5.8a. Comparing these experimental results with simulations shows that the TiO₂-filled sample is captured well over the total velocity range. For the unfilled sample the prediction is correct for the highest sliding velocity, while at lower scratch velocities deviations increase. The surface penetration is under-predicted with 1 μm at the lowest speed. This is still a more accurate prediction, 7% off, compared to that of the rubber-filled sample, 15% off, due to the larger absolute penetration depth. In contrast to the rubber-filled sample at 300 mN,

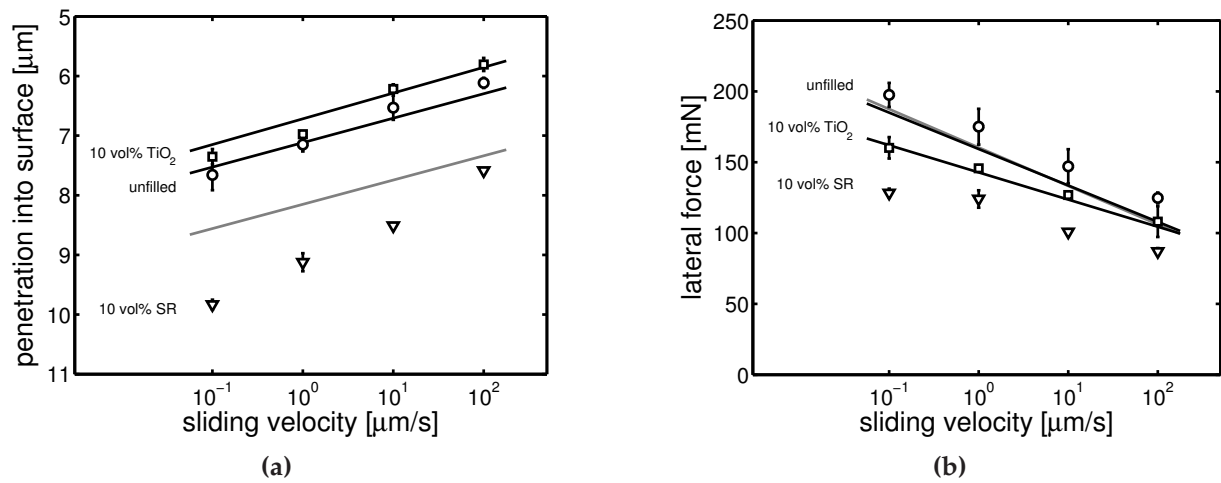


Figure 5.7: Penetration into the surface (a) and lateral friction force (b) as a function of scratch velocity at 300 mN normal load. Symbols are experimental results, as in Figure 5.3, and lines are simulation results for unfilled and TiO_2 -filled epoxy (black), and for SR-filled epoxy (gray). All simulations with $\mu_f = 0.27$.

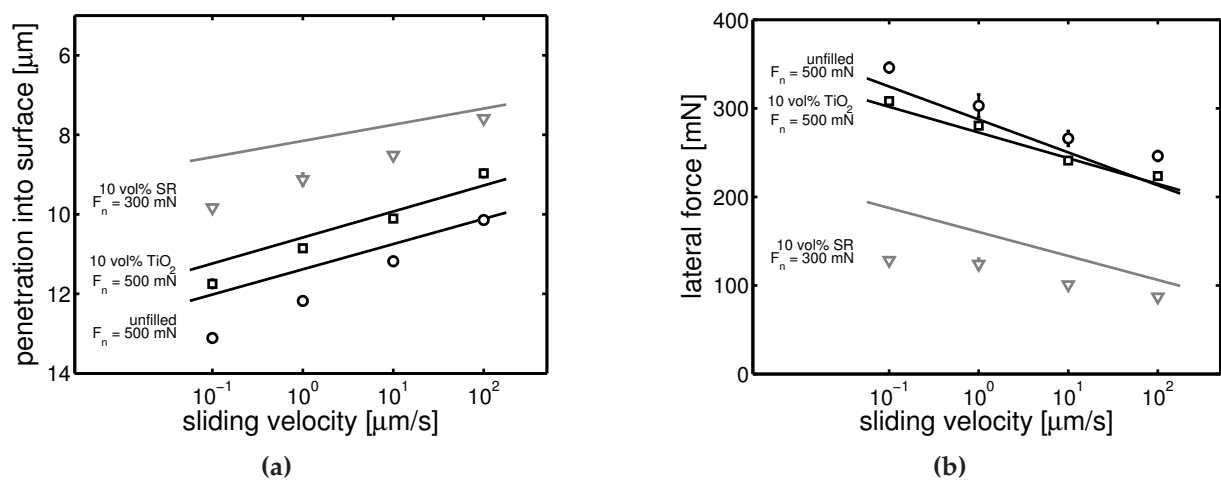


Figure 5.8: Penetration into the surface (a) and lateral friction force (b) as a function of scratch velocity for unfilled and TiO_2 -filled epoxy at 500 mN normal load applied. Experiments (symbols) compared to simulation results using $\mu_f = 0.27$ (solid lines). For comparison, experimental results and numerical predictions of SR-filled epoxy at 300 mN normal load are added in gray.

the lateral friction force at 500 mN normal load is predicted quantitatively for both samples, see Figure 5.8b. Comparing these experiments and simulations confirms that our approach does not fail at deeper penetration depths and, therefore, it does not explain

the discrepancy between simulations and experiments for the rubber-filled sample.

5.3.4 Effect of SR filler-particles

Surface interaction

Since the matrix material already affects the value of μ_f needed to capture the response, $\mu_f = 0.25$ for PC (Chapter 4) and $\mu_f = 0.27$ for this epoxy system, one explanation could be that the SR-fillers directly influences the surface chemistry, resulting in a different interaction with the indenter tip at the molecular scale. To check this, simulations are

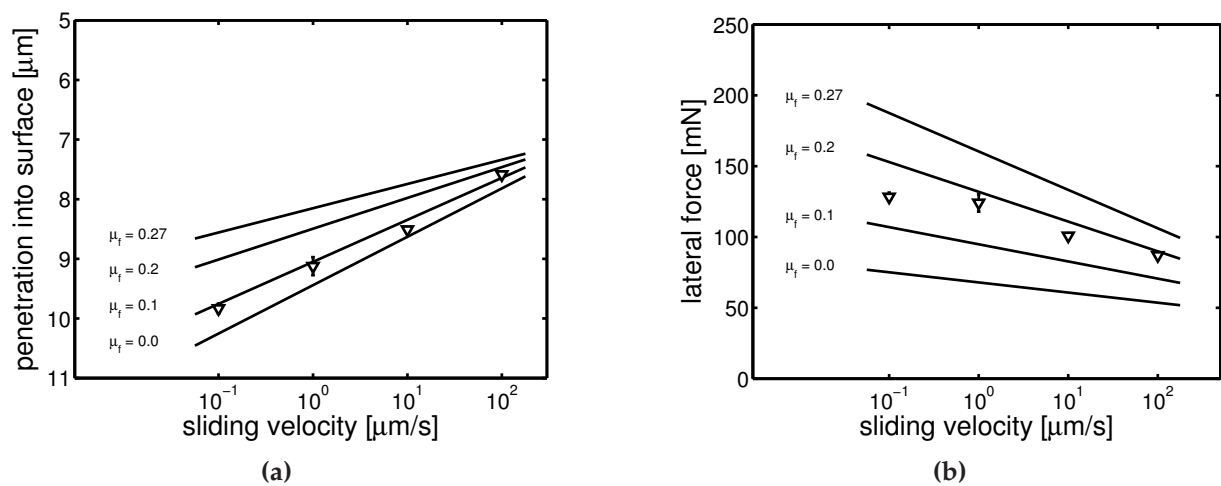


Figure 5.9: Penetration into the surface (a) and lateral friction force (b) as a function of scratch velocity for epoxy filled with SR-particles. Experiments (symbols) compared to simulation results using different values for μ_f (lines).

performed with different values of μ_f , see Figure 5.9. A lower value of μ_f has the effect of a less severe bow wave formation in front of the indenter. Since the experiment is force-controlled, a decrease in contact area and, therefore, an increase in penetration depth results, see Figure 5.9a. Due to the visco-elastic nature of the material, this effect becomes stronger with decreasing sliding velocity. With a single value of $\mu_f = 0.1$ both the absolute penetration depth and its dependence on sliding velocity are captured. With the decreased contact area from lowering μ_f , a decrease of lateral friction force is observed, see Figure 5.9b. Although lower values of μ_f give better predictions of the lateral force, a single value does not cover both force and penetration depth.

Rubber layer

A second explanation for the discrepancy between simulations and experiments could be a difference in composition of the top layer. Although the samples have been thoroughly mixed during sample preparation, the initial stages of the curing process result in a rapid decrease in viscosity of the uncured resin, increasing the mobility of the filler particles. This may cause the formation of clustered regions and/or that rubber fillers are migrating to the top layer to form a region with higher filler content. The relatively larger scatter observed in the stress-strain response, see Figure 5.1, could hint to inhomogeneities in composition. To test the influence of a difference in mechanical properties of the surface region, a single layer of 1 μm thick elements is added to the FE-mesh, see Figure 5.10, and modeled neo-Hookean with a 20 MPa modulus. This thickness is chosen since it is the typical length scale of the filler particles (0.1–3 μm diameter) and the modulus is a compromise between pure rubber properties and epoxy with (extremely) high filler loading. The part underneath this layer is, as before, modeled with parameter set 5.

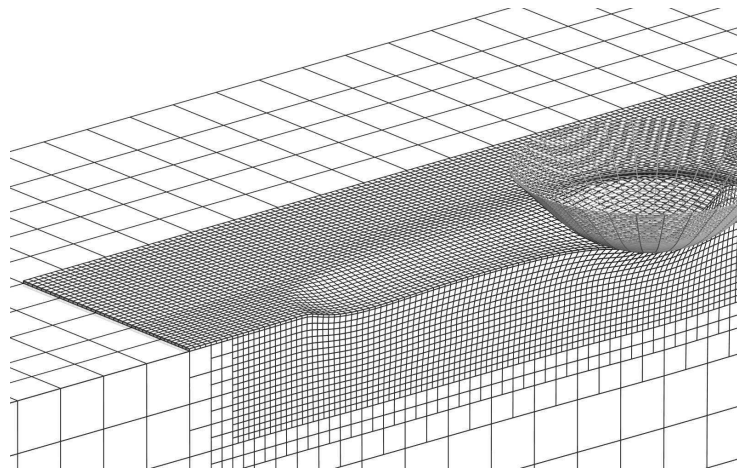


Figure 5.10: Zoom-in of finite element mesh for the scratch simulations with rubber layer on the scratch surface.

Comparing both scenarios, homogeneous composition versus a concentrated rubbery layer with both the same local friction ($\mu_f = 0.27$), the effect of this rubbery layer on the scratch response is considerable, see Figure 5.11. Initial penetration during the indentation step is unaffected, see Figure 5.11a, as is the sink-in when sliding commences, but the steady state penetration has increased about 15%. The absolute difference exceeds the 1 μm from the rubber layer itself. Despite this increase in penetration depth, also the lateral force decreases, by about 40%, see Figure 5.11b. Comparing these sim-

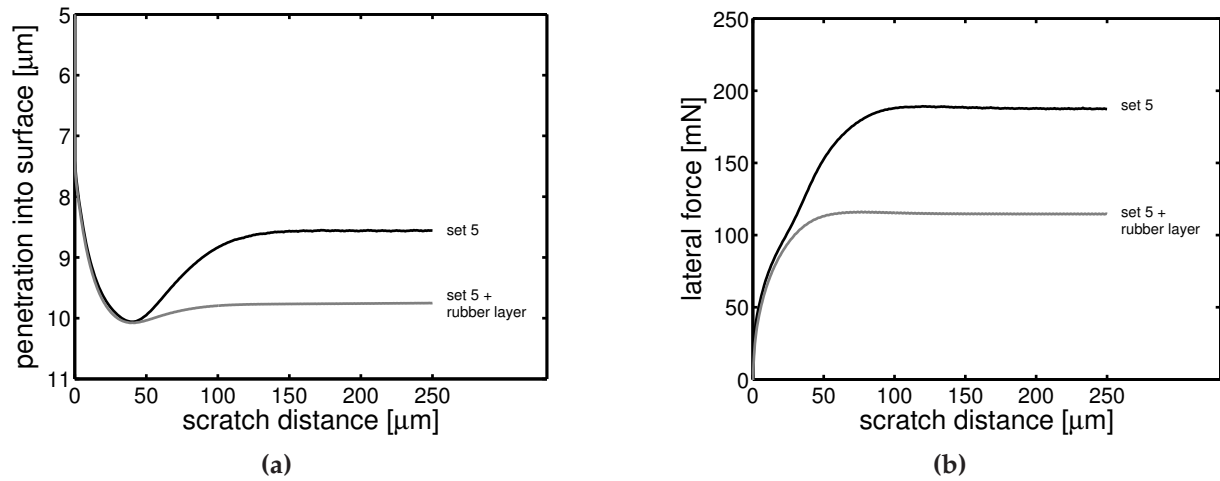


Figure 5.11: The effect of the rubber top-layer on scratch response: penetration into the surface (a) and lateral friction force (b) as a function of scratch distance. Simulation results of 300 mN normal load, 0.1 $\mu\text{m/s}$ sliding velocity, with $\mu_f = 0.27$ local friction coefficient.

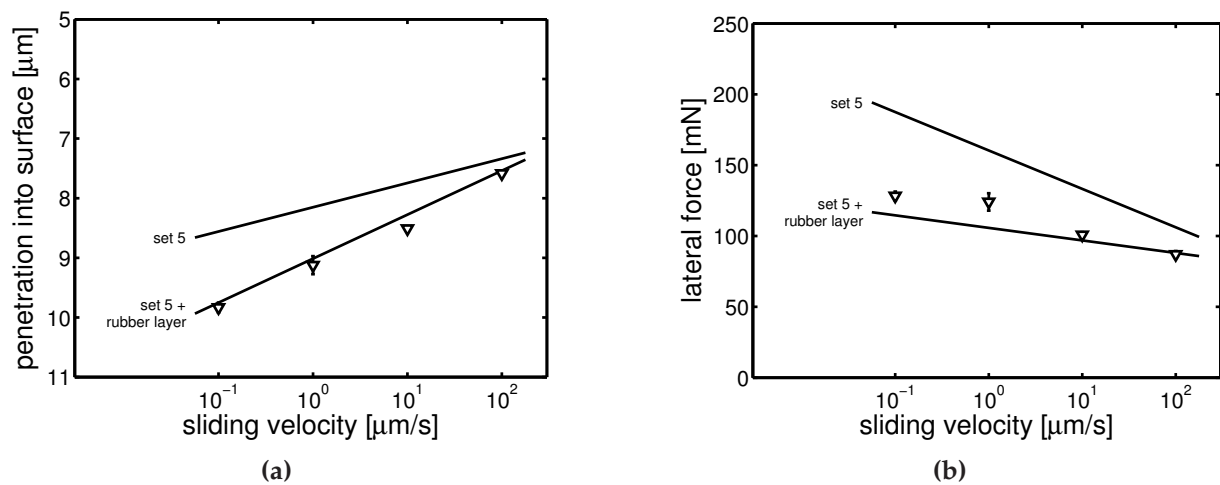


Figure 5.12: Penetration into the surface (a) and lateral friction force (b) as a function of scratch velocity for epoxy filled with SR-particles. Experiments (symbols) compared to simulations (solid lines) using $\mu_f = 0.27$ with a homogeneous scratch domain or with a rubber top-layer.

ulations with experiments yields excellent agreement, see Figure 5.12. The reason for the somewhat surprising effect of such a relatively thin, rubbery layer lies in the shape, but more importantly in the composition, of the bow wave that is formed in front of the indenter. This is illustrated in Figure 5.13, where the cross-section at the symmetry

plane is shown for both scenarios: (i) homogeneous material properties throughout the whole (sub)surface (see Figure 5.13a), and (ii) a rubbery layer on top (see Figure 5.13b). Here the simulations, 300 mN normal load and 0.1 $\mu\text{m}/\text{s}$ sliding velocity, have reached steady-state. The scratch profiles at the symmetry-plane, as indicated by the dashed line for case (i) and the gray line for case (ii), are depicted vertically scaled ($2\times$) in Figure 5.13c. To compare the contributions from the homogeneous filled part only, the profile of this part in case (ii) is added, depicted as a black solid line. The rubbery

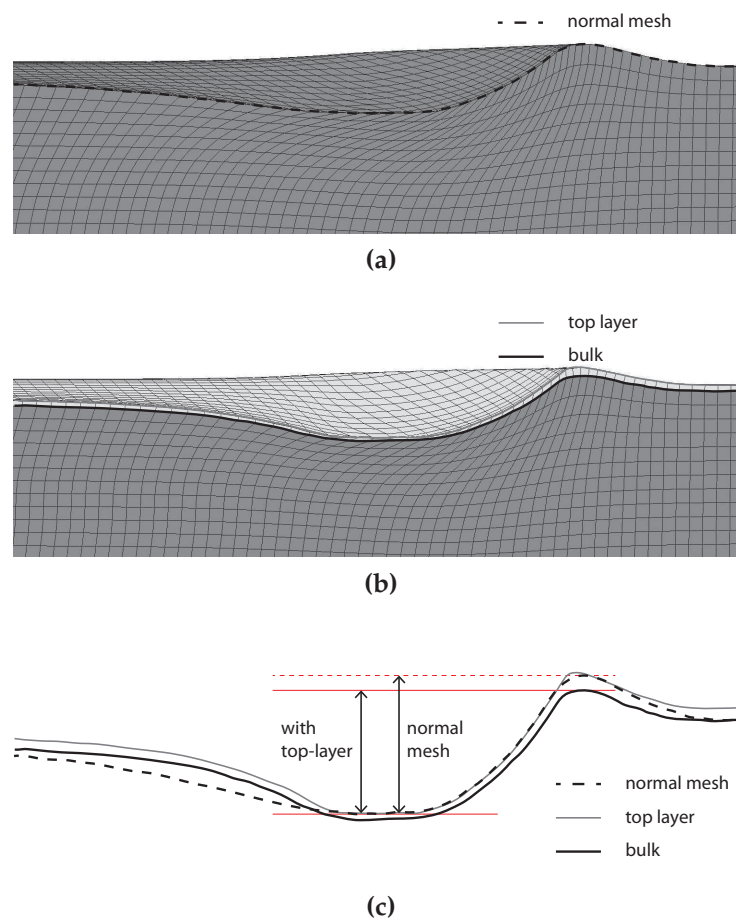


Figure 5.13: Scratch response of rubber-filled epoxy at 0.1 $\mu\text{m}/\text{s}$ sliding velocity and 300 mN normal load, (a) with homogeneous material properties (set 5) and (b) with a rubber layer on the same bulk (set 5); scratch-surface profiles are clarified with lines as indicated in the legend; indenter is not shown for clarity reasons. (c) Vertically scaled ($2\times$) scratch profiles from (a) and (b). Profiles are shifted such that homogeneous bulk, indicated by dark gray in (a) and (b), is at the same level. The projected contact area in horizontal direction between indenter tip and homogeneous bulk is indicated by arrows.

layer only transfers the stresses to the epoxy-rich part underneath, its contribution to the lateral force in the top part of the bow wave is minimal. Therefore, we only consider the projected vertical contact height between the indenter and the homogeneous filled part, as shown in Figure 5.13c. With the top-layer added, clearly a decrease in projected contact height results, even though the total penetration depth had increased. This difference in contact height may seem small, but it results in a quadratically increased projected contact area due to the cone-shape of the indenter. The rubber layer is acting as a stress-reliever for the material underneath, resulting in a smaller volume of epoxy-dominated material to be loaded.

Porous structure

A third, and final, explanation is suggested by inspecting the SEM (Figure 5.14) and TEM (Figure 5.15) images of cross-sections of the scratch sample. No macroscopic phase separation at the surface is observed. Instead, clearly 200–300 nm sized cavities are present everywhere in the material, both in the surface-layer (Figure 5.14a and 5.15a) and throughout the rest of the sample (Figure 5.14b). In the TEM micrographs, the voids are bright white and the rubber particles are visible as dark-gray regions in the epoxy matrix, see Figure 5.15b. The origin of these tiny voids is unknown, but they have a definitive impact on the materials behavior. Analyzing the SEM and TEM images gives a void volume fraction of 7–10% and to estimate their effect on the mechanical response, RVEs are generated with 10 vol% holes. The matrix is given the

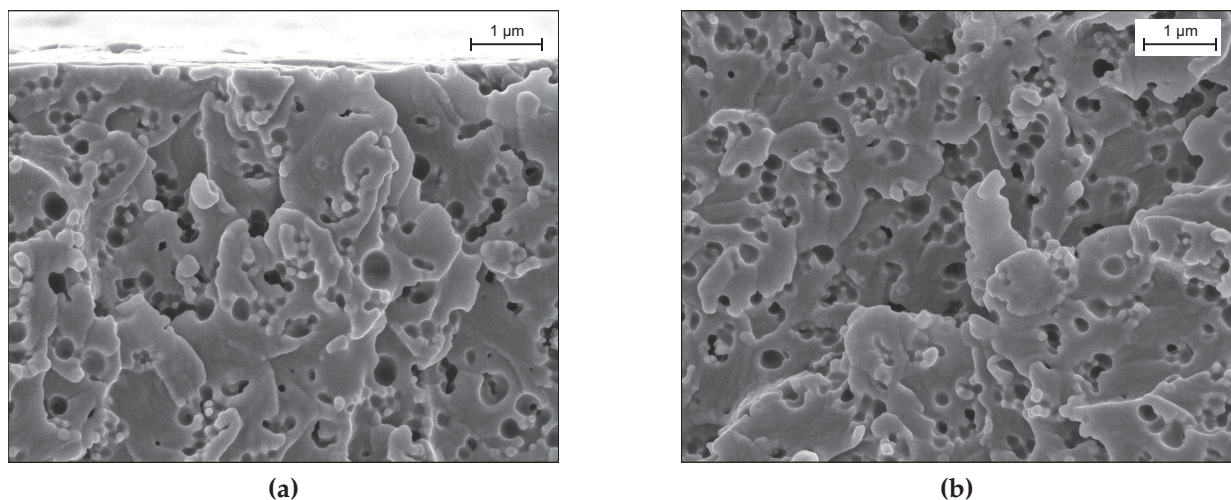


Figure 5.14: SEM pictures of 10 vol% rubber-filled epoxy, of cross-sections at (a) the surface and (b) in the middle of the sample.

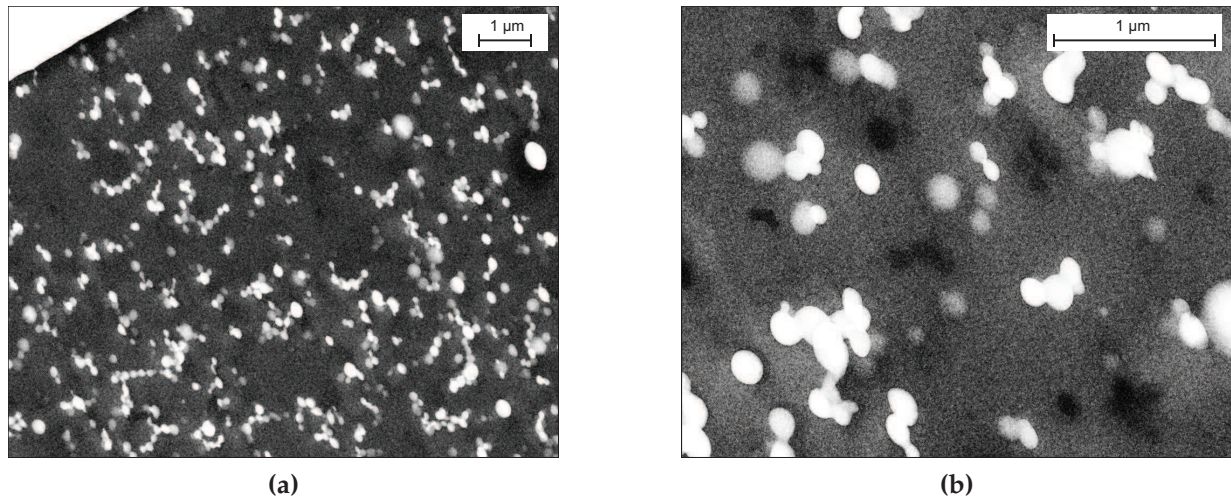


Figure 5.15: (a) TEM micrographs of 10 vol% rubber-filled epoxy. The surface is seen in the top-left corner. The micro-voids appear as bright white holes in the matrix and the SR fillers as dark-gray regions, which are better visible in the enlargement (b).

(ideal) homogenized material properties of 10 vol% rubber-filled epoxy (set 4, see Figure 5.5a). Figure 5.16a shows the response that results from set 4 (closed symbols), and the resulting stress-strain response of the voided RVEs (open symbols) compared with experiments. Evidently, adding 10 vol% voids yields a stress-strain response of the RVE that agrees already well with the experiments.

With voids the compressive stress decreases considerably, compared to the case of only rubber-fillers, set 4 (and 5, see Figure 5.5b), since 10 vol% of the system does not bear load anymore. The material parameters describing the RVE response of the rubber-filled samples in set 5 were adapted to match the experimental yield- and post-yield response, see Figure 5.5b, but this, as we see now, was partly done for the wrong reasons –damage rather than voids. Here we keep using the adapted parameter set 5, but change the compressibility, via the bulk modulus κ , to reflect the presence of the voids and, from the lateral dimension change of the RVE of the voided system, a decrease in the value of κ from 3645 MPa to 2700 MPa is found, Table 5.1 (set 6). This large difference in κ may seem exorbitant at first, but it originates from only a minor difference in Poisson's ratio ν . For set 4 (rubber-filled epoxy), the transverse macroscopic strain observed in the RVE-simulations gave $\nu = 0.41$, whereas for set 6, $\nu = 0.39$ was found. Assuming that the Young's modulus E did not change, which is obviously not the case, Equation 5.5 shows that this small difference in ν already leads to a 20% decrease of κ . Since E has actually decreased as well, an even larger decrease of the bulk modulus

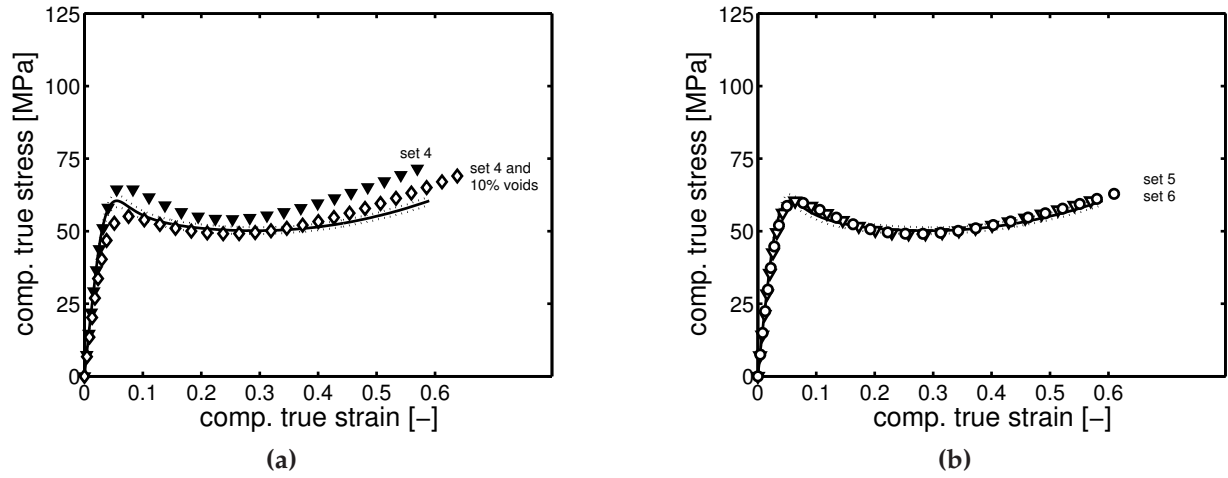


Figure 5.16: Stress-strain response of epoxy filled with 10 vol% rubber at a strain rate of 10^{-3} s^{-1} . Experimental results (mean: solid black lines, scatter: dotted lines), compared to (a) simulations using parameter set 4 (ideal rubber-filled, no voids, closed symbols), and simulations of RVEs with 10 vol% voids (open symbols) where the matrix is described by parameter set 4, and compared to (b) model predictions using to the large strain response of the experiments (G_r) adapted homogenized parameter set 5, and one last identical set with a to voids adapted bulk modulus κ : parameter set 6.

results. Interestingly, the influence of the bulk modulus κ on the response in uni-axial compression/tension is absent since the material is allowed to freely contract/expand in the plane of loading. This is reflected by an identical stress-strain response for set 5 and 6, see Figure 5.16b, despite of the 1 GPa difference in bulk modulus.

Scratch simulations are performed using parameter set 6 and $\mu_f = 0.27$. Changing only the bulk modulus, as compared to set 5, results in a considerable decrease in penetration depth, see Figure 5.17a. In the scratch experiment, κ clearly has a major impact. Below the indenter and directly in front of it, in the bow wave, the material undergoes confined compression, resulting in a high sensitivity to the volumetric contribution. Interestingly, the lateral friction force decreases with the higher penetration depth, see Figure 5.17b, which indicates that the bulk modulus strongly influences the resistance of the material in the bow wave. Compared to the experimentally obtained response, set 6 still underpredicts both penetration depth and lateral friction force. Therefore, we explore the influence of decreasing κ further and perform simulations using $\kappa = 2200 \text{ MPa}$ and $\kappa = 1700 \text{ MPa}$ in combination with parameter set 5, see Figure 5.17. The Poisson's ratios that correspond to these different values of κ are summarized in Table 5.5. Lowering κ proves to sufficiently capture the experimental data. Finally, Figure 5.18 shows

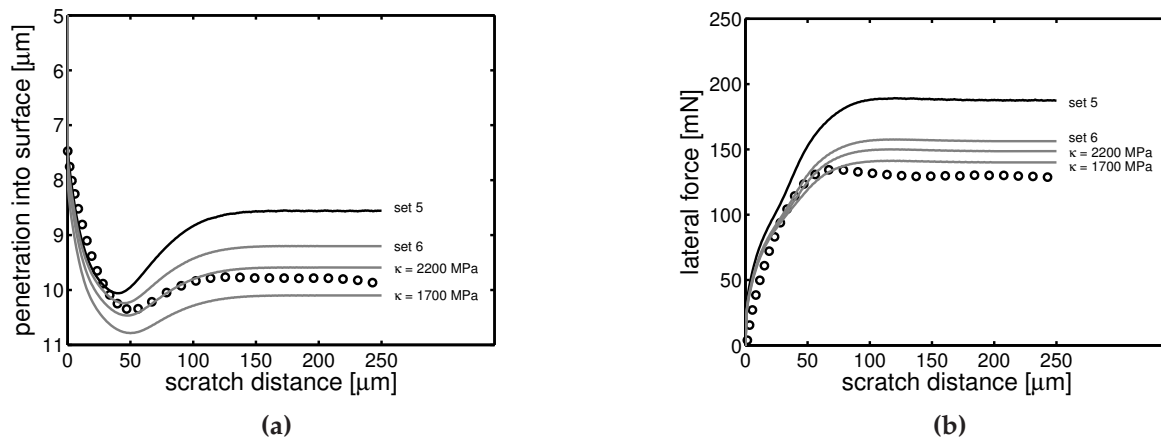


Figure 5.17: The effect of 10 vol% voids in the rubber-filled sample, reflected by lowering the bulk modulus to $\kappa = 2700$ MPa (set 6), and the effect of decreasing κ further: penetration into the surface (a) and lateral friction force (b) as a function of scratch distance. Experiments (symbols) at 300 mN normal load and $0.1 \mu\text{m/s}$ sliding velocity compared to simulation results using different values of κ in parameter set 5.

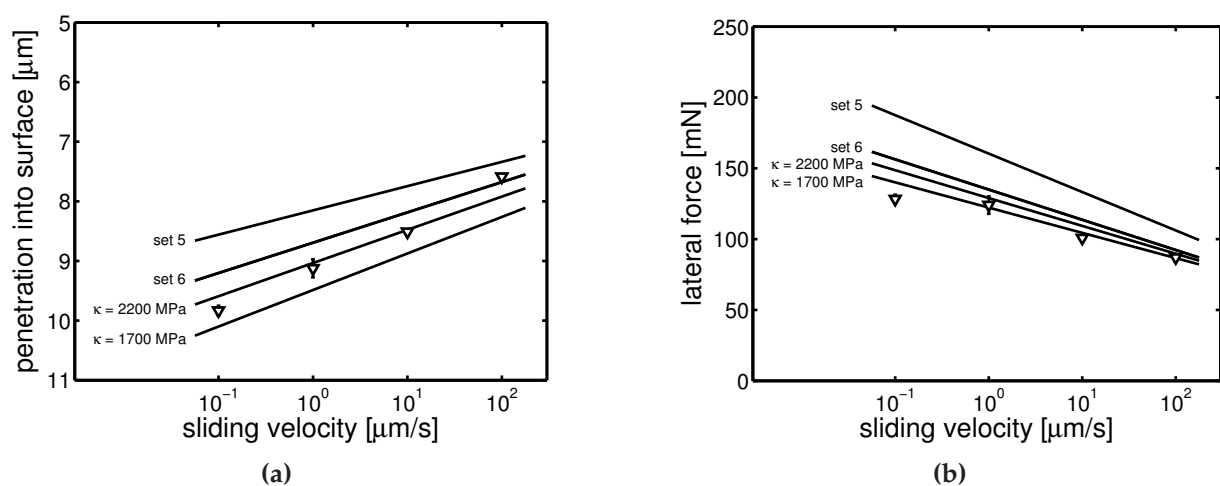


Figure 5.18: Penetration into the surface (a) and lateral friction force (b) as a function of scratch velocity for epoxy filled with SR-particles. Experiments (symbols) compared to simulations using $\mu_f = 0.27$ (solid lines) for two different values of bulk modulus κ .

that the experimental data are quantitatively modelled in the complete sliding velocity range investigated, if a low value for κ is used. This exercise clearly and illustratively demonstrates the importance of employing proper modeling to interpret experimental results of complex processes.

5.4 Conclusions

The hybrid experimental-numerical approach is successfully used to quantify the frictional response of an unfilled standard epoxy system, over a broad range of sliding velocities and at two different normal loads applied. Finite-element simulations of the single asperity scratch test were performed using material parameters obtained from a previous study. A value of $\mu_f = 0.27$ for the local friction coefficient was found to adequately capture the experimental data, which only slightly deviates from the value of 0.25 previously obtained in Chapter 4 for polycarbonate.

Next the same approach is applied to hard (TiO_2) and soft (rubber) particle-filled epoxy samples, using the numerical method described in Chapter 4. Homogenized material parameters are obtained via RVE-simulations and compression tests. Fillers change the intrinsic mechanical response, and therefore also the scratch response. Hard fillers increase the yield stress and decrease the penetration into the surface, i.e. they enhance scratch resistance, causing the lateral friction force to decrease since less material is moved in front of the indenter tip. This is confirmed by the scratch simulations, using $\mu_f = 0.27$, that quantitatively capture the experiments over the whole sliding-velocity range and for two different normal loads applied.

Soft fillers, in contrast, lower the yield stress and greatly increase the penetration into the surface. An unexpected result is that, although a larger volume of material is addressed, the lateral friction is decreased. This implies a change in friction or local deformation. Simulations confirm that lower values of μ_f , ranging 0.1–0.2, give better predictions, but no unique value of μ_f adequately captures both the surface penetration and the lateral friction response. An alternative explanation, inspired by the relatively large scatter observed in the compression response, is that the rubber fillers tend to agglomerate during the preparation process. For the scratch samples this could cause a surface layer with increased rubber content to form. Scratch simulations employing a 1 μm rubber surface layer, and with again $\mu_f = 0.27$, gave excellent results and, while surface penetration increases, the lateral friction force strongly decreases due to a redistribution

of stress, caused by the presence of a rubber layer. However, its existence could not be confirmed by inspecting the cross sections of the samples by SEM and TEM. Instead, serious voiding was found showing in the order of 10% 200–300 nm sized uniformly distributed cavities. Incorporating these voids via a multi-level approach in the modeling proved to result in an interesting macroscopic effect. An increase in penetration depth combined with a decrease in lateral force was predicted over the whole velocity range. Combined with a decreased value of the compressibility κ , it proved quantitative. This exercise witnessed the importance of attempts to interpret experimental results on complex processes with proper modeling.

5.A Material parameters

Table 5.1: *Material parameters for particle-filled epoxy.*

filler	set #	G_r [MPa]	κ [MPa]	τ_0 [MPa]	S_a [-]	μ [-]	r_0 [-]	r_1 [-]	r_2 [-]
unfilled	set 1	35	3200	1.5	17.7	0.166	0.977	15	-3.4
10 vol% TiO ₂	set 2	63	3675	1.49	17.4	0.219	0.98	50	-4.3
	set 3	44	3675	1.49	16.5	0.219	0.98	20	-2.8
10 vol% SR	set 4	33.2	3645	1.26	17.8	0.153	0.98	14	-3.0
	set 5	26	3645	1.26	16.3	0.153	0.98	15	-2.6
	set 6	26	2700	1.26	16.3	0.153	0.98	15	-2.6

Table 5.2: *Reference spectrum for epoxy.*

mode	$\eta_{0,i,ref}$ [MPa·s]	G_i [MPa]	λ_i [s]
1	$4.74 \cdot 10^5$	$4.47 \cdot 10^2$	$1.06 \cdot 10^3$
2	$5.79 \cdot 10^3$	$5.77 \cdot 10^1$	$1.00 \cdot 10^2$
3	$1.50 \cdot 10^3$	$5.41 \cdot 10^1$	$2.77 \cdot 10^1$
4	$3.39 \cdot 10^2$	$4.05 \cdot 10^1$	$8.37 \cdot 10^0$
5	$8.41 \cdot 10^1$	$3.33 \cdot 10^1$	$2.53 \cdot 10^0$
6	$2.10 \cdot 10^1$	$2.75 \cdot 10^1$	$7.64 \cdot 10^{-1}$
7	$4.21 \cdot 10^0$	$1.82 \cdot 10^1$	$2.31 \cdot 10^{-1}$
8	$1.21 \cdot 10^0$	$1.74 \cdot 10^1$	$6.97 \cdot 10^{-2}$
9	$2.10 \cdot 10^{-1}$	$1.00 \cdot 10^1$	$2.10 \cdot 10^{-2}$
10	$8.01 \cdot 10^{-2}$	$1.26 \cdot 10^1$	$6.35 \cdot 10^{-3}$
11	$1.69 \cdot 10^{-2}$	$8.79 \cdot 10^0$	$1.92 \cdot 10^{-3}$
12	$7.71 \cdot 10^{-3}$	$1.33 \cdot 10^1$	$5.80 \cdot 10^{-4}$
13	$1.46 \cdot 10^{-3}$	$8.35 \cdot 10^0$	$1.75 \cdot 10^{-4}$
14	$7.18 \cdot 10^{-4}$	$1.36 \cdot 10^1$	$5.29 \cdot 10^{-5}$
15	$1.44 \cdot 10^{-4}$	$9.01 \cdot 10^0$	$1.60 \cdot 10^{-5}$

Table 5.3: Reference spectrum for epoxy filled with 10 vol% TiO₂ particles.

mode	$\eta_{0,i,ref}$ [MPa·s]	G_i [MPa]	λ_i [s]
1	$7.61 \cdot 10^5$	$5.02 \cdot 10^2$	$1.52 \cdot 10^3$
2	$5.15 \cdot 10^3$	$7.31 \cdot 10^1$	$7.05 \cdot 10^1$
3	$5.15 \cdot 10^2$	$2.95 \cdot 10^1$	$1.75 \cdot 10^1$
4	$2.35 \cdot 10^2$	$3.85 \cdot 10^1$	$6.10 \cdot 10^0$
5	$2.50 \cdot 10^1$	$3.05 \cdot 10^1$	$8.20 \cdot 10^{-1}$
6	$3.51 \cdot 10^0$	$2.25 \cdot 10^1$	$1.56 \cdot 10^{-1}$
7	$4.47 \cdot 10^{-1}$	$1.85 \cdot 10^1$	$2.42 \cdot 10^{-2}$
8	$3.18 \cdot 10^{-2}$	$1.28 \cdot 10^1$	$2.48 \cdot 10^{-3}$

Table 5.4: Reference spectrum for epoxy filled with 10 vol% SR particles.

mode	$\eta_{0,i,ref}$ [MPa·s]	G_i [MPa]	λ_i [s]
1	$6.12 \cdot 10^5$	$4.02 \cdot 10^2$	$1.52 \cdot 10^3$
2	$4.14 \cdot 10^3$	$5.96 \cdot 10^1$	$6.95 \cdot 10^1$
3	$4.04 \cdot 10^2$	$2.24 \cdot 10^1$	$1.80 \cdot 10^1$
4	$2.13 \cdot 10^2$	$3.42 \cdot 10^1$	$6.23 \cdot 10^0$
5	$1.01 \cdot 10^1$	$4.38 \cdot 10^0$	$2.31 \cdot 10^0$
6	$2.59 \cdot 10^1$	$2.81 \cdot 10^1$	$9.22 \cdot 10^{-1}$
7	$2.81 \cdot 10^0$	$1.68 \cdot 10^1$	$1.67 \cdot 10^{-1}$
8	$5.18 \cdot 10^{-1}$	$5.25 \cdot 10^0$	$9.87 \cdot 10^{-2}$
9	$3.48 \cdot 10^{-1}$	$1.09 \cdot 10^1$	$3.19 \cdot 10^{-2}$
10	$1.04 \cdot 10^{-1}$	$7.65 \cdot 10^0$	$1.36 \cdot 10^{-2}$
11	$3.82 \cdot 10^{-2}$	$7.90 \cdot 10^0$	$4.84 \cdot 10^{-3}$
12	$1.54 \cdot 10^{-2}$	$7.85 \cdot 10^0$	$1.96 \cdot 10^{-3}$
13	$5.20 \cdot 10^{-3}$	$8.16 \cdot 10^0$	$6.37 \cdot 10^{-4}$
14	$1.48 \cdot 10^{-3}$	$6.71 \cdot 10^0$	$2.21 \cdot 10^{-4}$
15	$5.04 \cdot 10^{-4}$	$7.06 \cdot 10^0$	$7.14 \cdot 10^{-5}$
16	$1.20 \cdot 10^{-4}$	$5.97 \cdot 10^0$	$2.01 \cdot 10^{-5}$
17	$2.58 \cdot 10^{-5}$	$6.59 \cdot 10^0$	$3.92 \cdot 10^{-6}$

Table 5.5: Poisson's ratios ν corresponding to the bulk moduli κ used in Figures 5.16–5.18.

		set 4–5	set 6		
κ	[MPa]	3645	2700	2200	1700
ν	[–]	0.41	0.39	0.37	0.33

Micro-structural design for optimum scratch-resistant, wear-resistant, and low-friction coatings

6.1 Introduction

In Chapters 4 and 5, References [113] and [114], a hybrid experimental-numerical approach was presented to characterize the scratch response of hard- or soft particle-filled polymer systems, with either polycarbonate (PC) or an epoxy as matrix material. The homogenized material parameters used in the scratch simulations were obtained from the simulated response of three dimensional Representative Volume Elements (3D-RVEs), as presented in Chapters 2 and 3, References [115] and [116], applied to the same particle-filled systems. Typically, the scratch response is characterized by the penetration depth, a measure for the materials' scratch resistance, and the lateral friction force. The homogenized material parameters that are necessary to capture the scratch response in simulations might also be obtained directly from the experimental stress-strain response. The relation between the influence of filler-particles on the stress-strain response and, as a consequence, on the scratch resistance and the lateral resistance will be discussed in Section 6.2. Ultimately, friction leads to wear as critical events at the asperity-substrate interface lead to the formation of cracks. For particle-filled systems these critical events arise at the inter-particle scale and/or at the particle-matrix interface. Therefore, understanding wear in these systems demands not only the macroscopic response but, more importantly, information about the distribution of

stresses and strains at the local scale. Now the full potential of our approach is revealed, since the 3D-RVEs also provide this information. Section 6.3 presents the synergy of the scratch- and RVE-simulations. Finally in Section 6.4, based on detailed analyses of variations in the microstructure using 2D-RVEs, guidelines are derived to arrive at microstructures optimized with respect to improved wear resistance without sacrificing scratch resistance and low friction. The chapter ends with some conclusions and recommendations in Section 6.5.

6.2 Scratch-resistant and low-friction coatings

In Chapters 4 and 5 it was shown that the addition of hard filler particles leads to improved scratch resistance, i.e. the penetration into the surface is decreased, whereas soft fillers deteriorate it. Figure 6.1a summarizes the experimental compression data of hard and soft particle-filled polycarbonate (Chapter 2) and epoxy (Chapters 3 and 5) at 10^{-3} s^{-1} strain-rate. Clearly, these different systems mainly show a vertical shift in the yield and post-yield response.

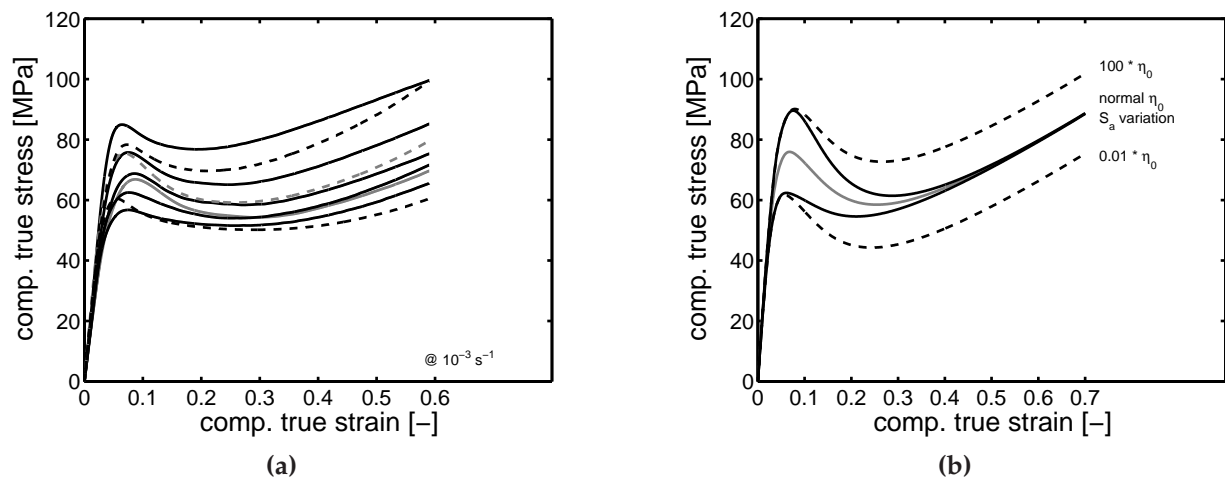


Figure 6.1: (a) Experimental stress-strain response of particle-filled (black) and unfilled (grey) polycarbonate (solid lines) and epoxy (dashed lines) in uniaxial compression at 10^{-3} s^{-1} strain rate. (b) EGP-model stress-strain response of epoxy (grey solid line), with different S_a values (black solid lines) or viscosities (dashed lines).

6.2.1 Yield or post-yield

To investigate which is the most dominant contribution, the yield stress itself or the total post-yield regime stress, we consider the intrinsic mechanical response of unfilled epoxy using the material parameters from Chapter 5, with $S_a = 17.7$, see Figure 6.1b. The flow stress in the EGP model is defined as:

$$\sigma_{s,i}^d = 2\eta_i(\bar{\tau}, p, S_a)D_{p,i}, \quad (6.1)$$

where the viscosity is defined by an Eyring type flow rule:

$$\eta_i = \eta_{0,i,ref} \underbrace{\frac{\bar{\tau}/\tau_0}{\sinh(\bar{\tau}/\tau_0)}}_{(I)} \underbrace{\exp\left(\frac{\mu p}{\tau_0}\right)}_{(II)} \underbrace{\exp(S_a R(\bar{\gamma}_p))}_{(III)}. \quad (6.2)$$

We consider two situations: (case 1) a $100\times$ increase or decrease in initial viscosity $\eta_{0,i,ref}$, leading to an order 2 shift of the total relaxation spectrum, and (case 2) a $\ln(100)$ or $\ln(1/100)$ change in S_a , leading to values of 22.3 and 13.1, respectively. Both cases lead to the same yield stresses, but the post-yield response is completely different, see Figure 6.1b: case 1 leads to a shift in stress for the complete post-yield regime, whereas case 2 leaves the strain-hardening regime unaffected.

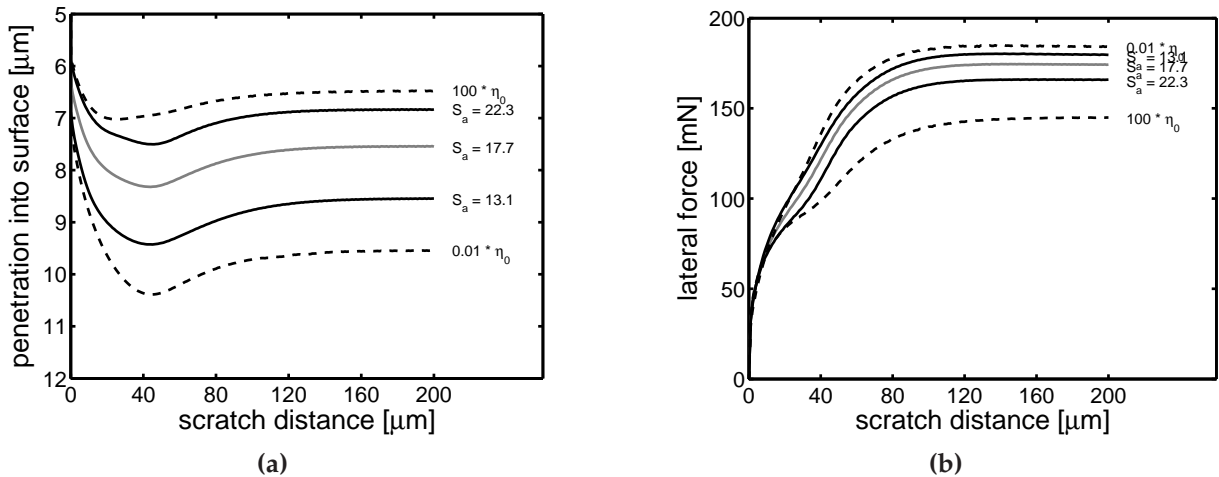


Figure 6.2: Predictions from scratch simulations using model parameters for epoxy, with different values for S_a or with shifted viscosity (influence on stress-strain response is shown in Figure 6.1b). (a) Penetration into the surface and (b) lateral friction force as a function of scratch distance.

Scratch simulations are performed with the original parameter sets, combined with the extra parameters for case (1) and (2). The results of these five simulations, with normal load set to 300 mN, 0.1 $\mu\text{m/s}$ sliding velocity, and a local friction coefficient of $\mu_f = 0.27$, are shown in Figure 6.2. Qualitatively, either increasing the yield stress expressed in η_i through $\eta_{0,i,ref}$ (case 1) or through S_a (case 2) leads to the same effect: a decrease in the penetration into the surface and, as a result of the lower contact area, a decreased lateral friction force. Quantitatively, however, the influence of changing the total post-yield response is stronger. Decreasing η_i has the opposite effect and, also here, the influence from changing the whole intrinsic post-yield response is the strongest.

6.2.2 Scratch resistance and yield stress

How the yield stress correlates with the scratch response experimentally is shown in Figures 6.3a–6.3b, where data of scratch experiments on hard and soft particle-filled, and unfilled, polycarbonate and epoxy at 1 $\mu\text{m/s}$ sliding velocity and different normal loads is shown. For each material the yield stress at 10^{-3} s^{-1} is known, see Figure 6.1a. Figure 6.3c shows the steady-state surface penetration from Figure 6.3a as a function of the yield stress. Clearly, a strong correlation exists between a material's yield stress and its scratch resistance. The steady-state lateral friction force is shown in Figure 6.3d; here the correlation is less evident. Next, simulations are performed. Differentiation in material properties via the yield stress is obtained by shifting the relaxation spectrum 2 orders in magnitude, either up or down, (case 1) in Figure 6.1b, since this describes the experimental differences between the materials' responses the best, see Figure 6.1a. Three different normal loads are considered, 300–500–700 mN. The simulations confirm that the scratch resistance increases with yield stress, see Figure 6.3e. Furthermore, as shown in Figure 6.3f, it appears that the friction force is indeed less sensitive to the yield stress.

Until now we considered penetration into the surface during scratching only. However, for practical realistic scratch resistance, the residual scratch depth, obtained after elastic recovery, is more relevant. The simulations also provide the residual scratch depth and they are included with the grey dashed lines in Figure 6.3e for 300 and 700 mN normal load. It appears that indeed only a small part of the penetration into the surface is plastic yielding (irreversible deformation), most is elastic. The simulations predict a decrease in relative recovery with increasing yield stress, but this unexpected and probably erroneous result could be attributed to deficiencies in the simple version of the EGP model used, where reversing deformations leads to errors. Solutions to this problem, the so-called Bauschinger effect, are known and have been found by introducing a

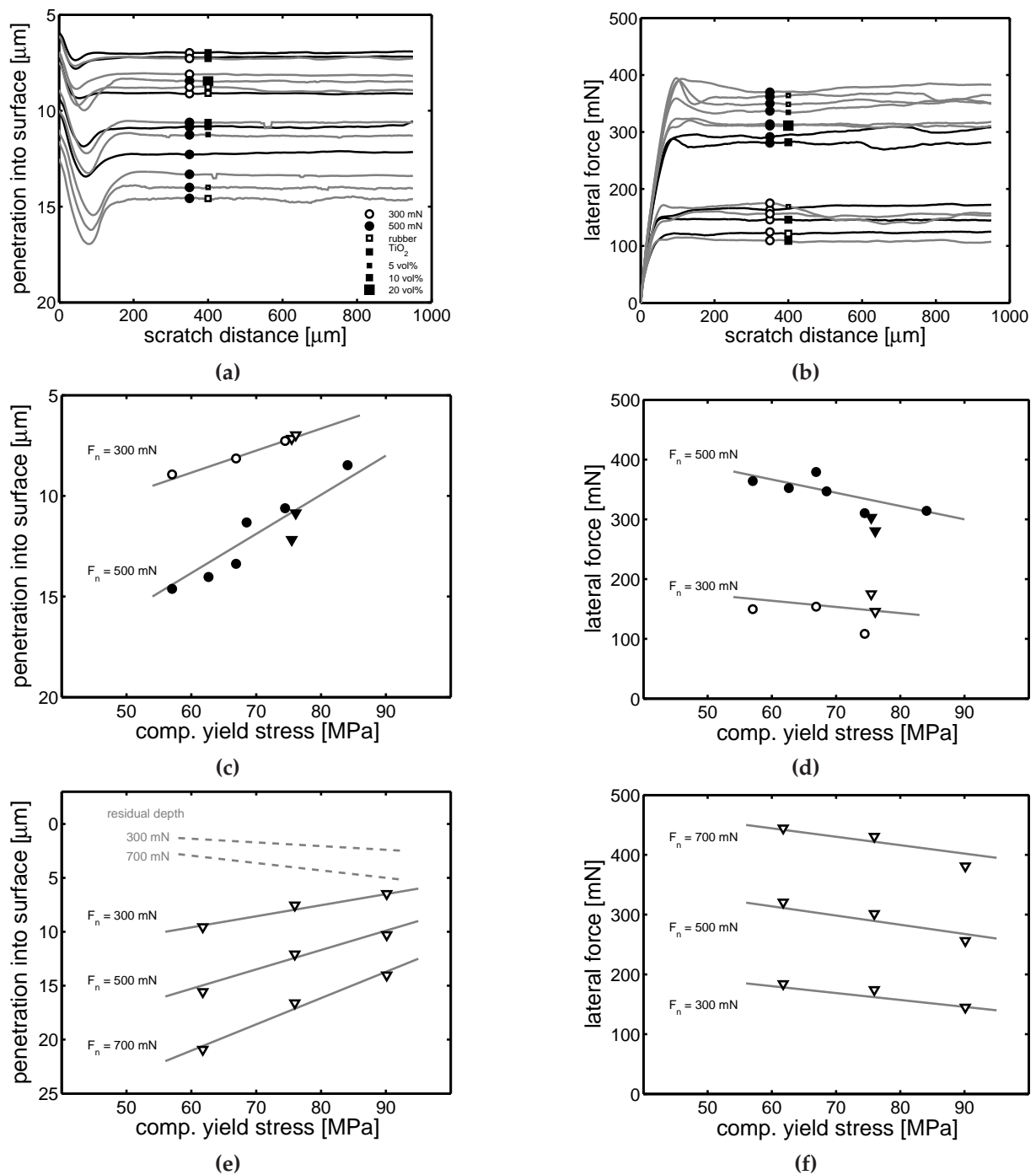


Figure 6.3: Penetration into the surface (a) and lateral friction force (b) as a function of scratch distance for –filled and unfilled– polycarbonate (grey) and epoxy (black), where normal load, and filler-type and fraction are indicated; (c)–(d) mean values from (a)–(b) as a function of yield stress measured in uniaxial compression at 10^{-3} s^{-1} strain rate, of (un)filled polycarbonate (circles) and epoxy (triangles), lines are to guide the eye; (e)–(f) simulations results, where the variation in yield stress originates from shifting the initial viscosity as in Figure 6.1b.

viscous contribution to the strain hardening [45]. This extended EGP model should be used (in future simulations) to give more correct and realistic predictions of the residual deformation.

Apart from using fillers, the yield stress in the epoxy systems can also be influenced by changing the network density by employing different hardeners. We used Jeffamine D230 and D400, with an average molecular weight of 230 and 400, respectively, leading to two epoxy systems with different crosslink densities and, consequently, different intrinsic responses, see Figure 6.4a. The result is a shift in the stress, similar to case (1)

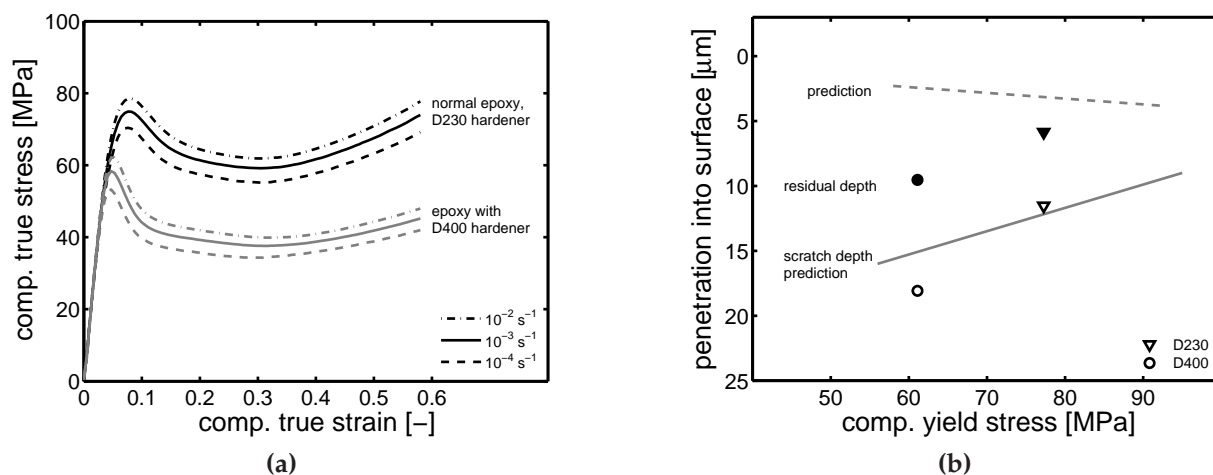


Figure 6.4: (a) Intrinsic response of epoxy, cured with different hardeners (leading to differences in M_c): Jeffamine D230 (material used so far, black lines) and D400 (increased M_c , grey lines) at different strain rates applied. (b) Steady state penetration depth (open symbols) and residual scratch depth (obtained with optical profilometer) (closed symbols), at 500 mN normal load and $0.1 \mu\text{m/s}$ sliding velocity, as a function of the yield stress at 10^{-3} s^{-1} strain rate. Lines are predictions, as in Figure 6.3e.

—a change in $\eta_{0,i,ref}$ — in the previous subsection, while leaving the rate-dependence intact. Penetration into the surface during scratching (500 mN normal load and $0.1 \mu\text{m/s}$ sliding velocity) again depends on the yield stress, see Figure 6.4b, and the simulations show that by only changing $\eta_{0,i,ref}$ the material's response during scratching is captured reasonably well. The residual scratch depth, obtained with the Sensofar Plu 2300 optical profilometer, shows an almost constant 50% recovery for these materials under these experimental conditions. Predictions demonstrate, as in Figure 6.3e, an increase in computed residual scratch depth with decreasing yield stress, illustrating that the error is larger for higher penetration depths. This confirms our hypothesis that the mismatch originates from our model failing to capture load reversal accurately, since this effect is

more pronounced with increased deformation. As a conclusion of this subsection it is shown both by experiments and simulations that scratch resistance improves with yield stress, while much less improvement is found in lateral force. Therefore, we will now investigate low friction in somewhat more detail.

6.2.3 Low friction coatings

As could be concluded from Figures 6.3b, 6.3d and 6.3f, tuning friction by changing the material properties seems to give only minor results. However, it was shown in Chapter 5 that the addition of only a very thin ($1\ \mu\text{m}$) layer of rubbery material on top of the polymer substrate results in a significant decrease in the lateral friction force, but at the expense of an increased penetration depth. Therefore, we return to this vertical stratification policy and compare the addition of a soft layer to the scenario where we add a hard thin surface layer (elasto-plastic, $E = 230\ \text{GPa}$, $H = 10\ \text{GPa}$, and $1\ \text{GPa}$ yield stress). This layer is perfectly connected to the underlying mesh, and redistributes the load over a large surface. The result is a decrease in penetration depth, see Figure 6.5a, and compared to the case with soft top-layer, an even lower lateral friction force, see Figure 6.5b.

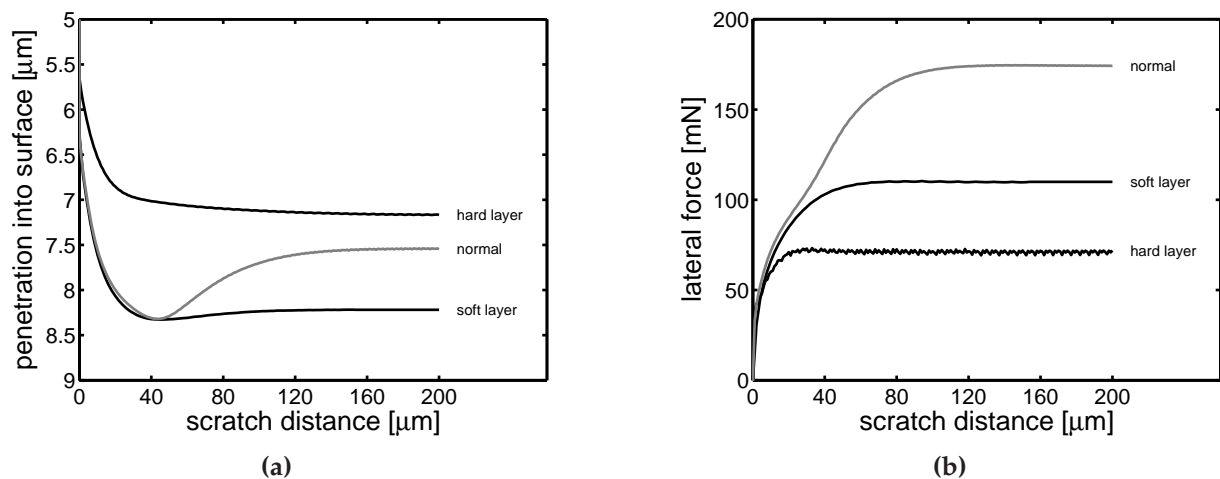


Figure 6.5: Predictions from scratch simulations using model parameters for unfilled epoxy (grey lines), and with a $1\ \mu\text{m}$ top-layer of a rubbery or metallic material. (a) Penetration into the surface and (b) lateral friction force as a function of scratch distance.

Again the results are intriguing as illustrated particularly by Figure 6.5b that shows a two times and even three times lower friction force, by adding a thin (respectively soft

and hard) toplayer only. However, this new strategy needs more investigation, since e.g. in case of the thin hard layer very large (hydrostatic) stresses appear in the hard substrate, so it will probably fail which will result in failure of polymer underneath as well. Moreover, the same μ_f as with the pure polymer is used which might not be correct.

6.3 Wear-resistance

6.3.1 Introduction

In the controlled single asperity experiments, with moderate normal forces applied on indenters having intermediate top angles, the onset of damage is observed in special cases only. With standard polycarbonate or the standard epoxy, that both can be considered as relatively tough materials, damage was never found. However, when using a high normal load on a brittle polymer like polystyrene (PS) regular cracks are formed at the bottom of the scratch surface, see Figure 6.6a. Van Breemen [117] attributed its existence to the event that a critical hydrostatic (tensile) stress (of 40 MPa for PS) was surpassed notably in the wake of the indenter under overall compressive loading, see Figure 6.6b. The crack formed releases the stress. The process repeats and after having moved a distance sufficiently large to build up new stresses, the critical tri-axial stress is surpassed again, explaining the periodicity of the wear events.

Similarly, in our experiments we only found periodic cracking under extreme loading conditions, for epoxy under high normal-load scratching, beyond the limitations of our Nano Indenter XP setup, and for polycarbonate with high hard-filler content, sharp indenter angle, and high normal load. In the analyses we will first shortly repeat Van Breemen's approach, but now on the epoxy used for real coatings, rather than polystyrene or polycarbonate, see Section 6.3.2. Next we investigate in great detail the onset of damage, thus wear, in filled systems, see Section 6.3.3, to conclude –based on these analyses– with recommendations for coatings optimized for wear resistance without sacrificing scratch resistance, see Section 6.4.

6.3.2 Wear in unfilled epoxy systems

To explore the conditions for our epoxy system that lead to a transition from the regime of ductile ploughing and elasto-plastic deformation to macroscopic cracking and wear,

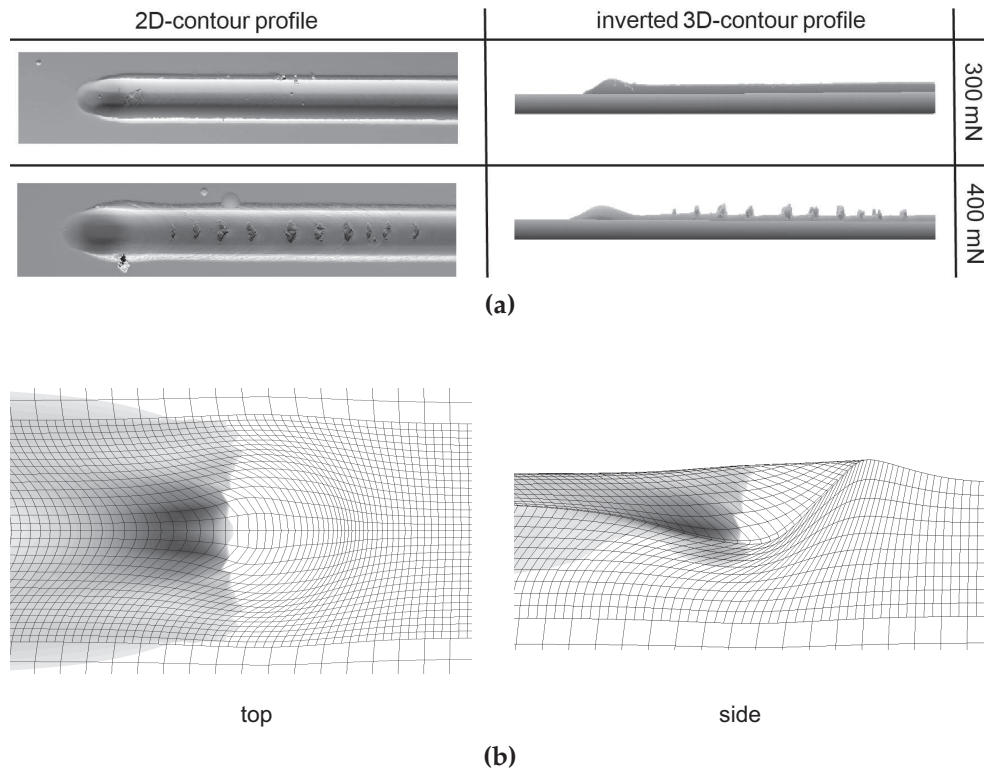


Figure 6.6: Influence of normal load on scratching polystyrene at a sliding velocity of $10 \mu\text{m/s}$; (a) scratch profile generated with optical profilometer, where the onset of wear is clearly visible, manifesting itself as small cracks in the surface profile; (b) the positive hydrostatic pressure as observed in a simulation, where black indicates the maximum hydrostatic pressure, corresponding with the locations in (a) where cracks are observed. Figures taken from [117].

we conducted scratch experiments on a CSM Micro Scratch Tester (MST). Tests were performed with a 90° top angle and $50 \mu\text{m}$ top radius diamond indenter at $100 \mu\text{m/s}$ sliding velocity, and with different normal loads (up to 8 N) applied. Inspecting the scratches afterwards reveals that periodic cracks start to appear at 4 N normal load, while they are absent at lower loadings. Scratch simulations are performed, using a constant local friction coefficient of $\mu_f = 0.27$, and compared with the experiments, see Figure 6.7. Both the penetration into the surface (Figure 6.7a) and the lateral friction force (Figure 6.7b) agree well for 1 and 2 N normal load, whereas they are slightly under-predicted for the 4 N normal-load experiment. It appears that the stress release upon crack formation leads to a further sink-in of the tip which subsequently results in an increased lateral force.

The simulations show that the local hydrostatic stresses in the wake of the indenter tip at

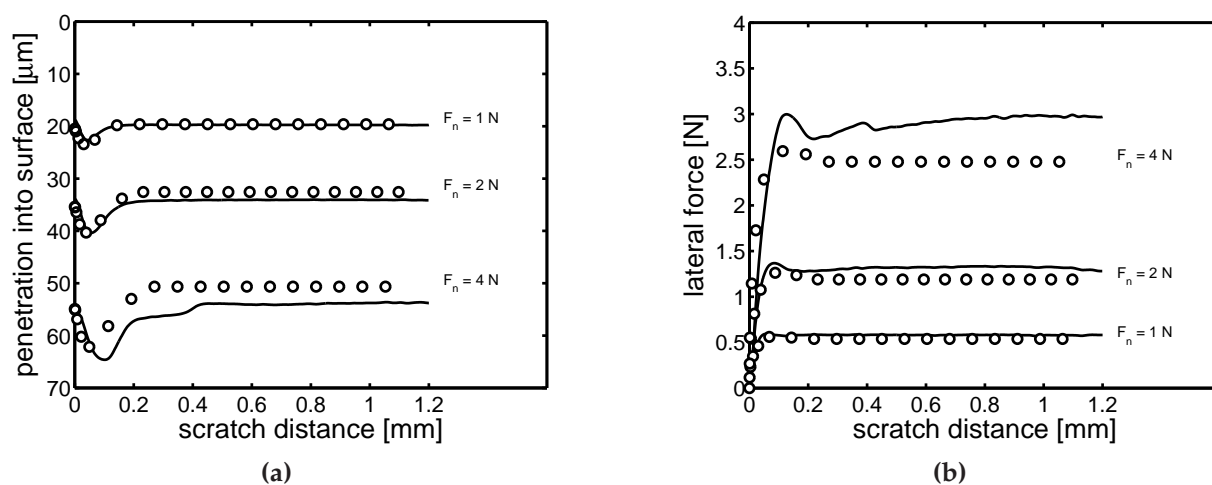


Figure 6.7: Scratch response of unfilled epoxy for different normal loads applied at $100\ \mu\text{m/s}$ sliding velocity. Experimental results (solid lines) compared with simulations (symbols) for (a) the penetration into the surface and (b) the lateral friction force as a function of scratch distance.

2 N normal load reach a maximum value of 130 MPa, providing the lower bound of the critical tri-axial stress that this epoxy material can sustain. At 4 N normal load a maximum value of 180 MPa is reached. Meijer and Govaert [118] showed that for a number of thermoplastic polymers, characterized by their entanglement density $\nu_e \sim 1/M_e$, a semi-log relation with their critical hydrostatic stresses results. Although physically crosslinked ($M_c = 589\text{ g/mol}$ [86]), we compare our lower and upper bound with their findings, see Figure 6.8. The 130–180 MPa range appears to be in line with, and only slightly outside the trend of the other polymers, and the latter might be caused by the difference in molecular interactions, either entangled or physically crosslinked. Figure 6.9 compares the positive hydrostatic stresses from the simulations with the post-scratch profile at 4 N normal load. The cracks, that appear as white regions in the surface profile, are clearly not in the center, as was the case with polystyrene (Figure 6.6a). The simulations confirm this, since the stress maximum, indicated by the black region (black means all stresses $> 150\text{ MPa}$) in the stress field, appears off-center as well.

In conclusion it appears that in homogeneous coatings the onset of wear is caused by a local exceeding of a, polymer dependent, critical positive hydrostatic stress. This (tri-axial tensile) stress is formed in the wake of the indenter, that under its center causes a negative hydrostatic stress (pressure) to bear the normal load. The stress is quantitatively predicted, as is, consequently, the onset of wear.

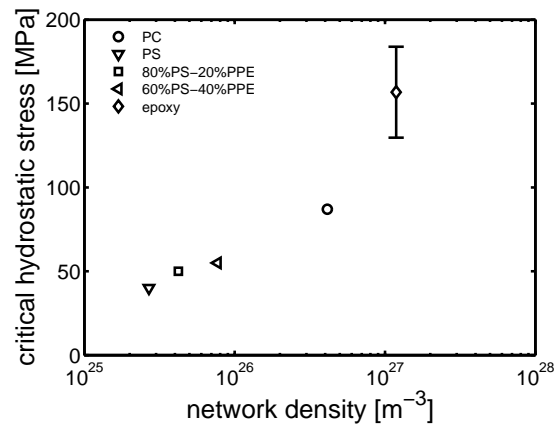


Figure 6.8: Critical hydrostatic stress as a function of (entanglement or crosslink) network density of various amorphous thermoplastic polymers (data from [118]), and of our epoxy system.

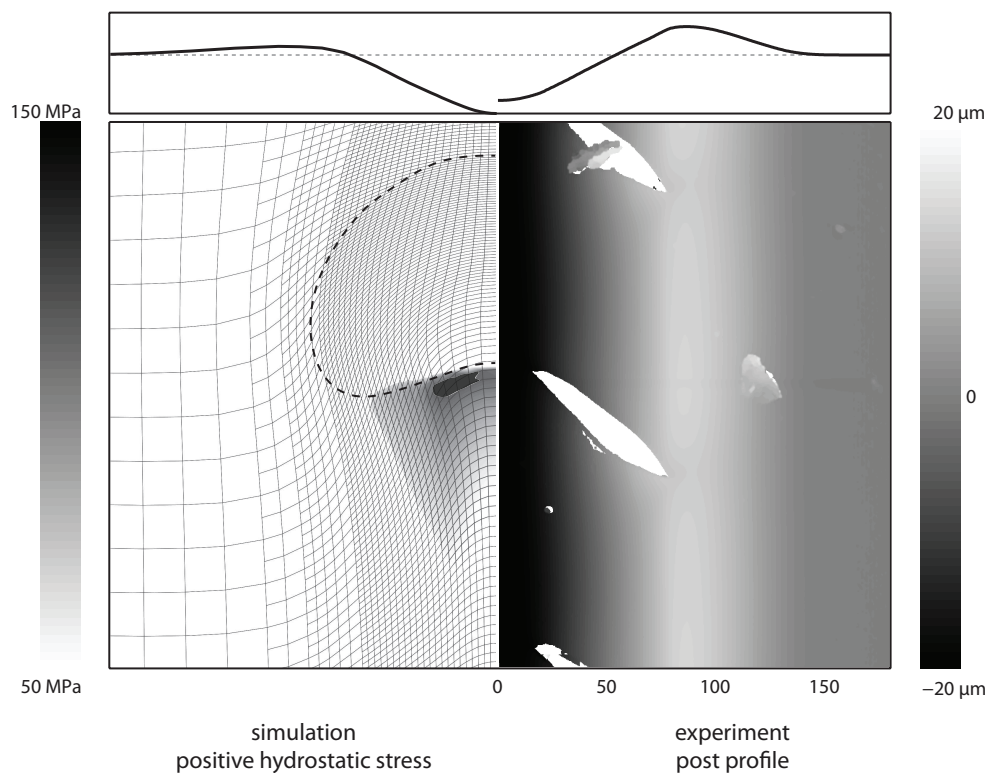


Figure 6.9: (left) Top view of simulation mesh at 4 N normal load (scratch direction upwards), where the grey-shades indicate positive hydrostatic stresses in 50–150 MPa range and the black area indicates all stresses > 150 MPa; the dashed line indicates the contact area; compared to the post scratch profile obtained with the Sensofar (on the right), where the white regions indicate the cracks in the surface. The lines on top of the figure give the experimental and modeled surface height profiles.

6.3.3 Wear in filled epoxy systems

Next we investigate damage in filled coatings, since generally hard fillers are added to the matrix material to help improving the scratch resistance (and to some extent to also lower the lateral friction force). The influence of the modulus of the filler on the macroscopic intrinsic response of the heterogeneous systems is plotted in Figure 6.10 for 10% hard (Figure 6.10a) and soft (Figure 6.10b) particles. Fillers mainly change the yield stress and the strain hardening. To help estimating the magnitude of the (large strain) rubber modulus of the different systems with soft fillers some constant moduli (dashed) lines are drawn. From Figure 5.5 in Chapter 5, we know that the 3D-RVE re-

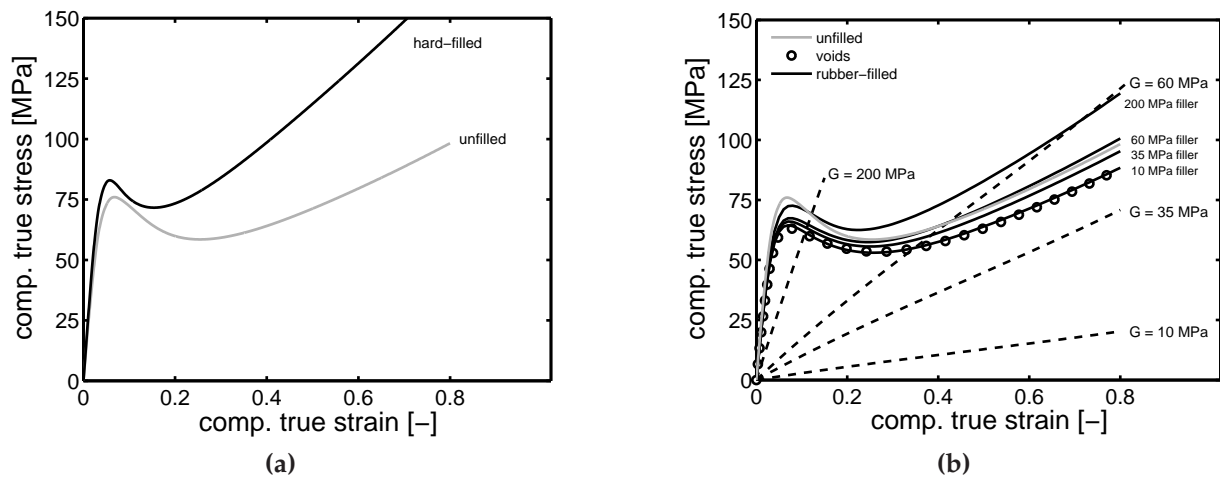


Figure 6.10: The influence of the filler-particles' modulus on the intrinsic response of epoxy (unfilled: grey solid lines) with 10 vol% filler-particles (black solid lines). Values of fillers' modulus are (a) 230 GPa or (b) 10–35–60–200 MPa (rubber). For comparison are given the slopes of lines with different moduli (dashed lines) and the intrinsic response of epoxy with 10 vol% holes (circles).

sponse of the intrinsic material behavior of particle filled epoxy starts deviating from the experiments at a macroscopic strain of around 20%, see Figure 6.11. This is basically surprisingly large, since the strong heterogeneous strain and stress distributions in filled systems easily cause the hydrostatic stress to locally exceed the materials' critical value already at very small macroscopic strains. Apparently only if a large number of critical events happen to occupy a sufficient volume of the RVE, makes the damage percolating through the complete structure and a noticeable failure, as demonstrated by the growing difference between experimental and computed stress beyond 20% strain in Figure 6.11, occurs on the macroscopic scale. We first investigate the strain distributions and analyze critical strains in given parts of the RVE volume. Accordingly, we

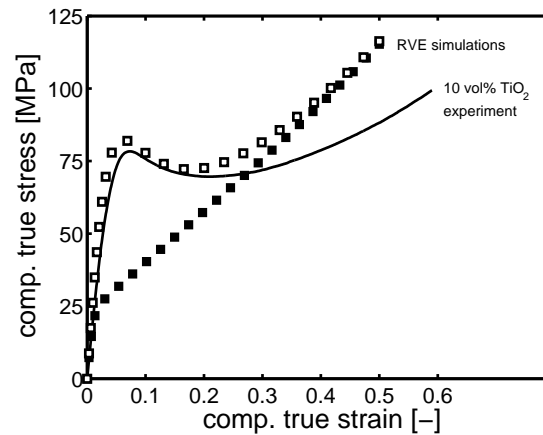


Figure 6.11: Stress-strain response of epoxy filled with 10 vol% TiO_2 at a strain rate of 10^{-3} s^{-1} , experimental result (solid line) compared to predictions from FE-simulation of 3D-RVEs using either $S_a = 17.7$ (open symbols) or $S_a = 0$ (closed symbols) for the epoxy matrix.

compute the stress distributions to finally arrive at an energy criterion where strains and stresses and volumes are incorporated.

Stress and strain based criterion

We focus on the microscopic scale making use of the detailed analyses using 3D-RVEs and compute the distribution of the maximum principal strains at different macroscopic strains of 0.05, 0.2, 0.35 and 0.5, for both the hard and the soft particle filled epoxies, with 10 vol% fillers, see Figure 6.12a. The maximum principle strain (of course) increases with the macroscopic strain applied. Caused by stress and strain localization in the particle filled systems, the maximum principal strain gradually becomes larger than that in the unfilled systems; for hard fillers this effect is much more pronounced.

Exceeding a local maximum in strain does not need to be serious and noticeable on the macroscopic scale. Therefore as a next step we compute the maximum strain reached in a given volume by integrating the strain over the total RVE. For the test volumes we chose 1% and 10% as examples. Figure 6.12b plots the critical maximum value of the principal strain reached in these volumes as a function of the macroscopic strain. Independent of the test volume chosen, the same trends are observed. Hard fillers cause a deviation from the straight (strain-strain) line that characterizes the unfilled epoxy and create a line with a different constant slope. Soft fillers first behave as hard fillers, but at a macroscopic strain of about 20% their slope changes to become identical to that of the

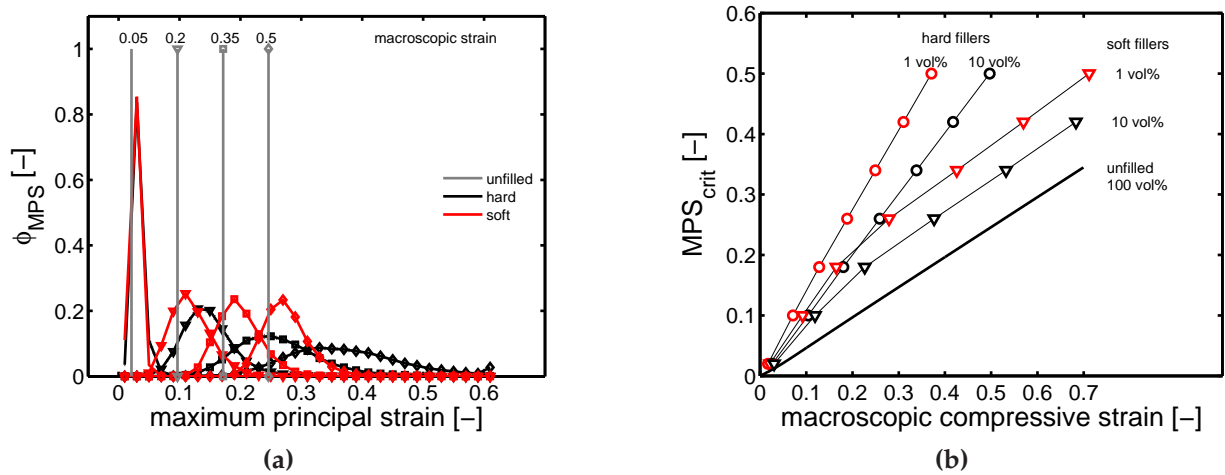


Figure 6.12: (a) Distribution of the maximal principal strains (MPS) in RVEs of 10 vol% particle-filled epoxy compared to the unfilled system as a function of the applied/macroscopic compressive strain. (b) Critical principal strain that is reached by an indicated volume fraction of the matrix as a function of macroscopic strain.

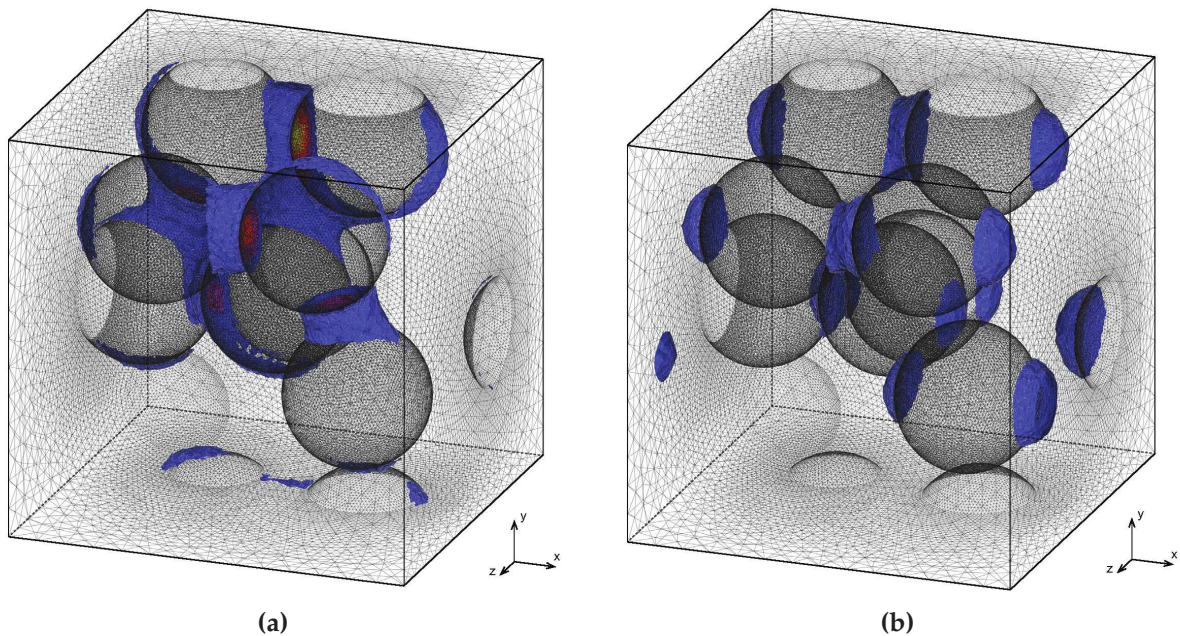


Figure 6.13: Iso-surfaces of positive hydrostatic stresses (lower threshold at 10 MPa) at 2.5% macroscopic strain in a (a) hard-particle filled system (RVE is compressed in z-direction), and (b) soft-particle filled system (RVE is compressed in x-direction).

unfilled epoxy. This is an interesting intermediate result; the more so since (also) at 20% macroscopic strain the experimental hard particle filled epoxy response starts deviating from the RVE response, see Figure 6.11.

Although the volume weighted strain distributions seem important, from the pure systems we know that a (hydrostatic) stress based criterion works extremely well (see Section 6.3.2). As shown in Chapter 3, detailed analyses on 3D-RVE level provide these stresses as well. In Figure 6.13, which is copied from Figures 3.7 and 3.8, we plot iso-surfaces of positive hydrostatic stresses at a relatively low macroscopic strain of 2.5%. Therefore we extend our analysis to arrive at an energy-based criterion, since energy contains the product of stresses and strains.

Energy based criterion

Figure 6.14a shows the distribution of the positive hydrostatic stresses in the matrix. From this distribution we compute the energy using the volume weighted strain distribution:

$$E(t) = \sum_{i=1}^N V_i(t) \varepsilon_i(t) \sigma_i^H(t), \quad (6.3)$$

which is a summation, over all elements ($i = 1, \dots, N$) with positive hydrostatic stress ($\sigma^H > 0$), of the product of σ^H , the elements' volume V_i , and the equivalent strain ε_i . The result is shown in Figure 6.14b.

Now let us assume that the most important mode of failure is caused by particle-matrix debonding, so we relate the result from Equation (7.1) to the total interfacial area $A_{tot} = N_{filler} 4\pi R^2$ where N_{filler} represents the number of particles in the RVE and R is the mean particle radius. Figure 6.15 shows this energy per interfacial area as a function of macroscopic strain. Since the same microstructure is considered, but with different filler material-properties, a scaling of Figure 6.14b results. Clearly, the energy per interface-area rapidly increases for the hard-particle filled system, while for the soft-particle filled system the increase is much more moderate and by changing the rubber modulus even low plateau values are reached. Figure 6.15b gives a closer view on the most interesting region around a macroscopic strain of 20% where damage became noticeable on the macroscopic scale. The hard-particle filled system surpasses at 20% macroscopic strain a critical value for the energy per interface-area of 1 kJ/m². This is a nice result indeed. The soft particle filled systems reach this critical value at very large macroscopic strains,

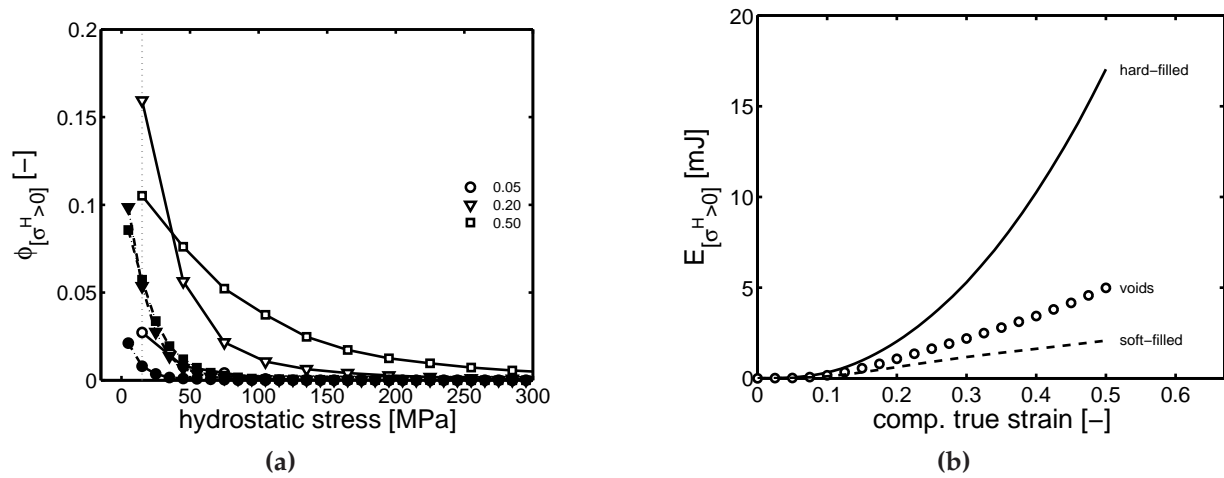


Figure 6.14: (a) Distribution of positive hydrostatic stresses in the matrix of 10 vol% hard-particle filled (solid lines) and 10 vol% soft-particle filled (dashed lines) RVEs at different macroscopic strains (indicated by symbols) (soft-filled: 10 MPa modulus). (b) Energy, caused by these positive hydrostatic stresses multiplied with the volume weighted strain, as a function of macroscopic strain.

or never at all, depending on the filler modulus relatively to the rubber modulus of the pure matrix in the strain hardening regime.

To demonstrate the latter, Figure 6.16a gives a cross section of Figure 6.15b showing the energy per surface area at 30% macroscopic strain for filler moduli G normalized with the large strain matrix rubber modulus G_r . Clearly a particle modulus close to the matrix rubber modulus gives an optimum low energy per surface. This is a very useful result that can, and will, be used in optimizing the microstructure. Another pretty interesting point is the influence of the size of the particles. Figure 6.16b illustrates that, for a given volume fraction fillers, the particle size directly, and strongly, influences the surface area A , thus smaller particles greatly lower the energy per surface values.

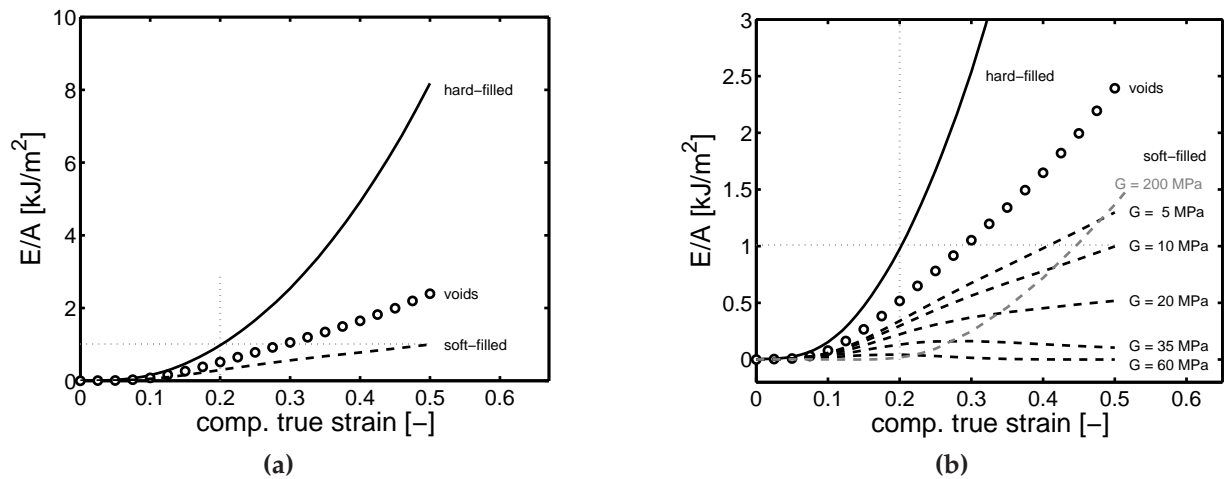


Figure 6.15: (a) Energy caused by the positive hydrostatic stresses, divided by the particle-matrix interfacial area, as a function of macroscopic strain. (b) Zoom in of (a) showing results for more values of the soft particles' modulus.

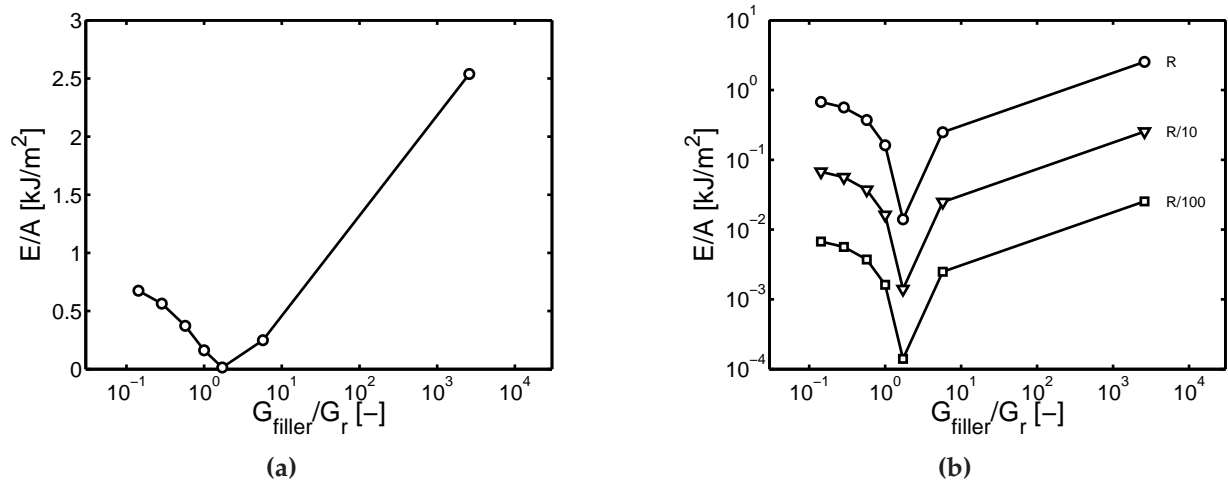


Figure 6.16: (a) Energy per surface (E/A) at 30% strain as a function of matrix' strain-hardening (G_r) normalized filler modulus G_{filler} , as a function of macroscopic strain, and (b) influence of the filler size, represented by the radius particle R , showing that smaller particles are to be preferred.

6.4 Optimizing for scratch- and wear resistant coatings

From the results presented in Figures 6.11 and 6.15 we concluded that in coatings with hard fillers at a macroscopic strain of 20% apparently a critical cumulative damage situation is reached at the averaged RVE level, expressed in a critical value of the energy per unit interface. Interestingly, this critical value is also reached, be it at larger macroscopic strains, with softer fillers. However, this is not generally true for all moduli and a clear optimum in soft filler modulus exists, where this critical energy per surface value is never reached, see Figures 6.15 and 6.16.

What remains is to find an optimum compromise between scratch resistance, that requires a high yield stress and therefore high filler moduli, and wear resistance, that benefits from a low filler modulus, aiming at avoiding critical energy-per-surface-interface values. The preference for a choice of the smaller filler particles, greatly influencing their total surface area A , was already discussed. In this last section we want to answer how hybrid filled systems that combine hard and soft filler particles should be designed. For quantitative answers on that question, 3D-RVE analyses are required, but present limitations in both computational power and memory availability limit their use to the size and complexity of the RVEs shown in Figure 6.13. Therefore we return to 2D periodic RVEs in plane strain loading, and realize and accept that our answers are limited to be qualitative only.

Basically two principally different concepts of hybrid filler systems can be thought off: (i) a mixture of hard and soft filler particles with different ratio's in particle size, and (ii) a soft shell around a hard filler-particle core, see Figure 6.17. Particle coordinates for the 3D-RVE are generated via the procedure described in Chapter 2. Subsequently, 2D-RVEs are obtained by taking cutting planes of the 3D-RVE. The 2D-RVE is accepted if its area-fraction of fillers equals the 3D-RVE's volume fraction within 1% error. Figure 6.17a shows an example of a meshed 2D-RVE with 10% hard fillers (black regions); in Figure 6.17b another 10% of equal-sized soft fillers is added (white regions), while Figure 6.17c shows a 2D-RVE with particle-size ratio $D_h/D_s = 5$ for the hard/soft-particles. Finally, in Figure 6.17d the soft phase appears as a shell around a hard-particle core. Not that, since the 2D-RVE is a cross-section of a 3D-RVE, some 'fillers' in 2D only consist of the soft 'shell'.

The stress-strain response of 3D-RVEs is compared to plane-strain 2D-RVEs in Figure 6.18. Clearly the 2D-RVEs respond considerably stiffer than the 3D-RVEs when

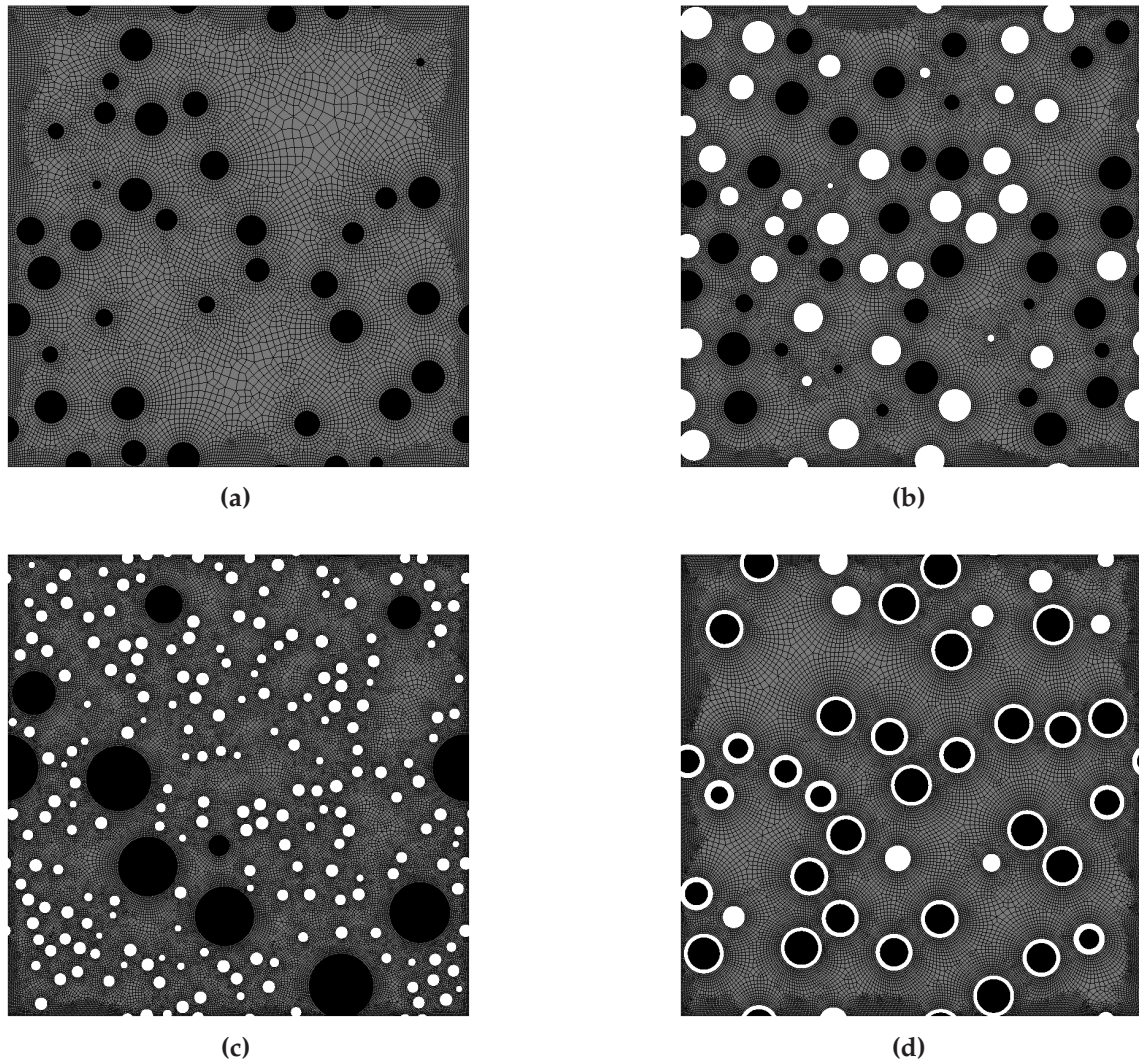


Figure 6.17: Meshed 2D-RVEs that are generated from 3D-RVEs' cross-sections; (a) only 10 vol% hard-particle filled (black) and (b) with additional 10 vol% equal-sized soft fillers (white); (c) ratio in particle size hard/soft: $D_h/D_s = 5$; (d) hard fillers as core surrounded by soft shells.

hard fillers are used, Figure 6.18a, while with soft fillers strain softening is completely absent, Figure 6.18b. The stiffer response results in earlier flow by sequential yielding compared to 3D. As a consequence the magnitude of the yield stress is predicted less accurate, as demonstrated by the observation that it does not increase by the addition of 10 vol% hard fillers. The strain hardening is still more pronounced, see Figure 6.18a. The computation of the energy per interface-area is still qualitatively correct as will be shown below.

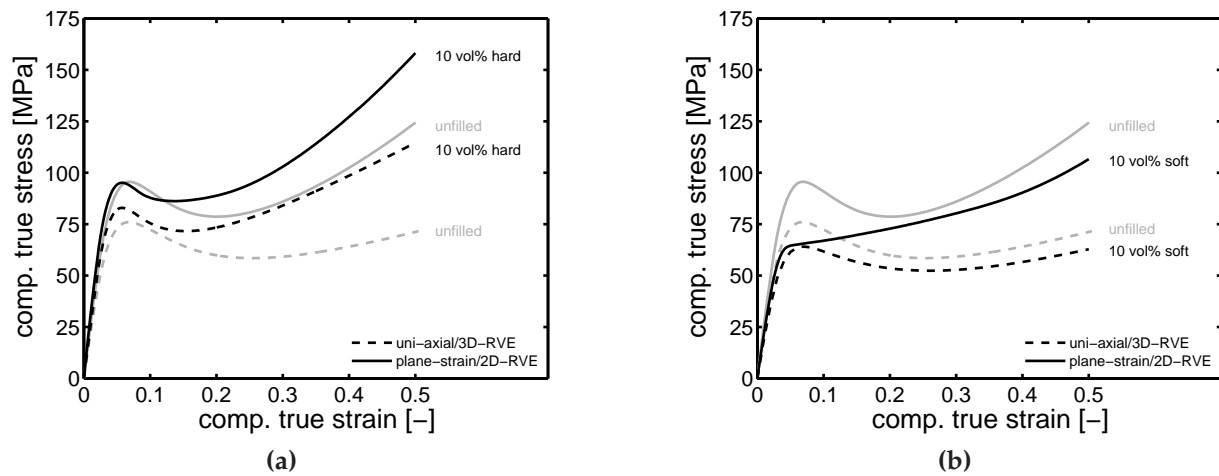


Figure 6.18: Comparison of the stress-strain response of 3D-RVEs in uni-axial compression (solid lines) and of 2D-RVEs under plane-strain loading; response of unfilled epoxy (grey lines) is compared with those of 10 vol% (a) hard-particle and (b) soft-particle filled systems (black lines).

Figure 6.19 summarizes all results of the computations with 2D-RVEs with different complex microstructures. Figure 6.19b plots the energy per interface-area versus strain for hard- and two soft-filled materials whose intrinsic response is given in Figure 6.19a. Compared to Figure 6.15 the vertical axis differs considerably, while for hard fillers the increase in energy starts at larger strains. The prediction for the soft-filled system with 35 MPa filler-modulus is qualitatively OK, while that for low 5 MPa modulus already starts increasing in an early stage of the deformation before leveling off. This is due to the position and orientation of places where the positive hydrostatic stresses occur, which is in the direction of deformation at the poles of the fillers. Therefore, build-up of these stresses starts soon after deformation commences, but they disappear when sequential yielding initiates. This in contrast with the hard-fillers' stress localization which starts at the equators of the particles, and most importantly, between interacting hard particles. In 3D, interactions occur with particles in all directions, whereas in 2D they can initiate in one plane only, resulting the energy to increase only in a later stage of the deformation.

Figure 6.19d shows the evolution of E/A for the 2D-RVEs with combined soft and hard filler-particles, both at 10% filler-content, for different ratios in diameter hard/soft D_h/D_s . The stress-strain responses of these systems are shown in Figure 6.19c. Clearly,

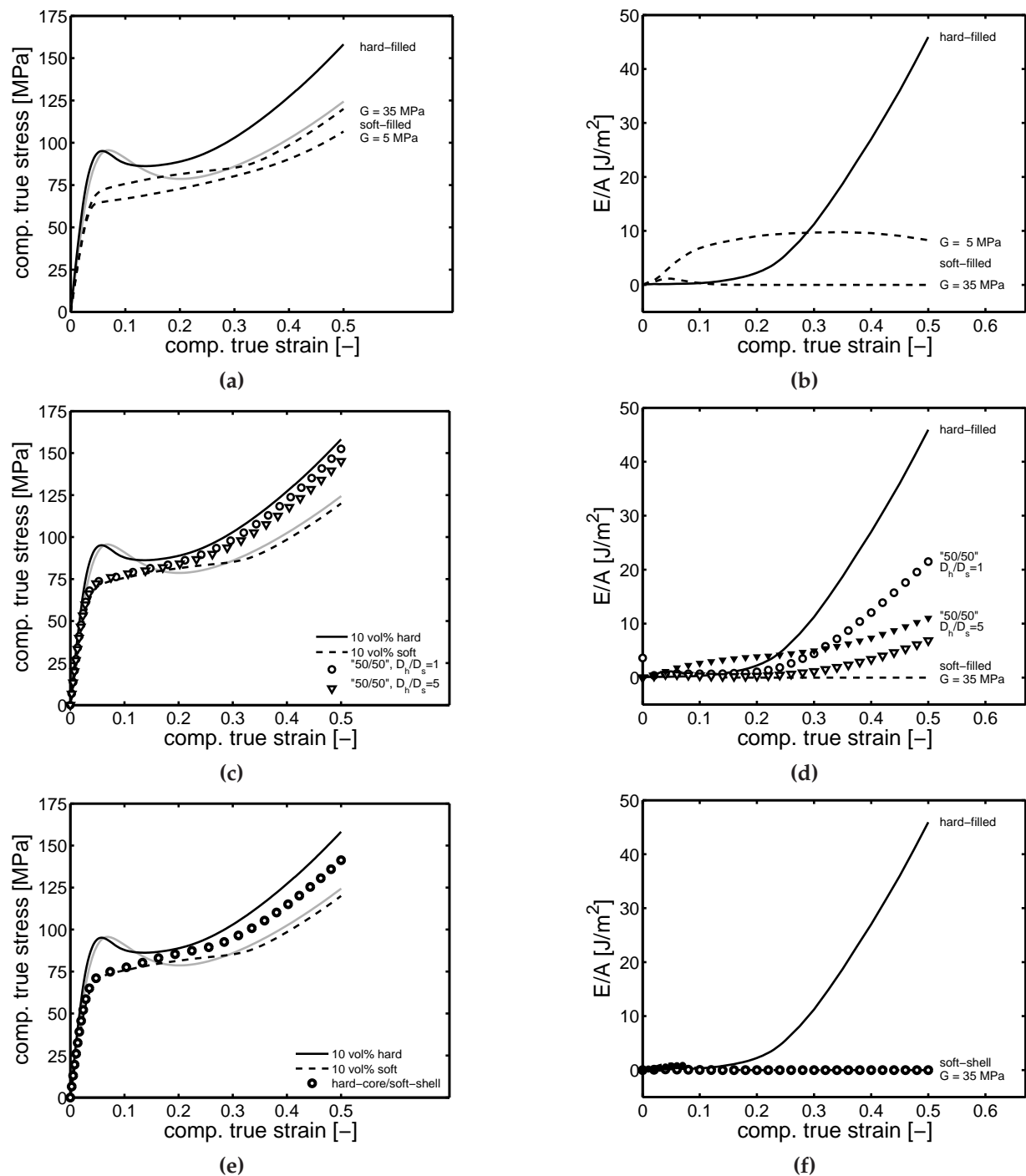


Figure 6.19: Stress-strain response and energy per interfacial area in 2D-RVEs. (a) Stress-strain response of unfilled (grey) and 10% hard (solid black line) and two soft (black dashed lines) particle filled systems; (b) energy per interface area of these systems; (c) and (d) as (a-b) now for mixed hard and soft fillers with two ratios in particle size hard/soft: D_h/D_s , large and small triangles $G = 35$ and 5 MPa, respectively; (e) and (f) as (a-b) now for hard fillers as core surrounded by soft shells.

combining hard with the optimized soft fillers –35 MPa modulus (open symbols) compared to 5 MPa (closed symbols)– causes E/A to increase at a later stage compared to the 10% hard-filled system. Moreover, this effect is more pronounced when the relative soft-particles' diameter is decreased, see Figure 6.17c. Adding soft fillers mainly influences the yield stress, see Figure 6.19c, while in the post-yield region strain hardening appears to be dominated by the hard particles. The particle-size ratio D_h/D_s has little effect on the stress-strain response.

To check the predictive quality of the plane-strain approach, we take the simple case of equal D_h/D_s , since this is relatively straightforward to implement in 3D. RVEs with 32 particles of 20 vol% total filler loading are generated, and the fillers are randomly divided to be either hard or soft. Predictions of stress-strain response and energy per interface-area are shown in Figure 6.20. Qualitatively, the effect on E/A is identical in

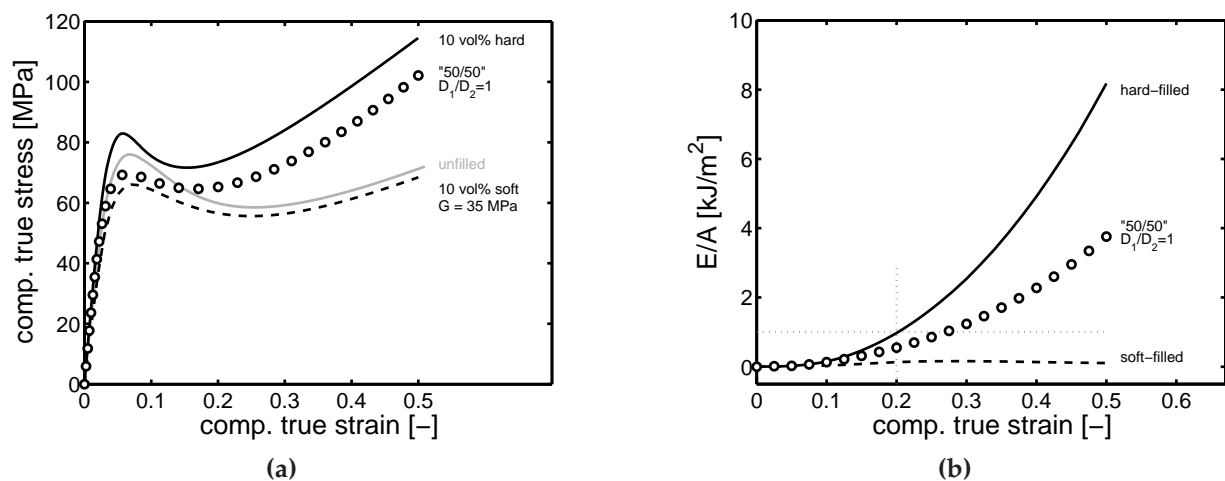


Figure 6.20: Predictions from simulations using 3D-RVEs that contain 10 vol% hard particles (black solid lines), 10 vol% soft particles (dashed lines), or 20 vol% filler content with 50%-50% mixture of hard and soft fillers (circles); (a) Macroscopic stress-strain response (unfilled epoxy included in grey, for comparison), and (b) the energy in the 3D-RVEs, caused by the positive hydrostatic stresses, divided by the particle-matrix interfacial area, as a function of macroscopic strain.

both 2D and 3D, compare Figures 6.19d and 6.20b. The stress-strain response, however, is very different. In full-3D the yield stress is roughly in between unfilled and soft-filled, localization in the form of strain-softening after yield is observed, and upon strain hardening the hybrid system outperforms unfilled epoxy as it increases parallel to the hard-filled system, see Figure 6.20a. The effects are more extreme in plane-strain, where the response basically 'jumps' from that of soft-filled (identical yield stress) to

that of the hard-particle filled system (nearly identical large strain response), see Figure 6.19c.

The most interesting case in terms of E/A -build-up is that of a soft shell around a hard-particle core, Figure 6.19f. With the 5 MPa filler-modulus (closed symbols) the effect is only minor, while no energy increase from the positive hydrostatic stresses is observed with the optimized 35 MPa filler-modulus. This is a most interesting result that deserves more future investigation. The stress-strain response (Figure 6.19e) appears very similar to the other mixed hard/soft filled systems (6.19c), which suggests that the mere presence of the combined hard/soft phase is more dominant than the exact morphology of the microstructure.

6.5 Conclusions and recommendations

Conclusions

- Scratch resistance is proportional to the material's yield stress. Increasing the yield stress via an increase in crosslink density gives better results than by applying progressive accelerated aging, since it directly reduces the penetration into the surface.
- Friction is only slightly dependent on yield stress. More promising for low friction coatings is to follow the strategy of vertical stratification. Very thin either soft or hard layers on top of the coating decrease the lateral friction force with a factor 2 and 3, respectively.
- In homogeneous coatings (the onset of) wear is caused by a local exceeding of a, polymer dependent, critical positive hydrostatic stress, which strongly correlates to the polymer's network density, either entangled or crosslinked.
- Wear in filled coating systems is experienced first in hard particle filled coatings and it starts to become noticeable on the macroscopic scale at a macroscopic strain of around 20%. The cause of (the onset of) wear proves to be surpassing a critical value of the energy E , stored in the RVE, divided by the total interfacial area A , between particles and matrix in the RVE, of $E/A = 1 \text{ kJ/m}^2$ for epoxy-TiO₂.
- For soft fillers the critical value for the energy per interfacial area is also reached, but at large macroscopic strains, depending on the filler modulus G relative to the rubber modulus G_r of the matrix in the large strain regime. Neither large,

nor small (e.g. voids) moduli are to be preferred; optimum values of this ratio are around $G/G_r = 1$, and give a plateau value, close to zero, of the energy per interface area.

- The particle size of the fillers directly determines the interfacial area for a given volume fraction fillers. The value of E/A is directly influenced. Consequently are smaller particle diameters to be preferred.
- To achieve wear resistance without sacrificing scratch resistance, hybrid filler systems should be used.
- If a mixture of hard and soft particles is chosen, then their diameter ratio D_h/D_s (and, consequently, for a given volume fraction their number ratio N_h/N_s) should be different from 1. A hard-soft ratio D_h/D_s of 5 is already much better, 10 could give further improvement, but is not yet explored due to computational constraints.
- A second hybrid system that works even better is a core shell system with the hard particles as core and the soft polymer as shell. As choice for soft material modulus, also here $G/G_r = 1$ is optimum.

Recommendations

- Quantifying residual deformation demands a constitutive model that accounts for the Bauschinger effect in load-reversal.
- Further investigation of the vertical stratification strategy to not only improve the scratch resistance, but to also lower the friction force, need to be performed.
- Attention should be paid to damage in the hard thin top coating and to failure in the interface between hard top and softer bottom layer.
- More importantly is to systematically vary the thickness of the top layer, its properties, and its position, since layers below the surface could be rather interesting as well.
- Finally the number and thickness ratio of the alternating layers in the stratified coating structures could be interesting parameters to vary. (Teeth, nacre and shell structures are made that way).
- The research into the design rules for optimized microstructures for combined scratch- and wear resistance just started. Many variables have to be varied, to start with the volume fractions in the different hybrid soft/hard systems.

-
- And of course the modulus of the soft rubber is a parameter also in these hybrid systems. A value of $G/Gr = 1$ seems to be beneficial here as well.
 - But most important is to perform 3D simulations on both the microscopic RVE scale and the macroscopic scratch test scale. In some situations dealt with in Section 6.4 this is technically still feasible.
 - Despite that also for hard fillers, the smaller particle sizes are to be preferred, given the low value of E/A in those cases, the opposite: applying very large particles, in the order of (but slightly smaller than) the total coating thickness, could be interesting. Rather than penetrating into the coating matrix material, the indenter in that case could “jump” from one “big stone” to the other, preventing visible scratch damage.

Conclusions and Recommendations

7.1 Conclusions

This thesis discusses the prediction of the performance of particle-filled polymers in sliding friction. The approach adopted is based on homogenizing the mechanical response of particle filled systems and, subsequently, use the macroscopic constitutive equation thus obtained to predict and analyze the materials' frictional response. The methodology is applied first to model systems with a well characterized thermoplastic polymer matrix –polycarbonate–, filled with either hard (TiO_2) or soft (rubber), order 100 nm sized filler particles. This enables developing and refining the experimental and numerical techniques. Thereafter the approach is applied to a class of polymers that is more relevant to coating applications, thermosetting polymer systems; for that a standard epoxy system was selected.

Intrinsic response

To investigate the intrinsic mechanical response of particle-filled systems, three dimensional representative volume elements (3D-RVEs) are constructed as a simplification of their microstructure. The purpose of the finite element simulations with these 3D-RVEs is twofold, they provide homogenized material parameters necessary for the scratch simulations, but equally important, they enable the analysis of local (inter-particle) deformations leading to microscopic, and ultimately, macroscopic wear.

1. It is shown that only 30 particles are sufficient to give a reliable RVE response with little scatter.
2. Using only a single-mode implementation of the constitutive framework to describe the polymer matrix already proves to describe key features of the intrinsic mechanical response of complex soft- and hard-particle filled polymer systems, such as an increasing initial modulus, yield stress and strain hardening with hard-particle filler-content, and a decreasing initial modulus and yield stress for soft-particle filler-content.
3. Quantitatively, these simulations under-predict the small strain response, however, but using multiple relaxation modes proves to be a major improvement. Multi-mode modeling implies that the initial response of the matrix is modeled stiffer, as it is in reality, compared to the single-mode modeling. This accurate modeling approach also reveals more intensified local stresses and strains, implying that microscopic failure commences at an even earlier stage.
4. Comparing the RVEs' numerical results to experiments shows that all the rate-dependency in the systems' responses originates from the polymer matrix, the fillers only change the magnitude of the stress response.
5. Furthermore, with the multi-mode modeling, the small-strain response of the particle-filled systems is captured accurately. The yield stress of TiO₂-filled PC was initially under-predicted, but as this matrix-filler combination is known to show accelerated aging, increasing the parameter representing the age proved sufficient.
6. The large-strain predictions of the TiO₂-filled systems, both with PC and epoxy matrix, shows to progressively deviate after approximately 20% compressive strain. In the simulations it is assumed that the particles perfectly adhere to the matrix, and no failure of the matrix itself is modeled. Although tested in compression, the simulations show a large build-up of positive stresses and strains, already starting at small macroscopic deformations. This implies a sequential occurrence of local failure, finally combining to grow into a macroscopic crack, that leads to a decreased macroscopic stress-response.
7. The soft-particle filled polycarbonate systems are accurately described by the sim-

ulations. This in contrast to the epoxy based soft-particle filled systems, where a significant over-prediction of the stress-response is observed. Initially, this deviation was attributed to differences in the quality of curing and a poor particle-distribution, but examining the microstructure with electron-microscopy shows serious voiding of about 10 vol% 200–300 nm sized uniformly distributed cavities. Incorporating these voids via a multi-level modeling approach shows that this explains the observed experimental response.

Scratch response

The scratch performance of the particle-filled model systems is tested with the single-asperity sliding friction test. The fillers change the intrinsic mechanical response, and therefore also the scratch response.

8. Hard fillers enhance the scratch resistance, as the increased yield stress leads to a decrease in surface penetration. This causes the lateral friction force to decrease since less material is moved in front of the indenter tip. In principal, soft fillers have the opposite effect. They decrease the yield stress, and thus cause the penetration into the surface to increase. As less material is moved in front of the indenter, a decrease in lateral friction force results.

The RVE-simulations and compression experiments provide homogenized material parameters that are used in scratch simulations. Friction is considered as a complex physical phenomenon involving many variables. Here we adapted a different approach, inspired by its successful application to unfilled polycarbonate [12], focussing on introducing more complexity in the local deformation processes, while simplifying the friction modeling by using the Amontons-Coulomb friction law.

9. The scratch simulations reveal that the response is very sensitive to relatively small errors in the modeling. This includes the input that relates to modeling of the experiment, i.e. the influence of the exact indenter-geometry, as a small offset in the shape leads to incorrect predictions of the penetration depth, and to the materials' constitutive modeling, as shown for the rubber-filled epoxy sample, where small differences in the Poisson's ratio lead to large differences in the predicted frictional response.

10. Employing proper constitutive modeling of the materials' intrinsic mechanical response and a simple velocity-independent friction model in finite element simulations revealed that only a single local friction coefficient (μ_f) is necessary to predict the frictional response of our unfilled and particle filled systems for different sliding velocities and for different normal loads applied. The exact value of μ_f depends on the indenter-matrix combination, but it is not affected by the filler particles. These only change the intrinsic mechanical response and, therefore, the deformation field around the indenter leading to a change in the total scratch response.

Scratch and wear resistance

The hybrid experimental-numerical approach is successfully used to quantify the frictional response of different particle-filled systems over a range of experimental conditions. Its advantage is that the simulations enable to distinguish between effects that are related to the adhesive interaction and effects that originate from the mechanical response of the substrate. Via the RVE-simulations also deformation processes at the smaller –inter-particle– length scale become accessible. The approach presented here shows promise as a design tool for the development of improved scratch resistant materials.

11. Scratch resistance is controlled by the yield stress of the polymers that constitute the coating. Increasing the yield stress can be achieved by (i) adding hard particle fillers, (ii) increasing the crosslink density in thermoset coatings or by (iii) introducing progressive ageing in thermoplastic coatings. The first two measures are to be preferred and give the best results.
12. Friction is only slightly dependent on yield stress. More promising for low friction coatings is to follow the strategy of vertical stratification. Very thin either soft or hard layers on top of the coating decrease the lateral friction force with a factor 2 and 3, respectively.
13. Wear in homogeneous coatings depends on the critical hydrostatic stress that, when surpassed, initiates cavity formation. This releases the stress that, on further scratching, builds up again, so the process repeats. The maximum tri-axial tensile stress a polymer can sustain is proportional to its network density, which

consequently should be maximized.

14. Wear in heterogeneous coatings depends on a critical energy E per interfacial area A that, when surpassed, initiates macroscopic changes in the intrinsic material response. For the system epoxy-TiO₂ the critical value of E/A equals 1 kJ/m². Given the dependence of the interface area A between matrix and filler on the particle diameter, smaller particles are better. For soft particles, the optimum modulus G is equal to the rubber modulus of the matrix G_r at large strains: $G/G_r = 1$.
15. To achieve wear resistance without sacrificing scratch resistance, hybrid filler systems should be used. If a mixture of hard and soft particles is chosen, then their diameter ratio D_h/D_s (and, consequently, for a given volume fraction their number ratio N_h/N_s) should be different from 1. A hard-soft ratio D_h/D_s of 5 is already much better, 10 could give further improvement, but this is not yet explored due to computational constraints. A second hybrid system that works well is a core shell system with the hard particles as core and the soft polymer as shell. As choice for soft material modulus, also here $G/G_r = 1$ is most probably optimum.

7.2 Recommendations

Scratch resistance

1. For the in-situ response, i.e. to predict the scratch experiment itself, using the standard version of the EGP [44] suffices, since the scratch response is dominated by the bow wave in front of the indenter, where loading conditions are predominantly compressive and no load reversal has occurred yet. The extended EGP model [45, 119], or a similar model that properly accounts for the so-called Bauschinger effect, should be used to also correctly and quantitatively predict deformation after unloading. This is required to find the residual scratch depth that is a true measure for the scratch resistance of coatings.

Low friction

2. As formulated in Section 6.5, more attention should be paid to the new vertical stratification strategy to arrive at low friction coatings. A number of computational-technical questions remain to be answered. Many different topologies and coating designs are interesting and challenging to investigate further. Obvious parameters are thickness, properties, positions and orientation –on or relatively to the surface– and number of the layers; they are all worthwhile exploring.

Wear resistance

3. In Chapter 6 we derived a new criterion for the onset of wear in heterogeneous systems, and a critical value of $E/A = 1 \text{ kJ/m}^2$ was found for the coating system epoxy-TiO₂. The energy E here equals the RVE-integrated product of the local positive hydrostatic stress ($\sigma_i^H > 0$) and the volume (V_i) weighted local strain (ε_i):

$$E(t) = \sum_{i=1}^N V_i(t) \varepsilon_i(t) \sigma_i^H(t). \quad (7.1)$$

The interface area A equals the total interface in the RVE between matrix and filler:

$$A = N_f 4\pi R^2. \quad (7.2)$$

The concept of this new damage criterion E/A should be tested on more standard composite structures and materials. And it goes without saying that the hybrid coating systems proposed, that aim at improving wear resistance without sacrificing scratch resistance, are an onset only. A systematic investigation of the potential of the proposed hybrid microstructures, combined with a systematic variation in volume ratio's and constituent properties, is recommendable and could be performed straightforward.

References

- [1] M Urbakh, J Klafter, D Gourdon, and J Israelachvili. The nonlinear nature of friction. *Nature*, 430 (6999):525–528, 2004.
- [2] Y Dong, Q Li, and A Martini. Molecular dynamics simulation of atomic friction: A review and guide. *J. Vac. Sci. Technol., A*, 31(3):030801, 2013.
- [3] FP Bowden, AJW Moore, and D Tabor. The Ploughing and Adhesion of Sliding Metals. *J. Appl. Phys.*, 14:80–91, February 1943.
- [4] JF Archard. Elastic deformation and the laws of friction. *Proc. R. Soc. London, Ser. A*, 243(1233): 190–205, 1957.
- [5] JA Greenwood and JJ Wu. Surface roughness and contact: An apology. *Meccanica*, 36(6):617–630, 2001.
- [6] B Briscoe. Isolated contact stress deformations of polymers: the basis for interpreting polymer tribology. *Tribol. Int.*, 31(1–3):121–126, 1998.
- [7] W Brostow, W Chonkaew, R Mirshams, and A Srivastava. Characterization of grooves in scratch resistance testing. *Polym. Eng. Sci.*, 48(10):2060–2065, 2008.
- [8] R Browning, GT Lim, A Moyse, HJ Sue, H Chen, and J Earls. Quantitative evaluation of scratch resistance of polymeric coatings based on a standardized progressive load scratch test. *Surf. Coat. Technol.*, 201(6):2970 – 2976, 2006.
- [9] A Krupička, M Johansson, and A Hult. Use and interpretation of scratch tests on ductile polymer coatings. *Prog. Org. Coat.*, 46(1):32–48, 2003.
- [10] XQ Pei, R Bennewitz, M Busse, and AK Schlarb. Effects of single asperity geometry on friction and wear of peek. *Wear*, 304(1-2):109–117, 2013.
- [11] BJ Briscoe, E Pelillo, and SK Sinha. Scratch hardness and deformation maps for polycarbonate and polyethylene. *Polym. Eng. Sci.*, 36(24):2996–3005, 1996.
- [12] LCA van Breemen, LE Govaert, and HEH Meijer. Scratching polycarbonate: A quantitative model. *Wear*, 274-275(0):238–247, 2012.
- [13] HEH Meijer and LE Govaert. Multi-scale analysis of mechanical properties of amorphous polymer systems. *Macromol. Chem. Phys.*, 204(2):274–288, 2003.

- [14] KI Winey and RA Vaia. Polymer nanocomposites. *MRS Bull.*, 32(04):314–322, 2007.
- [15] B Pukánszky. Interfaces and interphases in multicomponent materials: past, present, future. *Eur. Polym. J.*, 41(4):645–662, 2005.
- [16] JD Eshelby. The determination of the elastic field of an ellipsoidal inclusion, and related problems. *Proc. R. Soc. A*, 241(1226):376–396, 1957.
- [17] R Hill. A self-consistent mechanics of composite materials. *J. Mech. Phys. Solids*, 13(4):213–222, 1965.
- [18] T Mori and K Tanaka. Average stress in matrix and average elastic energy of materials with misfitting inclusions. *Acta Metall.*, 21(5):571–574, 1973.
- [19] RM Christensen and KH Lo. Solutions for effective shear properties in three phase sphere and cylinder models. *J. Mech. Phys. Solids*, 27(4):315–330, 1979.
- [20] JW Ju and TM Chen. Effective elastic moduli of two-phase composites containing randomly dispersed spherical inhomogeneities. *Acta Mech.*, 103(1–4):123–144, 1994.
- [21] JW Ju and TM Chen. Micromechanics and effective moduli of elastic composites containing randomly dispersed ellipsoidal inhomogeneities. *Acta Mech.*, 103(1–4):103–121, 1994.
- [22] S Torquato. Effective stiffness tensor of composite media : II. applications to isotropic dispersions. *J. Mech. Phys. Solids*, 46(8):1411–1440, 1998.
- [23] AA Gusev. Representative volume element size for elastic composites: A numerical study. *J. Mech. Phys. Solids*, 45(9):1449–1459, 1997.
- [24] N Ohno, X Wu, and T Matsuda. Homogenized properties of elastic–viscoplastic composites with periodic internal structures. *Int. J. Mech. Sci.*, 42(8):1519–1536, 2000.
- [25] HGH van Melick, LE Govaert, and HEH Meijer. Prediction of brittle-to-ductile transitions in polystyrene. *Polymer*, 44(2):457–465, 2003.
- [26] S Kari, H Berger, R Rodriguez-Ramos, and U Gabbert. Computational evaluation of effective material properties of composites reinforced by randomly distributed spherical particles. *Compos. Struct.*, 77(2):223–231, 2007.
- [27] E Gunel and C Basaran. Influence of filler content and interphase properties on large deformation micromechanics of particle filled acrylics. *Mech. Mater.*, 57(0):134–146, 2013.
- [28] J Segurado, J LLorca, and C González. On the accuracy of mean-field approaches to simulate the plastic deformation of composites. *Scr. Mater.*, 46(7):525–529, 2002.
- [29] J Segurado, C González, and J LLorca. A numerical investigation of the effect of particle clustering on the mechanical properties of composites. *Acta Mater.*, 51(8):2355–2369, 2003.
- [30] J Segurado and J LLorca. A numerical approximation to the elastic properties of sphere-reinforced composites. *J. Mech. Phys. Solids*, 50(10):2107–2121, 2002.
- [31] J Segurado and J LLorca. Computational micromechanics of composites: The effect of particle spatial distribution. *Mech. Mater.*, 38(8-10):873–883, 2006.

- [32] O Pierard, J Llorca, J Segurado, and I Doghri. Micromechanics of particle-reinforced elastoviscoplastic composites: Finite element simulations versus affine homogenization. *Int. J. Plast.*, 23(6):1041–1060, 2007.
- [33] N Sheng, MC Boyce, DM Parks, GC Rutledge, JI Abes, and RE Cohen. Multiscale micromechanical modeling of polymer/clay nanocomposites and the effective clay particle. *Polymer*, 45(2):487–506, 2004.
- [34] Y Li, AM Waas, and EM Arruda. The effects of the interphase and strain gradients on the elasticity of layer by layer (lbl) polymer/clay nanocomposites. *Int. J. Solids Struct.*, 48(6):1044–1053, 2011.
- [35] G Cricri, E Garofalo, F Naddeo, and L Incarnato. Stiffness constants prediction of nanocomposites using a periodic 3d-fem model. *J. Polym. Sci., Part B: Polym. Phys.*, 50(3):207–220, 2012.
- [36] M Pahlavanpour, P Hubert, and M Lévesque. Numerical and analytical modeling of the stiffness of polymer-clay nanocomposites with aligned particles: One- and two-step methods. *Comput. Mater. Sci.*, 82(0):122–130, 2014.
- [37] MC Boyce, DM Parks, and AS Argon. Large inelastic deformation of glassy polymers. part i: Rate dependent constitutive model. *Mech. Mater.*, 7:15–33, 1988.
- [38] EM Arruda and MC Boyce. Evolution of plastic anisotropy in amorphous polymers during finite straining. *Int. J. Plast.*, 9(6):697–720, 1993.
- [39] CP Buckley and DC Jones. Glass-rubber constitutive model for amorphous polymers near the glass transition. *Polymer*, 36(17):3301–3312, 1995.
- [40] CP Buckley, PJ Dooling, J Harding, and C Ruiz. Deformation of thermosetting resins at impact rates of strain. part 2: constitutive model with rejuvenation. *J. Mech. Phys. Solids*, 52(10):2355–2377, 2004.
- [41] DSA De Focatiis, J Embery, and CP Buckley. Large deformations in oriented polymer glasses: Experimental study and a new glass-melt constitutive model. *J. Polym. Sci., Part B: Polym. Phys.*, 48(13):1449–1463, 2010.
- [42] TA Tervoort, RJM Smit, WAM Brekelmans, and LE Govaert. A constitutive equation for the elastoviscoplastic deformation of glassy polymers. *Mech. Time-Depend. Mater.*, 1(3):269–291, 1997.
- [43] ETJ Klompen, TAP Engels, LE Govaert, and HEH Meijer. Modelling of the post-yield response of glassy polymers: Influence of thermomechanical history. *Macromolecules*, 38(16):6997–7008, 2005.
- [44] LCA van Breemen, ETJ Klompen, LE Govaert, and HEH Meijer. Extending the EGP constitutive model for polymer glasses to multiple relaxation times. *J. Mech. Phys. Solids*, 59(10):2191–2207, 2011.
- [45] DJA Senden, S Krop, JAW van Dommelen, and LE Govaert. Rate- and temperature-dependent strain hardening of polycarbonate. *J. Polym. Sci., Part B: Polym. Phys.*, 50(24):1680–1693, 2012.
- [46] LCA van Breemen, TAP Engels, ETJ Klompen, DJA Senden, and LE Govaert. Rate- and temperature-dependent strain softening in solid polymers. *J. Polym. Sci., Part B: Polym. Phys.*, 50(24):1757–1771, 2012.
- [47] M Ishikawa, I Narisawa, and H Ogawa. Criterion for craze nucleation in polycarbonate. *J. Polym. Sci., Polym. Phys. Ed.*, 15(10):1791–1804, 1977.

- [48] M Ishikawa and I Narisawa. The effect of heat treatment on plane strain fracture of glassy polymers. *J. Mater. Sci.*, 18(9):2826–2834, 1983.
- [49] RP Kambour and EA Farraye. Crazeing beneath notches in ductile glassy polymers: A materials correlation. *Polymer communications Guildford*, 25(12):357–360, 1984.
- [50] RP Nimmer and JT Woods. An investigation of brittle failure in ductile, notch-sensitive thermoplastics. *Polym. Eng. Sci.*, 32(16):1126–1137, 1992.
- [51] TAP Engels, LCA van Breemen, LE Govaert, and HEH Meijer. Criteria to predict the embrittlement of polycarbonate. *Polymer*, 52(8):1811–1819, 2011.
- [52] HA Visser, TC Bor, M Wolters, LL Warnet, and LE Govaert. Influence of physical aging on impact embrittlement of upvc pipes. *Plast., Rubber Compos.*, 40(5):201–212, 2011.
- [53] N Chawla and KK Chawla. Microstructure-based modeling of the deformation behavior of particle reinforced metal matrix composites. *J. Mater. Sci.*, 41(3):913–925, 2006.
- [54] MATLAB. *version 7.12.0 (R2011a)*. The MathWorks Inc., Natick, Massachusetts, 2011.
- [55] Gambit. *version 2.4.6*. Ansys Inc., Cecil Township, Pennsylvania, 2007.
- [56] C Bauwens-Crowet, JC Bauwens, and G Homès. The temperature dependence of yield of polycarbonate in uniaxial compression and tensile tests. *J. Mater. Sci.*, 7(2):176–183, 1972.
- [57] ETJ Klompen and LE Govaert. Nonlinear viscoelastic behaviour of thermorheologically complex materials: a modeling approach. *Mech. Time-Depend. Mater.*, 3(1):49–69, 1999.
- [58] AD Mulliken and MC Boyce. Mechanics of the rate-dependent elastic–plastic deformation of glassy polymers from low to high strain rates. *Int. J. Solids Struct.*, 43(5):1331–1356, 2006.
- [59] TAP Engels, LE Govaert, and HEH Meijer. 2.29 - mechanical characterization of glassy polymers: Quantitative prediction of their short- and long-term responses. In K Matyjaszewski and M Möller, editors, *Polymer Science: A Comprehensive Reference*, pages 723–747. Elsevier, Amsterdam, 2012. ISBN 978-0-08-087862-1. doi: 10.1016/B978-0-444-53349-4.00054-6.
- [60] RJ Gardner and JR Martin. Humid aging of plastics: Effect of molecular weight on mechanical properties and fracture morphology of polycarbonate. *J. Appl. Polym. Sci.*, 24(5):1269–1280, 1979.
- [61] PA O’Connell, J Wang, TA Ishola, and GB McKenna. Exceptional property changes in ultrathin films of polycarbonate: Glass temperature, rubbery stiffening, and flow. *Macromolecules*, 45(5): 2453–2459, 2012.
- [62] CM Evans, H Deng, WF Jager, and JM Torkelson. Fragility is a key parameter in determining the magnitude of tg-confinement effects in polymer films. *Macromolecules*, 46(15):6091–6103, 2013.
- [63] N Shamim, YP Koh, SL Simon, and GB McKenna. Glass transition temperature of thin polycarbonate films measured by flash differential scanning calorimetry. *J. Polym. Sci., Part B: Polym. Phys.*, 52(22):1462–1468, 2014.
- [64] TAP Engels, BAG Schrauwen, LE Govaert, and HEH Meijer. Improvement of the long-term performance of impact-modified polycarbonate by selected heat treatments. *Macromol. Mater. Eng.*, 294(2):114–121, 2009.

- [65] KM Blackwood, RA Pethrick, FI Simpson, RE Day, and CL Watson. Titanium dioxide induced failure in polycarbonate. *J. Mater. Sci.*, 30(17):4435–4445, 1995.
- [66] D Cangialosi, M Wübbenhorst, J Groenewold, E Mendes, H Schut, A van Veen, and SJ Picken. Physical aging of polycarbonate far below the glass transition temperature: Evidence for the diffusion mechanism. *Phys. Rev. B*, 70:224213, Dec 2004.
- [67] D Cangialosi, M Wübbenhorst, J Groenewold, E Mendes, and SJ Picken. Diffusion mechanism for physical aging of polycarbonate far below the glass transition temperature studied by means of dielectric spectroscopy. *J. Non-Cryst. Solids*, 351(33-36):2605–2610, 2005. Proceedings of 3rd International Conference on Broadband Dielectric Spectroscopy and its Applications.
- [68] RD Priestley. Physical aging of confined glasses. *Soft Matter*, 5:919–926, 2009.
- [69] KP Unnikrishnan and ET Thachil. Toughening of epoxy resins. *Des. Monomers Polym.*, 9(2):129–152, 2006.
- [70] GM Odegard and A Bandyopadhyay. Physical aging of epoxy polymers and their composites. *J. Polym. Sci., Part B: Polym. Phys.*, 49(24):1695–1716, 2011.
- [71] A Patnaik, P Kumar, S Biswas, and M Kumar. Investigations on micro-mechanical and thermal characteristics of glass fiber reinforced epoxy based binary composite structure using finite element method. *Comput. Mater. Sci.*, 62:142–151, 2012.
- [72] R Bagheri and R Pearson. Role of particle cavitation in rubber-toughened epoxies: Ii. inter-particle distance. *Polymer*, 41(1):269–276, 2000.
- [73] S Wu, Q Guo, S Peng, N Hameed, M Kraska, B Stühn, and YW Mai. Toughening epoxy thermosets with block ionomer complexes: A nanostructure–mechanical property correlation. *Macromolecules*, 45(9):3829–3840, 2012.
- [74] J Chen, AJ Kinloch, S Sprenger, and AC Taylor. The mechanical properties and toughening mechanisms of an epoxy polymer modified with polysiloxane-based core-shell particles. *Polymer*, 54(16):4276–4289, 2013.
- [75] AC Moloney, HH Kausch, and HR Stieger. The fracture of particulate-filled epoxide resins. *J. Mater. Sci.*, 19(4):1125–1130, 1984.
- [76] P Dittanet and RA Pearson. Effect of silica nanoparticle size on toughening mechanisms of filled epoxy. *Polymer*, 53(9):1890 – 1905, 2012.
- [77] D Maxwell, RJ Young, and AJ Kinloch. Hybrid particulate-filled epoxy-polymers. *J. Mater. Sci. Lett.*, 3(1):9–12, 1984.
- [78] AJ Kinloch, DL Maxwell, and RJ Young. The fracture of hybrid-particulate composites. *J. Mater. Sci.*, 20(11):4169–4184, 1985.
- [79] YL Liang and RA Pearson. The toughening mechanism in hybrid epoxy-silica-rubber nanocomposites (hesrns). *Polymer*, 51(21):4880–4890, 2010.
- [80] LE Govaert, HJ Schellens, HJM Thomassen, RJM Smit, L Terzoli, and T Peijs. A micromechanical approach to time-dependent failure in off-axis loaded polymer composites. *Composites Part A*, 32(12):1697–1711, 2001.

- [81] L Yang, Y Yan, J Ma, and B Liu. Effects of inter-fiber spacing and thermal residual stress on transverse failure of fiber-reinforced polymer-matrix composites. *Comput. Mater. Sci.*, 68(0):255–262, 2013.
- [82] J LLorca and J Segurado. Three-dimensional multiparticle cell simulations of deformation and damage in sphere-reinforced composites. *Mater. Sci. Eng. A*, 365(1-2):267–74, 2004.
- [83] C G'Sell and GB McKenna. Influence of physical ageing on the yield response of model dgeba/poly(propylene oxide) epoxy glasses. *Polymer*, 33(10):2103–2113, 1992.
- [84] J Ma, MS Mo, XS Du, P Rosso, K Friedrich, and HC Kuan. Effect of inorganic nanoparticles on mechanical property, fracture toughness and toughening mechanism of two epoxy systems. *Polymer*, 49(16):3510–3523, 2008.
- [85] LM McGrath, RS Parnas, SH King, JL Schroeder, DA Fischer, and JL Lenhart. Investigation of the thermal, mechanical, and fracture properties of alumina-epoxy composites. *Polymer*, 49(4):999–1014, 2008.
- [86] TH Wu, A Foyet, A Kodentsov, LGJ van der Ven, RATM van Benthem, and G de With. Wet adhesion of epoxy-amine coatings on 2024-t3 aluminum alloy. *Mater. Chem. Phys.*, 145(3):342–349, 2014.
- [87] JN Sultan and FJ McGarry. Effect of rubber particle size on deformation mechanisms in glassy epoxy. *Polym. Eng. Sci.*, 13(1):29–34, 1973.
- [88] RS Kody and AJ Lesser. Deformation and yield of epoxy networks in constrained states of stress. *J. Mater. Sci.*, 32(21):5637–5643, 1997.
- [89] AJ Lesser and RS Kody. A generalized model for the yield behavior of epoxy networks in multiaxial stress states. *J. Polym. Sci., Part B: Polym. Phys.*, 35(10):1611–1619, 1997.
- [90] S Pandini and A Pegoretti. Time, temperature, and strain effects on viscoelastic poisson's ratio of epoxy resins. *Polym. Eng. Sci.*, 48(7):1434–1441, 2008.
- [91] JL Jordan, JR Foley, and CR Siviour. Mechanical properties of epon 826/dea epoxy. *Mech. Time-Depend. Mater.*, 12(3):249–272, 2008.
- [92] BJ Briscoe, PD Evans, SK Biswas, and SK Sinha. The hardnesses of poly(methylmethacrylate). *Tribol. Int.*, 29(2):93–104, 1996.
- [93] BJ Briscoe and SK Sinha. Wear of polymers. *Proc. Inst. Mech. Eng. [J]*, 216(6):401–413, 2002.
- [94] W Brostow, HE Hagg Lobland, and M Narkis. Sliding wear, viscoelasticity, and brittleness of polymers. *J. Mater. Res.*, 21(9):2422–2428, 2006.
- [95] BJ Briscoe and SK Sinha. Scratch resistance and localised damage characteristics of polymer surfaces – a review. *Materialwiss. Werkst.*, 34(10-11):989–1002, 2003.
- [96] YJ Mergler, RJ van Kampen, WJ Nauta, RP Schaake, B Raas, JGH van Griensven, and CJM Meesters. Influence of yield strength and toughness on friction and wear of polycarbonate. *Wear*, 258(5-6): 915–923, 2005.
- [97] V Jardret, H Zahouani, JL Loubet, and TG Mathia. Understanding and quantification of elastic and plastic deformation during a scratch test. *Wear*, 218(1):8–14, 1998.

- [98] C Gauthier and R Schirrer. Time and temperature dependence of the scratch properties of poly(methylmethacrylate) surfaces. *J. Mater. Sci.*, 35(9):2121–2130, 2000.
- [99] I Demirci, C Gauthier, and R Schirrer. Mechanical analysis of the damage of a thin polymeric coating during scratching: role of the ratio of the coating thickness to the roughness of a scratching tip. *Thin Solid Films*, 479(1-2):207–215, 2005.
- [100] F Wredenber and PL Larsson. Scratch testing of metals and polymers: Experiments and numerics. *Wear*, 266(1-2):76–83, 2009.
- [101] J Lee, G Xu, and H Liang. Experimental and numerical analysis of friction and wear behavior of polycarbonate. *Wear*, 251(1-12):1541–1556, 2001. 13th International Conference on Wear of Materials.
- [102] JL Bucaille, C Gauthier, E Felder, and R Schirrer. The influence of strain hardening of polymers on the piling-up phenomenon in scratch tests: Experiments and numerical modelling. *Wear*, 260(7-8):803–814, 2006.
- [103] H Jiang, GT Lim, JN Reddy, JD Whitcomb, and HJ Sue. Finite element method parametric study on scratch behavior of polymers. *J. Polym. Sci., Part B: Polym. Phys.*, 45(12):1435–1447, 2007.
- [104] N Aleksy, G Kermouche, A Vautrin, and JM Bergheau. Numerical study of scratch velocity effect on recovery of viscoelastic–viscoplastic solids. *Int. J. Mech. Sci.*, 52(3):455–463, 2010.
- [105] H Pelletier, C Gauthier, and R Schirrer. Influence of the friction coefficient on the contact geometry during scratch onto amorphous polymers. *Wear*, 268(9–10):1157–1169, 2010.
- [106] Z Wang, P Gu, H Zhang, Z Zhang, and X Wu. Finite element modeling of the indentation and scratch response of epoxy/silica nanocomposites. *Mech. Adv. Mater. Struct.*, 21(10):802–809, 2014.
- [107] MM Hossain, R Minkwitz, P Charoensirisomboon, and HJ Sue. Quantitative modeling of scratch-induced deformation in amorphous polymers. *Polymer*, 55(23):6152–6166, 2014.
- [108] B Feng and Z Chen. Tribology behavior during indentation and scratch of thin films on substrates: Effects of plastic friction. *AIP Advances*, 5(5):057152, 2015.
- [109] K Friedrich, R Reinicke, and Z Zhang. Wear of polymer composites. *Proc. Inst. Mech. Eng. [J]*, 216(6):415–426, 2002.
- [110] RJM Smit, WAM Brekelmans, and HEH Meijer. Predictive modelling of the properties and toughness of polymeric materials. part iii: Simultaneous prediction of micro- and macro-structural deformation of rubber-modified polymers. *J. Mater. Sci.*, 35:2881–2893, 2000.
- [111] N Chen, N Maeda, M Tirrell, , and J Israelachvili. Adhesion and friction of polymer surfaces: The effect of chain ends. *Macromolecules*, 38(8):3491–3503, 2005.
- [112] DB Knorr, TO Gray, and RM Overney. Cooperative and submolecular dissipation mechanisms of sliding friction in complex organic systems. *J. Chem. Phys.*, 129(7):074504, 2008.
- [113] S Krop, HEH Meijer, and LCA van Breemen. Finite element modeling and experimental validation of single-asperity sliding friction of diamond against reinforced and non-filled polycarbonate. *Wear*, 356-357:77–85, 2016.

-
- [114] S Krop, HEH Meijer, and LCA van Breemen. Sliding friction on particle filled epoxy: Developing a quantitative model for complex coatings. *Wear*, 2016. submitted for publication.
- [115] S Krop, HEH Meijer, and LCA van Breemen. Global and local large-deformation response of sub-micron, soft- and hard-particle filled polycarbonate. *J. Mech. Phys. Solids*, 87:51–64, 2016.
- [116] S Krop, HEH Meijer, and LCA van Breemen. Multi-mode modeling of global, and precise local deformation and failure in particle filled epoxy systems. *Composites Part A*, 2016. submitted for publication.
- [117] LCA van Breemen. *Contact mechanics in glassy polymers*. PhD thesis, Eindhoven University of Technology, Eindhoven, 2009.
- [118] HEH Meijer and LE Govaert. Mechanical performance of polymer systems: The relation between structure and properties. *Prog. Polym. Sci.*, 30(8):915–938, 2005.
- [119] DJA Senden, JAW van Dommelen, and LE Govaert. Strain hardening and its relation to bauschinger effects in oriented polymers. *J. Polym. Sci., Part B: Polym. Phys.*, 48(13):1483–1494, 2010.

Samenvatting

In de verfproducerende industrie worden jaarlijks miljarden euro's omgezet terwijl de ontwikkeling van nieuwe coatings nog altijd veelal slechts gebaseerd is op ervaring en een "trial-and-error" benadering. De onderliggende basisfenomenen van wrijving en slijtage zijn nog steeds niet volledig begrepen. Belangrijke eigenschappen van de (poly-mere) verf, zoals krasvastheid, worden verbeterd via wijzigingen in de chemie of door toevoeging van vulstoffen. Vulstoffen kunnen, ten opzichte van de basiscoating, zowel hard zijn of zacht; de deeltjesdiameter is normaal gesproken in de orde 100–1000 nanometer. Vulstoffen worden onder andere toegepast om coatings harder te maken, om de slagvastheid te verbeteren, of als kleurstof. Ze beïnvloeden tevens het mechanische gedrag van de coating en, als gevolg daarvan, ook het wrijvings- en slijtagegedrag.

Eerder onderzoek heeft aangetoond dat het krasgedrag van een onge vuld glasachtig modelpolymeer (polycarbonaat) via simulaties kwantitatief kan worden voorspeld, mits het juiste materiaalmodel wordt gebruikt. Het experiment waarin met een enkelvoudige indenter in het oppervlak van de coating wordt gekrast werd succesvol gemodelleerd met een eenvoudig snelheidsafhankelijk frictiemodel gecombineerd met het zogenaamde "Eindhoven Glassy Polymer" (EGP) constitutieve materiaalmodel. De simulaties voorspelden zowel de afhankelijkheid van krasdiepte en wrijvingskracht van de krassnelheid, als de invloed van verschillende geometrieën van de diamanten indenter, kwantitatief.

Dit proefschrift borduurt voort op dit pionierswerk door het uit te breiden naar met deeltjes gevulde polymere systemen. In eerste instantie wordt voor de matrix (het basismateriaal) opnieuw gebruik gemaakt van het volledig gekarakteriseerde modelpolymeer polycarbonaat, ditmaal gevuld met harde (TiO_2) of zachte (MBS-rubber) deeltjes. Het intrinsieke spannings-rek gedrag is gemeten met behulp van gecontroleerde compressieproeven waarin de totale respons van het gevulde systeem wordt bepaald. Om inzicht te verkrijgen in de lokale spanningen en rekken, worden simulaties gedaan. De complexe microstructuren zijn gemodelleerd met vereenvoudigde driedimensiona-

le Representatieve Volume Elementen (3D-RVE's). Hiermee worden de compressie-experimenten gesimuleerd in een eindige elementen methode omgeving. Het EGP model voorspelt de experimenten uitstekend, en de simulaties geven tevens detailinformatie over kritische lokale spanningen en rekken tussen de deeltjes die uiteindelijk leiden tot macroscopische schade en falen van het coating-materiaal.

Met de gehomogeniseerde materiaalparameters die uit de simulaties volgen, en die het macroscopisch gedrag van de gevulde systemen beschrijven, worden krassimulaties uitgevoerd en vergeleken met de experimenten. Wederom blijkt dat het combineren van een kwantitatief correct materiaalmodel met een simpel snelheidsonafhankelijk (Coulombs) frictiemodel leidt tot een succesvolle beschrijving van de experimenten. Deze simulaties geven ook waarden van de (gehomogeniseerde) kritische rekken die leiden tot zichtbare schade. Door deze vervolgens op te leggen op de randen van de RVE's worden de kritische spanningen en rekken, op een lager schaalniveau, die tussen de deeltjes van de vulstof, bepaald. Deze informatie wordt later gebruikt om de microstructuur aan te passen en te optimaliseren.

Voor verfapplicaties is polycarbonaat niet relevant. Daarom wordt de methode vervolgens toegepast op systemen met een thermoharder als matrix, een commercieel verkrijgbare epoxy. Eerst wordt dit nieuwe matrixmateriaal gekarakteriseerd om de parameters in het EGP model te bepalen, vervolgens zijn systemen geprepareerd met zachte (polysiloxaan rubber) of met harde (TiO_2) vulstofdeeltjes, en getest in compressie- en krasexperimenten. Er wordt vervolgens aangetoond dat de ontwikkelde hybride experimentele/numerieke methode ook kan worden toegepast op systemen met een thermoharder als basis.

Het proefschrift eindigt met een aanzet tot het ontwerpen van geoptimaliseerde kras- en slijtagebestendige coatings. Hierbij wordt gebruik gemaakt van inzichten verkregen uit experimenten en simulaties van zowel gevuld polycarbonaat als epoxy. De analyse leidt tot aanbevelingen voor nieuwe coatings. Via een criterium voor de aanzet tot falen en slijtage in ongepulde coatings (*het overschrijden van een kritische, netwerkdichtheidafhankelijke, drie-assige spanningstoestand*) wordt een nieuw criterium voor gevulde coatings afgeleid (*het overschrijden van de, als gevolg van deze spanningstoestand, opgeslagen elastische energie per eenheid oppervlak tussen matrix en vulstof*). Complexe microstructuren worden gemodelleerd in tweedimensionale RVE's en vervolgens virtueel getest. Verschillende scenario's worden verkend en geven directe aanwijzingen voor geoptimaliseerde hybride microstructuren (zowel hiërarchisch in deeltjesgrootte, als met "core-shell" structuren) voordat het tijdrovende proces van synthese van nieuwe materialen, en van nieuwe vulstoffen en hun composieten, hoeft te worden doorlopen.

Dankwoord

Met dit proefschrift sluit ik een hele mooie, maar op het laatst ook (uiteraard) hectische periode af. Ik wil beginnen met Han en Lambèrt te bedanken voor de kans om aan dit “supervette krasproject” te mogen werken. Het was een ervaring die ik niet had willen missen. Ik waardeer de manier waarop jullie me enerzijds de vrijheid hebben gegeven om zelf te gaan ontdekken, maar ook aan de rem trokken waar dat nodig was. Er ligt nu een boekje waar ik oprecht trots op ben, en daarvoor ben ik jullie dankbaar.

Furthermore, I would like to thank Akzo Nobel N.V. for financially supporting this project. My gratitudes go to the people at Felling, especially Andrew Burgess and Paul Dooling, for the interesting discussions, both inside and outside the scope of my work. I enjoyed the collaboration and the opportunity that you gave me.

Dit boekje markeert niet alleen het einde van vier jaar onderzoek, maar eigenlijk van een véél langere carrière aan de TU/e. Daarom wil ik ook graag Leon noemen, die mij dankzij een zeer geslaagde bachelor eindproject introduceerde binnen deze fantastische groep, overhaalde om toch aan de Master te beginnen via een groepsproject (hij had al “twee serieuze jongens”), en dankzij zijn aanstekelijke “*blij met kunststof*” is de rest geschiedenis. Ik heb echt een heerlijke tijd gehad en wil dan ook alle (ex-)collega’s binnen de polymerengroep, maar ook daarbuiten, daarvoor bedanken. Dat geldt ook voor de ondersteunende staf (onterecht, want eigenlijk dragend) op het secretariaat (Marleen en Ans), de werkplaats (Sjef, Rob, Pieter en Lucien), het systeembeheer a.k.a. Leo en, tot slot, Marc van Maris, de koning van het multi-scale lab.

Ik heb altijd en enorme waardering gehad voor de integratie van onderwijs en onderzoek binnen deze groep. Eerst als student en later tijdens mijn promotie in de begeleidende rol. Ik wil dan ook alle studenten bedanken voor hun, al dan niet directe, bijdrage binnen mijn project: Sander, Jelle, Jeroen, Daniël, Astrid, Frank, Mark, Berton, Guy, Mike en Stan.

Ook ben ik dank verschuldigd aan alle familie en vrienden, die mij misschien voor

gek versleten toen ik nog eens (vrijwillig) tekende voor een verlenging van mijn TU/e-bestaan, maar me wel hebben ondersteund en in me zijn blijven geloven. Speciale dank en waardering gaan naar John en Connie, omdat jullie mij geleerd hebben om verder te kijken dan mijn neus lang is en vooral eigenzinnig te zijn. En dan, tot slot, de belangrijkste van allemaal. Mijn woorden zijn op, maar jij bent echt de belangrijkste. Lieve Barbara, ik ben er weer, voor jou.

Sam

Eindhoven, maart 2016

Curriculum Vitae

Sam Krop was born in Paramaribo, Suriname, on the first of February 1983. At the age of 12, he moved to the Netherlands, where he graduated in 2001 from his pre-academic secondary education at the H.N. Werkman College in Groningen. He then enrolled as a student in the department of Mechanical Engineering at the Eindhoven University of Technology, where he received his Bachelor's degree in 2009. His Bachelor Final Project, entitled "Enhanced Ageing kinetics under dynamic load?" under the supervision of dr.ir. L.E. (Leon) Govaert, inspired him to join the Polymer Technology group chaired by prof.dr.ir. H.E.H. (Han) Meijer. There he received his Master's degree in August 2011, under the supervision of dr.ir. L.E. (Leon) Govaert and dr.ir. J.A.W. (Hans) van Dommelen, with the thesis entitled "Constitutive modeling of rate and temperature dependent strain hardening in polycarbonate".

In October 2011, Sam accepted the opportunity to pursue a PhD-degree under the guidance of dr.ir. L.C.A. (Lambert) van Breemen and prof.dr.ir. H.E.H. (Han) Meijer. The results of his project, financially supported by AkzoNobel N.V. and concerning contact phenomena of particle-filled polymers, are presented in this thesis.

During his PhD the author successfully completed the postgraduate course Register Polymer Science of the National Dutch Research School PTN (Polymeer Technologie Nederland) and was awarded the title of Registered Polymer Scientist in April 2014. The course consists of the following modules: (A) Polymer Chemistry, (B) Polymer Physics, (C) Polymer Properties, and (D) Rheology & Polymer Processing.

List of Publications

This thesis has resulted in the following publications:

- S. Krop, H.E.H. Meijer, and L.C.A. van Breemen. "Global and local large-deformation response of sub-micron, soft- and hard-particle filled polycarbonate," *Journal of the Mechanics and Physics of Solids* **87**, 51–64 (2016).
- S. Krop, H.E.H. Meijer, and L.C.A. van Breemen. "Multi-mode modeling of global and local deformation, and failure, in particle filled epoxy systems," *Composites Part A: Applied Science and Manufacturing*, submitted for publication (2016).
- S. Krop, H.E.H. Meijer, and L.C.A. van Breemen. "Finite element modeling and experimental validation of single-asperity sliding friction of diamond against reinforced and non-filled polycarbonate," *Wear*, in press (2016).
- S. Krop, H.E.H. Meijer, and L.C.A. van Breemen. "Sliding friction on particle filled epoxy: Developing a quantitative model for complex coatings," *Wear*, submitted for publication (2016).

Additionally, the author has contributed to:

- D.J.A. Senden, S. Krop, J.A.W. van Dommelen, and L.E. Govaert. "Rate- and temperature-dependent strain hardening of polycarbonate." *J. Polym. Sci., Part B: Polym. Phys.*, **50**, 1680–1693 (2012).